Some Aspects of the Crystal Chemistry of Perovskites under High Pressures

Di Wang

Dissertation submitted to the faculty of the Virginia Polytechnic Institute and State University in partial fulfillment of the requirements for the degree of

Doctor of Philosophy
In
Geosciences

Nancy L. Ross, Chair
Ross J. Angel
Gerald V. Gibbs
Scott D. King
Renata M. Wentzcovitch

April 26, 2012
Blacksburg, VA

Keywords: perovskite, high pressure, symmetry-adapted mode phase transition, elasticity, phonon, $LaAlO_3$, $YAlO_3$, DFT

Some Aspects of the Crystal Chemistry of Perovskites under High Pressures

Di Wang

Abstract

This dissertation makes contributions to the methodology of quantitative description of the tilting systems of perovskite structures and theoretical analysis of high-pressure phase transitions of representative perovskites.

Chapter 1 and 2 introduce the perovskite structures, tilting classification and descriptions. The structures in each of the 15 tilt systems have been decomposed in to the amplitudes of symmetry-adapted modes in order to provide a clear and unambiguous definition of the tilt angles. A general expression in terms of tilt angles for the ratio of the volumes of the two polyhedra within the perovskite structure is derived.

Chapter 3 uses the first-principles plane-wave pseudopotential calculations to investigate the high-pressure $R\bar{3}c$ to $Pm\bar{3}m$ phase transition and elasticity of $LaAlO_3$ perovskite. This second order transition is determined to occur at ~14 GPa by the pressure variation of the squared frequency of the soft *R*-point mode in the $Pm\bar{3}m$ structure. Elastic moduli are inverted from the calculated stress-strain data by the singular value decomposition method. The Landau parameters for this phase transition are calibrated from the calculation results.

Chapter 4 uses the same method to investigate the high-pressure phase transitions and elasticity of $YAlO_3$ perovskite. The *Pnma*, *Imma*, *I*4/*mcm*, $R\bar{3}c$, $Pm\bar{3}m$ perovskite structures and the NH_4CdCl_3-, Gd_2S_3-, U_2S_3-, $CaIrO_3$-type structures are considered. A continuous *Pnma* to *Imma* transition occurs at ~89 GPa, determined from the soft *Z*-point mode of the *Imma* structure. Then, a discontinuous *Imma* to *I*4/*mcm* transition occurs at ~100 GPa, suggested by the relative enthalpies and phonon dispersions. The elasticities of the *Pnma*, *Imma* and *I*4/*mcm* structures show mechanical stabilities compatible with the phase transitions. The NH_4CdCl_3- and $CaIrO_3$-type structures are dynamically stable although not energetically favorable. The relative *A*/*B* site polyhedral volume ratios are found to qualitatively reproduce the relative enthalpies of the perovskite structures.

Author Acknowledgements

The author would like to thank Dr. Nancy L. Ross and Dr. Ross J. Angel for the selection of the research topics and guidance in crystallography, mineralogy and physics. Thanks also go to Dr. Gerald V. Gibbs and Dr. Scott D. King for the microscopic and macroscopic overviews of the projects. Dr. Renata M. Wentzcovitch (U. Minnesota) is thanked for introducing me to the first-principles calculation.

The author would also like to thank Dr.Yonggang Yu for sharing his computational experience. Dr. Jing Zhao is thanked for his modeling of perovskite, Dr. Koichiro Umemoto (U. Minnesota) is thanked for his help in generating pseudopotentials, and Dr. Branton J. Campbell, Dr. Harold T. Stokes (Brigham Young U.) and Dr. Christopher J. Howard (U. Newcastle, Australia) are thanked for discussions on symmetry-adapted modes.

All the calculations in this dissertation were performed on the supercomputers from the Advanced Research Computing at Virginia Tech, and the Minnesota Supercomputing Institute at University of Minnesota, to which the author would like to acknowledge.

The author acknowledges with gratitude the financial support from the National Science Foundation grants EAR-0738692 to Dr. Nancy L. Ross and Dr. Ross J. Angel, EAR-0635990, ATM-0428774 to Dr. Renata M. Wentzcovitch, and the Virginia Tech Department of Geosciences Chinese Scholar Fellowship to Di Wang.

Table of Contents

List of Figures

List of Tables

Chapter 1: Introduction

1.1 Perovskite

Perovskite is believed to be the dominant mineral of the lower mantle (Ringwood, 1975). $(Mg,Fe)SiO_3$, $(Mg,Fe,Al)(Al,Si)O_3$ and $CaSiO_3$ perovskites are formed between 580 and 750 km depth (Helffrich and Wood, 2001). Thus, the thermodynamic properties and phase transitions of perovskites can help us investigate the composition and dynamics of the lower mantle and even the core-mantle boundary. And to extract information regarding the composition of mantle from seismological observations, elastic properties of candidate minerals at high pressures are required. Properties of perovskites are of interest also because many perovskites with other element compositions have applications in industry. For example, $YAlO_3$ perovskite can be used as a solid-state laser host (Weber *et al.*, 1969), $LaAlO_3$ perovskite is a substrate material for high-temperature superconductor films (Lee *et al.*, 1990; Konaka *et al.*, 1991) and $BaZrO_3$ is a high-temperature capacitor dielectric (Koenig and Jaffe, 1964).

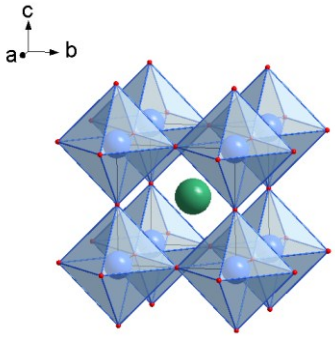

Cubic $Pm\bar{3}m$ $a^0a^0a^0$

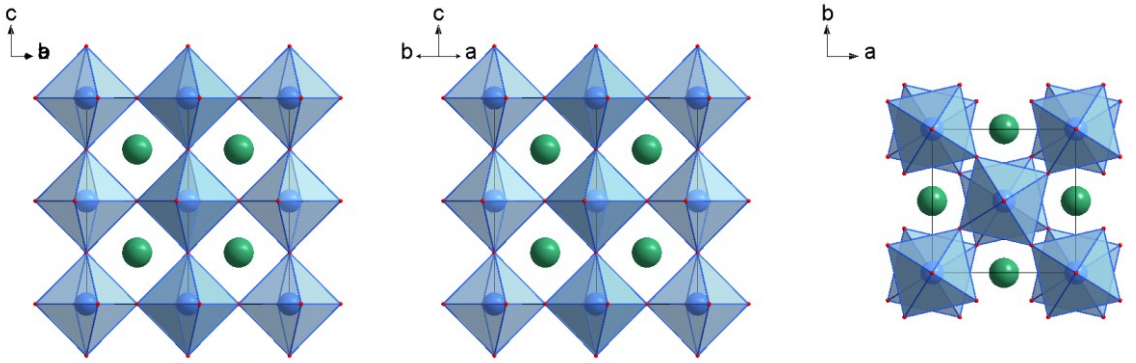

*I*4/*mcm* $a^0a^0c^-$

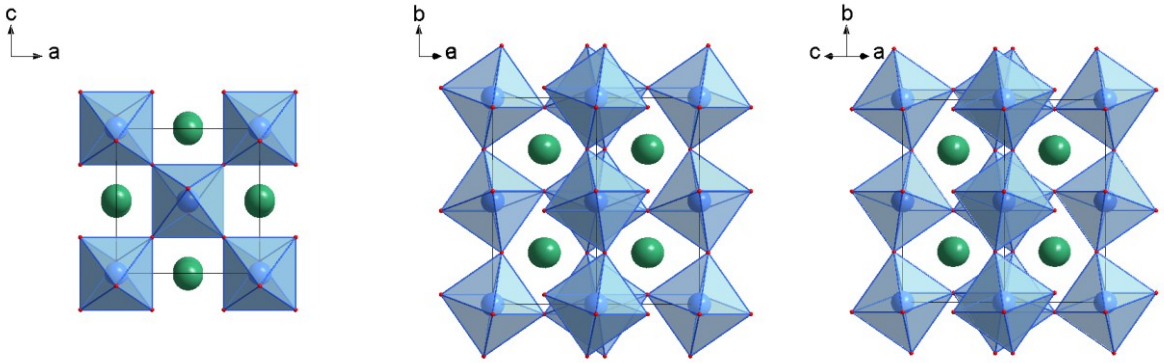

Imma $a^0b^-b^-$

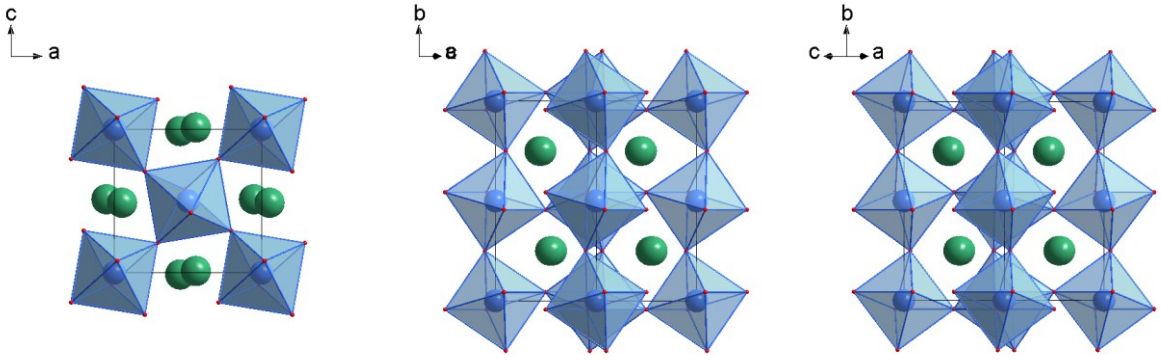

Pnma $a^+b^-b^-$

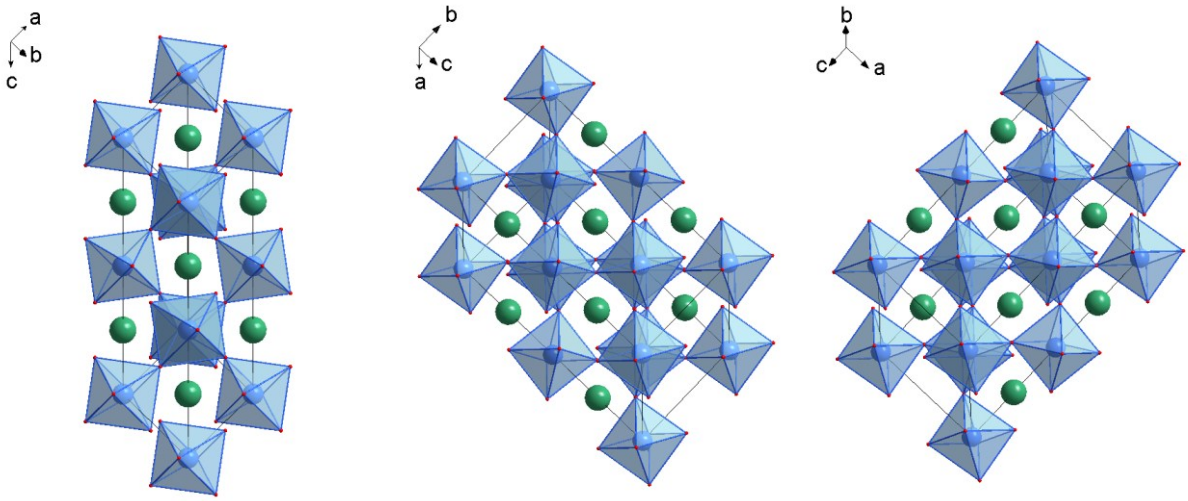

$R\bar{3}c$ $a^-a^-a^-$

Figure 1.1 Five perovskite structures viewed along three pseudo-cubic axes. Each column corresponds one letter symbol.

1.2 Tilting systems of perovskite

The structure of perovskite ABO_3 can be described as a framework of corner-linked BO_6 octahedra where *B* cations are at the center of the octahedra and *A* cations are at the center of the space between the octahedra. A small portion of perovskites have the ideal cubic structure where BO_6 octahedra are regular and all the *B*–O–*B* bond angles are 180° as plotted in Figure 1.1. Most perovskites are distorted from the cubic structure. Three types of distortions are possible (Megaw, 1973): distortions of the BO_6 octahedra, displacement of *B* cation in the octahedra and the tilting of the BO_6 octahedra. Assuming that the octahedra keep the regular shape and connection with one another through the corners during tilting, 23 different simple tilting systems are identified in terms of the rotations around *a*-, *b*- and *c*-axes which parallel the three cubic lattice vectors and cross the central *B* cation (Glazer, 1972). Here is a brief introduction. If an octahedron rotates around one axis, the rotation of all the other octahedra in the layer perpendicular to that axis is constrained by the connectivity. But the two adjacent octahedra

along that axis can rotate in the same or the opposite sense. Thus notations $a^{\#}b^{\#}c^{\#}$ are used to denote different tilting systems where # can be 0, + and -. 0 means no rotation around the corresponding axis; + means the octahedra along the corresponding axis rotate in the same sense and by the same angle; - means that any two adjacent octahedra along the corresponding axis rotate in the opposite sense and by the same angle. Repeated letters among $a^{\#}b^{\#}c^{\#}$ mean the rotations around the corresponding axes have the same magnitude. Five examples are given in Figure 1.1.

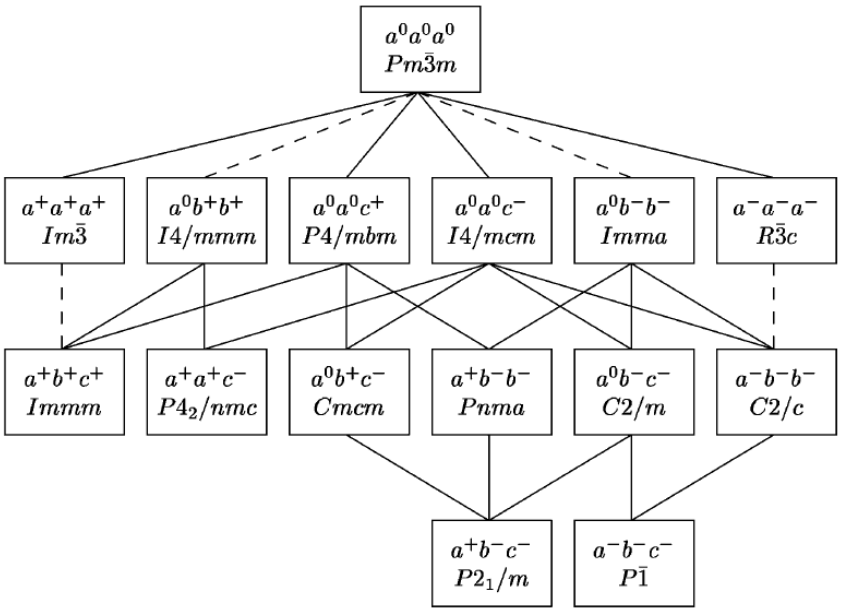

Figure 1.2 A schematic diagram indicating the group-subgroup relationships among the 15 space groups. The solid and dashed lines join a group with its subgroup. A dashed line indicates that the corresponding phase transition is required by Landau theory to be first order. Quoted from Howard and Stokes (2002, 1998).

1.3 Space groups of perovskite

Glazer identified the space group for each tilting system by close examination and found 15 different space groups for a total of 23 tilting systems. However, using a program POTATO, Woodward (1997a) found that six of the tilting systems can not construct a framework of regular

octahedra and that different distortions of the octahedra made to form a framework can lead to different space groups. Although Howard and Stokes (1998) later found a framework of regular octahedra for one of the six tilting systems pointed out by Woodward, the limitation of methodology of examining the rigid tilting systems appears. With the group-theoretical analysis program *ISOTROPY* (Hatch and Stokes, 1985), Howard and Stokes (1998) directly found the 15 space groups as the isotropy subgroups of *Pm*-3*m* using its matrix representation built on the six component tilt systems $a^+b^0b^0$, $b^0a^+b^0$, $b^0b^0a^+$, $a^-b^0b^0$, $b^0a^-b^0$ and $b^0b^0a^-$ as basis functions. Apart from correcting one space group among Glazer's 15, they indentified the group-subgroup relationships among the 15 space groups and the order of the phase transitions between different space groups (Figure 1.2). In the literature survey of Woodward (1997b), 12 of the 15 space groups suggested by Howard and Stokes have been reported experimentally. The only one structure which doesn't belong to Howard and Stokes' 15 space groups seems poorly determined.

1.4 Phase transitions of perovskite

It has long been believed that the large AO_{12} cuboctahedra have greater compressibility and thermal expansivity than the small BO_6 octahedra, so when a perovskite is compressed the size of the AO_{12} cuboctahedra is reduced through tilting of the rigid BO_6 octahedra (Hazen and Finger, 1979). When the AO_{12} cuboctahedra reach a minimum size, a transition to a more distorted or lower-symmetry phase occurs. However, Zhao *et al.* (2004) and Angel *et al.* (2005) found experimentally the bond valence matching in perovskites and consequently proved that the AO_{12} cuboctahedra are more compressible in the $A^{2+}B^{4+}O_3$ (2:4) perovskites, but less compressible in the $A^{3+}B^{3+}O_3$ (3:3) perovskites, than the BO_6 octahedra. It is thereby explained why experiments on 3:3 perovskites show that the BO_6 octahedra are less, rather than more, tilted with increasing pressure (Ross *et al.*, 2004a, b). A general rule controlling the phase transitions in perovskites is hence identified: with increasing pressure 2:4 perovskites change to a more-distorted or lower-symmetry phase while 3:3 perovskites change to a less distorted or higher-symmetry phase (Zhao *et al.*, 2004; Angel *et al.*, 2005). Since Strens (1967) demonstrated that the higher-symmetry phase in such tilt transitions is also the high-temperature phase because of the greater

degeneracy of normal vibration modes, the Clapeyron slopes of tilt transitions of 2:4 perovskites are positive while those of 3:3 perovskites are negative.

The potential group-subgroup phase transitions for ABO_3 perovskites are joined by dashed or solid lines in Figure 1.2, according to whether they are of first or second order required by Landau theory (Landau and Lifshitz, 1980). This theory also requires that other phase transitions without group-subgroup relationship are all of first order. According to the general rule, as pressure is increased 2:4 perovskites tend to go downward or horizontally in the diagram while 3:3 perovskites show the opposite tendency.

So far, most knowledge about the phase transitions of perovskite comes from experiments at relative low pressures and temperatures. First-principles calculations can help expand our understanding of perovskites by showing their structural evolution, phase transitions, thermodynamic and elastic properties at relatively high pressures and temperatures. Crystal chemistry and first-principles calculation can benefit from and improve each other.

1.5 Reference

Angel R J, Zhao J and Ross N L 2005 General rules for predicting phase transitions in perovskites due to octahedral tilting *Phys. Rev. Lett.* **95** 025503

Glazer A 1972 The classification of tilted octahedra in perovskites *Acta Cryst.* **B28** 3384-92

Hatch D M and Stokes H T 1985 Practical algorithm for identifying subgroups of space groups *Phys. Rev. B* **31** 2908-12

Hazen R M and Finger L W 1979 Polyhedral tilting: A common type of pure displacive phase transition and its relationship to analcite at high pressure *Phase Trans.* **1** 1 - 22

Helffrich G R and Wood B J 2001 The Earth's mantle *Nature* **412** 501-7

Howard C J and Stokes H T 1998 Group-Theoretical Analysis of Octahedral Tilting in Perovskites *Acta Cryst.* **B54** 782-9

Howard C J and Stokes H T 2002 Group-Theoretical Analysis of Octahedral Tilting in Perovskites. Erratum *Acta Cryst.* **B58** 565

Koenig J and Jaffe B 1964 Barium Zirconate Modified with Lanthanum, a High-Temperature Capacitor Dielectric *J. Am. Ceram. Soc.* **47** 87-9

Konaka T, Sato M, Asano H and Kubo S 1991 Relative permittivity and dielectric loss tangent of substrate materials for high-Tc superconducting film *J. Supercond.* **4** 283-8

Landau L D and Lifshitz E M 1980 *Statistical Physics, 3rd ed.,* (New York: Pergamon Press)

Lee A E, Platt C E, Burch J F, Simon R W, Goral J P and Al-Jassim M M 1990 Epitaxially grown sputtered $LaAlO_3$ films *Appl. Phys. Lett.* **57** 2019-21

Megaw H D 1973 *Crystal Structures - a Working Approach* (Philadelphia: W. B. Saunders)

Ringwood A E 1975 *Composition and Petrology of the Earth's Mantle* (London, New York, and Sydney: McGraw-Hill)
Ross N L, Zhao J and Angel R J 2004a High-pressure single-crystal X-ray diffraction study of $YAlO_3$ perovskite *J. Solid State Chem.* **177** 1276-84
Ross N L, Zhao J and Angel R J 2004b High-pressure structural behavior of $GdAlO_3$ and $GdFeO_3$ perovskites *J. Solid State Chem.* **177** 3768-75
Strens R G J 1967 Symmetry-entropy-volume relationships in polymorphism *Miner. Mag.* **36** 565-77
Weber M J, Bass M, Andringa K, Monchamp R R and Comperchio E 1969 Czochralski growth and properties of $YAlO_3$ laser crystals *Appl. Phys. Lett.* **15** 342-5
Woodward P 1997a Octahedral Tilting in Perovskites. I. Geometrical Considerations *Acta Cryst.* **B53** 32-43
Woodward P 1997b Octahedral Tilting in Perovskites. II. Structure Stabilizing Forces *Acta Cryst.* **B53** 44-66
Zhao J, Ross N L and Angel R J 2004 New view of the high-pressure behaviour of $GdFeO_3$-type perovskites *Acta Cryst.* **B60** 263-71

Chapter 2: Octahedral tilts, symmetry-adapted displacive modes and polyhedral volume ratios in perovskite structures

2.1 Abstract

The structures of tilted perovskites in each of the 15 tilt systems have been decomposed in to the amplitudes of symmetry-adapted modes in order to provide a clear and unambiguous definition of the tilt angles. A full expression in terms of the mode amplitudes for the ratio of the volumes of the two polyhedra within the perovskite structure for each of the 15 tilt systems is derived, along with more general expressions in terms of either mode amplitudes or tilt angles that can be used to estimate this ratio when the distortions of the octahedra are small.

2.2 Introduction

The ABX_3 perovskite structure is adopted by minerals of geological importance and many materials with industrial utility. For example, $(Mg,Fe)SiO_3$ perovskite is the predominant phase in the Earth's lower mantle (Ringwood, 1962; Reid and Ringwood, 1975; Liu, 1976; Mao *et al.*, 1977), $BaTiO_3$ and $PbTiO_3$ are important ferroelectrics (e.g. Cohen, 1992), and most high-temperature superconductors are derivatives of the perovskite structure (e.g. Uher, 1990) with an example of MgC_xNi_3 being an intermetallic perovskite superconductor (He *et al.*, 2001). Understanding the relationship between structure, structural variation and thermodynamic properties in perovskites is therefore of importance and utility in many fields.

The ABX_3 perovskite structure comprises a three-dimensional framework of corner-linked BX_6 octahedra with A cations occupying the cavities within the framework. In the ideal cubic perovskite structure with space group $Pm\bar{3}m$ the A cations are 12-coordinated, forming AX_{12} coordination cuboctahedra. When the A cations are not big enough for the cavities within the framework, the relatively rigid BX_6 octahedra tilt to reduce the size of the cavities occupied by the A cations (Megaw, 1966). Subsequent analysis (e.g. Glazer, 1972; Howard and Stokes, 1998, 2002) has shown that there are 15 symmetrically-distinct tilt systems in perovskites that can be

parameterized in terms of the tilts of the octahedra around the three mutually perpendicular tetrad axes of the cubic structure. The tilts of consecutive octahedra along each of the three axes can either be of the same sign and magnitude, or of opposite sign but the same magnitude. This leads to the description of the thermodynamics of phase transitions involving changes in the tilting patterns in terms of two three-dimensional order parameters representing the two types of tilts along each of these three axes (e.g. Howard and Stokes, 2004). Successful analysis of the thermodynamics of perovskite phase transitions involving tilting (Carpenter *et al.*, 2005; Carpenter, 2007; Carpenter *et al.*, 2010) has demonstrated that the tilt angles around the pseudo-cubic axes are indeed thermodynamic order parameters.

The ratio of the volume of the AX_{12} coordination cuboctahedron to that of the BX_6 octahedron, V_A/V_B, is equal to 5 in the cubic aristotype structure, and decreases with increasing tilting of the octahedra in the hettotype structures (e.g. Avdeev *et al.*, 2007). The relative compressibilities and thermal expansivities of the two polyhedra therefore control whether a given perovskite structure becomes more or less tilted with changes in pressure or temperature (Andrault and Poirier, 1991; Zhao *et al.*, 2004; Angel *et al.*, 2005). In particular, because perovskite structures uniformly become less tilted (on average) with increasing temperature, the compressional behavior of the polyhedra determines the phase diagram for tilt transitions in perovskites (Angel *et al.*, 2005). When the BX_6 octahedra are less compressible than the AX_{12} sites the tilts increase with pressure within a single phase, and when tilt transitions occur, they do so to structures with greater tilts and lower symmetry, giving the phase transition boundary a positive slope $\mathrm{d}P/\mathrm{d}T$. Conversely, when the BX_6 octahedra are softer than the AX_{12} sites, tilting decreases with increasing pressure, and tilt transitions occur to less tilted structures with higher symmetry through a phase transition boundary with $\mathrm{d}P/\mathrm{d}T < 0$ (Angel *et al.*, 2005). Thus the polyhedral volume ratio of perovskites, V_A/V_B, and its change with pressure and temperature, is also an important thermodynamic parameter which must be linked to the values of tilt angles as the primary order parameters for tilt transitions.

Calculation of the tilt angles and the polyhedral volume ratio from experimentally-determined perovskite structures is therefore of critical importance for understanding and characterizing the thermodynamics of perovskites. However, except for structures in the three simplest tilt systems

and the trivial case of the cubic aristotype, the octahedra are permitted by symmetry to become distorted in such a way that affects the tilt angles and the polyhedral volume ratio. Thomas (1996, 1998) proposed a method to quantitatively describe all perovskite structures by a few length and angle parameters. Three of the angle parameters were defined as the angles between BX_6 octahedral stalks which connect opposite octahedral vertices, and the corresponding closest pseudo-cubic axes. However, these angles do not correspond to the three tilt angles around the pseudo-cubic axes, especially in tilt systems with three tilts, and they include the distortions of the octahedra as well. Tamazyan & van Smaalen (2007) proposed another geometric parameterization of perovskite structures where the orientation of BX_6 octahedra is described by two rotation angles around the z axis and an axis in the xy plane in a direction defined by a third angle. Because the orientation of the octahedra is defined by only two rotation axes and the second one is not necessarily the x or y axis, this description does not aim at the quantification of the tilts around the three pseudo-cubic axes. Furthermore, as illustrated by these two examples, the decomposition of a perovskite structure including tilted and distorted octahedra by geometric analysis does not result in an unambiguous definition of the Glazer (1972) tilts and the problem is more acute in perovskites with lower space group symmetries (Avdeev *et al.*, 2007). As a consequence, Avdeev *et al.* (2007) provided expressions for the polyhedral volume ratios as direct functions of the fractional coordinates of the anions in each of the perovskite space groups. However, except for the four simplest cases mentioned above, unambiguous expressions for both the Glazer tilts and their relationship to the V_A/V_B ratio remain to be determined both explicitly for each space group, and in a general form.

In this paper I make use of the computer programs *ISOTROPY* (Stokes *et al.*, 2007) and *ISODISTORT* (or the earlier *ISODISPLACE*) (Campbell *et al.*, 2006) to analyze perovskite structures in terms of the irreducible representations of the space group of the parent structure (Perez-Mato *et al.*, 2010). Irreducible representations and symmetry-adapted modes provide a clear and unambiguous way to separate the effects of distortion and tilting of octahedra in perovskites because the modes by definition are orthogonal to one another. I decompose the coordinates in the explicit expressions for V_A/V_B in the 15 tilt systems (Avdeev *et al.*, 2007) in to symmetry-adapted mode amplitudes, to express V_A/V_B as a direct function of the amplitudes of the modes that measure the octahedral tilts and distortions. A comparison of these expressions

reveals a general formula that provides a very close approximation to the value of V_A/V_B for all tilt systems both in terms of the mode amplitudes and the values of the Glazer (1972) tilts.

2.3 Symmetry-adapted mode analysis of perovskites

2.3.1 Previous studies

The perovskite structures were first systematically classified by Glazer (1972) according to different tilting patterns of BX_6 octahedra around the *a*, *b* and *c* axes of the cubic aristotype. Glazer restricted consideration to a simple and common case where the octahedra along the rotation axis rotate by the same angle in the same sense or in opposite senses alternately, which are called 'in-phase' and 'out-of-phase' tilts, respectively. By inspecting all combinations of in-phase and out-of-phase tilts around the three pseudo-cubic axes by the same or different angles, Glazer found 23 tilt systems and assigned their space groups accordingly. Each tilt system was denoted by a symbol $a^{\#}b^{\#}c^{\#}$, where # takes 0, + or - if there is no tilt, in-phase or out-of-phase tilt around the relevant axis. While the analysis by Glazer (1972) greatly assisted in the correct structural analysis of many perovskite systems, it left three crucial issues unaddressed. First were the subtle symmetry issues - whether the tilt systems with higher symmetry between the tilts than required by the space group symmetry were really distinct tilt systems, and whether some proposed tilt systems actually involved two tilts around a single axis. Second, except in the case of three simple tilt systems $a^-a^-a^-$, $a^0a^0c^+$ and $a^0a^0c^-$, the calculation of the values of the tilts from atomic coordinates is neither well-defined nor unique. Related to that issue, in the majority of tilt systems in which octahedral distortion is permitted by the space group symmetry, the separation of distortions and tilts can be done in many ways resulting in different values for the tilt angles.

All three of these issues were addressed by Howard & Stokes (1998, 2002) who followed the description of tilting patterns of perovskite by Glazer (1972) and analysed the tilts in the context of the Landau theory of phase transitions assisted by the computer program *ISOTROPY* (Stokes *et al.*, 2007). The octahedral rotations about the *B* cations are represented by irreps whose basis modes are sets of pseudo-vectors at Wyckoff *a* sites where *B* cations are located. Because BX_6 octahedra may tilt in opposite senses alternately along the three pseudo-cubic axes, the unit cell

dimensions of tilted perovskites can be at most doubled compared to that of the cubic aristotype. Thus, only irreps at special *k*-points Γ (0, 0, 0), *X* (0, 0, $\frac{1}{2}$), *M* ($\frac{1}{2}$, $\frac{1}{2}$, 0) and *R* ($\frac{1}{2}$, $\frac{1}{2}$, $\frac{1}{2}$) in the reciprocal space of the cubic aristotype need be considered. Of the possible irreps, Howard & Stokes (1998, 2002) showed that the basis modes of two three-dimensional irreps M_3^+ and R_4^+ (notation of Miller and Love, 1967) represent the two types of tilt patterns of the octahedra. The in-phase tilt patterns $b^0b^0a^+$, $a^+b^0b^0$, $b^0a^+b^0$ correspond to the three basis modes of irrep M_3^+, and different combinations of these basis modes generate four tilt systems with only in-phase tilts. Similarly, the three basis modes of irrep R_4^+ correspond to the out-of-phase tilt patterns $b^0b^0a^-$, $a^-b^0b^0$, $b^0a^-b^0$, and in various combinations generate the six tilt systems with only out-of-phase tilts. Coupling of M_3^+ and R_4^+ results in 14 potential tilt systems, four of which belong to the simple case Glazer (1972) considered where in-phase and out-of-phase tilts do not coexist around any individual pseudo-cubic axis. In all, this irrep analysis by Howard & Stokes (1998, 2002) identified 15 tilt systems including the cubic aristotype, all of which were among the 23 tilt systems listed by Glazer. The remaining eight tilt systems listed by Glazer are either a special case of one of the 15 tilt systems or a complex case where in-phase and out-of-phase tilts are allowed by the symmetry to coexist around one pseudo-cubic axis; details are provided by Howard & Stokes (1998, 2002).

Darlington (2002a, b) and Knight (2009) developed an analysis that is essentially equivalent to that of using irreps, by manually decomposing the tilted perovskite structures in terms of condensed normal modes of the cubic aristotype. By comparing the atomic displacements allowed by the space group of tilted perovskites with the mode displacements associated with *X*, *M* and *R* points, Knight (2009) identified the modes condensed in the 15 tilted perovskite structures. For each of the structures, he found as many modes as the internal degrees of freedom and gave the equation relating the mode amplitudes and the fractional coordinates as well as cell dimensions. The equation for the perovskite structure with $a^+b^-b^-$ tilting and space group *Pbnm* is quoted from Knight (2009) as an example:

$$\begin{pmatrix} 1 & 0 & 0 & 0 & 0 & 0 & 0 \\ 0 & 1 & 0 & 0 & 0 & 0 & 0 \\ 0 & 0 & 1 & 0 & 0 & 0 & -1 \\ 0 & 0 & 0 & 0 & 1 & 0 & 0 \\ 0 & 0 & 0 & -1 & 0 & 1 & 0 \\ 0 & 0 & 0 & 1 & 0 & 1 & 0 \\ 0 & 0 & -1 & 0 & 0 & 0 & -1 \end{pmatrix} \begin{pmatrix} d_1 \\ d_2 \\ d_3 \\ d_4 \\ d_5 \\ d_6 \\ d_7 \end{pmatrix} = \begin{pmatrix} au/\sqrt{2} \\ bv/\sqrt{2} \\ au1/\sqrt{2} \\ bv1/\sqrt{2} \\ \sqrt{2}au2 \\ \sqrt{2}bv2 \\ cw2 \end{pmatrix}. \quad (2.1)$$

The parameters d_i are the mode amplitudes which is the distance of the independent displacement component of the mode in length units (typically Å or *nm*). They are dependent upon the *a*, *b* and *c* unit cell dimensions of the *Pbnm* structure, and the deviations *u*, *v* and *w* of the free fractional coordinates of a set of symmetry independent atoms from the ideal coordinates corresponding to the cubic aristotype. Among the seven mode amplitudes, d_3 and d_4 correspond to the R_4^+ and M_3^+ modes inducing out-of-phase b^-b^- and in-phase a^+ tilts, respectively. Such decompositions explicitly isolate tilting from distortion of the octahedra. The tilt angle around a pseudo-cubic axis can be then calculated by the amplitude of the corresponding octahedral tilt mode:

$$\phi = \arctan\left(2\left(\frac{N}{V}\right)^{1/3} d\right) \quad (2.2)$$

where ϕ is the octahedral tilt angle around a pseudo-cubic axis, *d* is the amplitude of the M_3^+ or R_4^+ mode associated with the axis, *V* is the unit cell volume of the tilted structure, and *N* is the multiplicity of the unit cell compared to the cubic aristotype (Knight, 2009).

2.3.2 Mode analysis using ISOTROPY and ISODISTORT

ISOTROPY (Stokes *et al.*, 2007) can be used to search for displacive modes of *A* and *X* atoms in cubic perovskite and provide a comparison with the results of Cowley (1964). Thus, I searched for irreps at *k*-points *X*, *M* and *R* of space group $Pm\bar{3}m$, carried by modes composed of vectors at Wyckoff *b* and *d* sites occupied by *A* and *X* atoms, respectively. *ISOTROPY* found all the irreps

identified by Knight (2009) in the 15 tilted perovskite structures, for which the basis sets of vectors at Wyckoff *b* or *d* sites shown by *ISOTROPY* suggest the same basis modes as tabulated in Cowley (1964) and Knight (2009) except for irrep X_5^+. The six basis modes of irrep X_5^+ suggested by *ISOTROPY* are linear combinations of those of Cowley's (Table 2.1). It can be easily deduced that the matrix describing this linear relationship can also relate, by similarity transformation, the irrep matrix carried by *ISOTROPY*'s basis modes and that carried by Cowley's basis modes, for each symmetry operation in space group $Pm\bar{3}m$. The two sets of matrices are actually equivalent irreps of X_5^+ according to the group theory. Thus, the broad search for irreps using *ISOTROPY* verifies all the irreps and their basis modes which have been identified by Knight (2009) in the 15 tilted perovskite structures.

Table 2.1 Basis modes of irreps M_2^+, M_3^+, R_3^+, R_4^+, R_5^+ and X_5^+ of space group $Pm\bar{3}m$ [a].

Irrep	Wavevector	*A* cation displacements‡	*X* anion displacements§
M_2^+	$(0, \frac{1}{2}, \frac{1}{2})$		$X_I(z) = - X_{II}(y)$
	$(\frac{1}{2}, 0, \frac{1}{2})$		$X_I(z) = - X_{III}(x)$
	$(\frac{1}{2}, \frac{1}{2}, 0)$		$X_{III}(x) = - X_{II}(y)$
M_3^+	$(0, \frac{1}{2}, \frac{1}{2})$		$X_I(y) = - X_{II}(z)$
	$(\frac{1}{2}, 0, \frac{1}{2})$		$X_I(x) = - X_{III}(z)$
	$(\frac{1}{2}, \frac{1}{2}, 0)$		$X_{II}(x) = - X_{III}(y)$
R_3^+	$(\frac{1}{2}, \frac{1}{2}, \frac{1}{2})$		$X_I(z) = X_{II}(y) = - X_{III}(x)$ $X_I(z) = - X_{II}(y)$
R_4^+	$(\frac{1}{2}, \frac{1}{2}, \frac{1}{2})$		$X_I(y) = - X_{II}(z)$ $X_I(x) = - X_{III}(z)$ $X_{II}(x) = - X_{III}(y)$

R_5^+	$(\frac{1}{2}, \frac{1}{2}, \frac{1}{2})$	A(x) A(y) A(z)	$X_I(y) = X_{II}(z)$ $X_I(x) = X_{III}(z)$ $X_{II}(x) = X_{III}(y)$
X_5^+ (Cowley)	$(0, \frac{1}{2}, 0)$	A(z) A(x)	$X_{II}(z)$ $X_{II}(x)$
	$(0, 0, \frac{1}{2})$	A(x) A(y)	$X_I(x)$ $X_I(y)$
	$(\frac{1}{2}, 0, 0)$	A(y) A(z)	$X_{III}(y)$ $X_{III}(z)$
X_5^+ (ISOTROPY)	$(0, \frac{1}{2}, 0)$	A(z) = - A(x) A(z) = A(x)	$X_{II}(z) = - X_{II}(x)$ $X_{II}(z) = X_{II}(x)$
	$(0, 0, \frac{1}{2})$	A(x) = - A(y) A(x) = A(y)	$X_I(x) = - X_I(y)$ $X_I(x) = X_I(y)$
	$(\frac{1}{2}, 0, 0)$	A(y) = - A(z) A(y) = A(z)	$X_{III}(y) = - X_{III}(z)$ $X_{III}(y) = X_{III}(z)$

[a] Reproduced from Knight (2009). The mode displacements are derived by Cowley (1964). ‡ The *A* cation is at $(\frac{1}{2}, \frac{1}{2}, \frac{1}{2})$ in the cubic unit cell. § I, II and III are used by Cowley to denote the three *X* anions at $(0, 0, \frac{1}{2})$, $(0, \frac{1}{2}, 0)$ and $(\frac{1}{2}, 0, 0)$ in the cubic unit cell, respectively. The *x*, *y* and *z* in parenthesis indicate displacement direction in the cubic lattice. The mode displacements in other unit cells can be deduced from the wavevector of the mode.

Given the parent structure, *ISODISTORT* (Campbell *et al.*, 2006) can decompose a distorted structure with lower symmetry in to symmetry-adapted modes of macroscopic strain, atomic displacement and site occupancy. For each displacive mode condensed in the distorted structure, *ISODISTORT* expresses the displacement directions of affected atoms in terms of the directions in the supercell of the symmetry independent atoms, and hence can be used to relate the mode amplitudes and the fractional coordinates in a form similar to equation (2.1). Note that Knight (2009) incorporates unit cell dimensions *a*, *b* and *c* in to the equations, so the resulting mode amplitudes d_i depend on the cell dimensions. However, *ISODISTORT* describes the superlattice deformation of the distorted structure as macroscopic strain modes, so that the displacive modes

are referred to the basis of the undeformed superlattice which is an exact transformation of the cubic lattice of the aristotype. Thus, the cell parameter changes of the distorted structure are attributed to the strain modes and the displacive mode amplitudes only depend on fractional coordinates. For displacive mode decomposition of perovskites, I can therefore round the cell dimensions a, b and c in equation (2.1) to multiples of that of the cubic aristotype a_p and divide both sides of the equation by a_p. After eliminating the coefficients on the right-hand side, I have:

$$\begin{pmatrix} 1 & 0 & 0 & 0 & 0 & 0 & 0 \\ 0 & 1 & 0 & 0 & 0 & 0 & 0 \\ 0 & 0 & 1 & 0 & 0 & 0 & -1 \\ 0 & 0 & 0 & 0 & 1 & 0 & 0 \\ 0 & 0 & 0 & -\frac{1}{2} & 0 & \frac{1}{2} & 0 \\ 0 & 0 & 0 & \frac{1}{2} & 0 & \frac{1}{2} & 0 \\ 0 & 0 & -\frac{1}{2} & 0 & 0 & 0 & -\frac{1}{2} \end{pmatrix} \begin{pmatrix} d_1' \\ d_2' \\ d_3' \\ d_4' \\ d_5' \\ d_6' \\ d_7' \end{pmatrix} = \begin{pmatrix} u \\ v \\ u1 \\ v1 \\ u2 \\ v2 \\ w2 \end{pmatrix} \tag{2.3}$$

where $d_i' = d_i/a_p$ are clearly now the mode amplitudes in terms of only the changes of the fractional coordinates of the atoms within the unit cell of the cubic aristotype, and do not incorporate the unit cell deformation, so this form of mode decomposition equation follows the separation between strain and displacive modes in *ISODISTORT*.

In fact, the atomic displacement directions in the supercell shown by *ISODISTORT* for each displacive mode just constitute the corresponding column of the square matrix in equation (2.3), except that *ISODISTORT* defines the directions such that the magnitude of the largest component is equal to 1 or -1. For example, for the M_3^+ mode of *X* anions condensed in the *Pbnm* perovskite structure, *ISODISTORT* shows that the symmetry independent X1 anion at (0, 0, $\frac{1}{4}$) does not move while the X2 anion moves from the ideal position ($\frac{1}{4}$, $\frac{1}{4}$, 0) along the [$\bar{1}$10] direction in the supercell. But I cannot simply put these direction components in to the 4th column in equation (2.3) associated with the M_3^+ mode because the numbers in the column should be the coordinate

changes induced by the unit mode amplitude $d_4' = 1$ or $d_4 = a_p$. The supercell lattice vectors of the *Pbnm* structure are [110], [$\bar{1}$10] and [002] in terms of the cubic lattice vectors, so the direction vector [$\bar{1}$10] of the X2 anion in the supercell is actually vector [$\bar{2}$00] in the cubic parent cell. Let's hypothetically assume that the coordinates of the X2 anion change by [$\bar{1}$10] in the supercell, then the mode amplitude would be $d_4 = Fa_p$, $F = 2$, recalling that Knight (2009) defines the mode amplitude as the distance of the independent displacement component. So, the direction vector [$\bar{1}$10] divided by the factor $F = 2$ are the coordinate changes induced by the unit mode amplitude and the resulting $-\frac{1}{2}$ and $\frac{1}{2}$ should be put in to the 5th and 6th positions of the 4th column associated with $u2 = x_{X2} - \frac{1}{4}$ and $v2 = y_{X2} - \frac{1}{4}$, respectively.

Because of the F factor, and the different terminology used by *ISODISTORT*, the mode amplitudes output from *ISODISTORT* must be converted to get the mode amplitudes d_i', which otherwise have to be calculated by solving equation (2.3). *ISODISTORT* outputs the standard supercell-normalized amplitude *As* rather than d defined by Knight (2009). Their relationship is $As = (1/normfactor) \cdot d/(Fa_p)$, where the *normfactor* depends on the structure and Fa_p is the mode amplitude produced by the direction vectors relevant atoms move along. With $d' = d/a_p$, I have

$$d' = As \cdot normfactor \cdot F \,. \tag{2.4}$$

ISODISTORT calculates *As* and *normfactor* for each displacive mode condensed in the input structure, so in practice I can obtain d_i' of each mode by this simple expression rather than solving equation (2.3).

Based on equation (2.3), I add the ideal values of the independent fractional coordinates corresponding to the cubic aristotype on both sides of the equation, so that the mode amplitudes are directly related to the fractional coordinates. The results for all the 15 tilted perovskite structures are listed in Appendix A. The space group settings and Wyckoff positions adopted for the 15 perovskite structures follow Table 5 of Woodward (1997) and Table 1 of Avdeev *et al.* (2007), except that I use $P\bar{1}$ rather than $F\bar{1}$ because *ISODISTORT* does not accept input

structures in space group settings that are not included in the *International Tables for Crystallography*. In Appendix A I omit the prime symbol for *d* and use three subscripts. Other than the Miller and Love (1967) irrep symbol, the first subscript indicates whether the mode involves displacements of *A* cations at cubic Wyckoff *b* sites or *X* anions at *d* sites. The digits in the third subscript indicate which basis modes of the irrep make up the linear combination acting as one symmetry-adapted mode. I should note that the basis modes constituting the symmetry-adapted mode can change if a different subgroup of $Pm\bar{3}m$ is chosen for the tilted perovskite structure containing the mode, which is conjugate to that used in this study. In this case the symmetry operation in $Pm\bar{3}m$ which relates the two conjugate subgroups transforms the domain state used in this study to another. So, the order parameter for each irrep is multiplied by the matrix representing the operation in the irrep and may become a different combination of basis modes. As an independent component of a varying order parameter, the symmetry-adapted mode may also become a different combination of basis modes of the associated irrep, and hence may be denoted by different digits in the third subscript.

After comparing our results of displacive mode decomposition of perovskite with those of Knight (2009), I found general agreement except for three points to note. The first is that Knight uses linear combinations of R_5^+ basis modes $A(x) = A(y)$ and $A(x) = -A(y)$ in the $I2/m$ and $P2_1/m$ ($I112_1/n$ and $P112_1/m$ in Knight (2009)) structures, rather than the R_5^+ basis modes themselves such as $A(x)$, $A(y)$, $A(z)$ in the $P\bar{1}$ ($F\bar{1}$ in Knight (2009)) structure. In these three structures, whether the R_5^+ basis modes or their linear combinations are used affects the relevant part of the mode decomposition equation. The second point is similar; that in the $P2_1/m$ structure the linear combinations of X_5^+ basis modes $X_I(x) = X_I(y)$ and $X_I(x) = -X_I(y)$ *ISODISTORT* uses make the mode decomposition equation a little different from Knight's which involves the X_5^+ basis modes $X_I(x)$ and $X_I(y)$ themselves. The third point is that although Knight did not write the R_3^+ mode in the $I2/a$ ($I2_1/b11$ in Knight (2009)) perovskite structure as a linear combination of basis modes $X_I(z) = X_{II}(y) = -\frac{1}{2}X_{III}(x)$ and $X_I(z) = -X_{II}(y)$ of irrep R_3^+ (Table 2.1), the mode he wrote as $X_{II}(y) = -X_{III}(x)$ is actually a linear combination of the two basis modes as denoted by our

symbol $d_{X,R_3^+,12}$ (Appendix A section g). But if the space group $I2/a$ undergoes a conjugate subgroup transformation (as mentioned previously) through the three-fold rotation around the cubic [111] direction C_{31}^+, the mode $X_{II}(y) = - X_{III}(x)$ would transform to $X_I(z) = - X_{II}(y)$, the second basis mode of irrep R_3^+, and hence the symbol would be $d_{X,R_3^+,2}$ instead of $d_{X,R_3^+,12}$. This is an example of the mode symbol changing with the domain states described by different conjugate subgroups of $Pm\bar{3}m$.

2.4 Polyhedral volume ratio V_A/V_B

2.4.1 V_A/V_B as a function of displacive mode amplitudes

Avdeev *et al.* (2007) derived the formulae for the AX_{12} and BX_6 polyhedral volume ratio V_A/V_B in terms of the fractional coordinates of the *X* anions for the 15 tilted perovskite structures and the $Pm\bar{3}m$ aristotype structure. Note that the unit cell parameters do not appear in the formulae because although they affect the values of V_A and V_B, changes in the unit cell parameters change both polyhedral volumes in the same proportion and the ratio V_A/V_B therefore remains unaffected by the unit cell parameters. Further, because the AX_{12} cuboctahedra and BX_6 octahedra are bounded by *X* anions, the V_A/V_B formulae only contain the fractional coordinates of the *X* anions. If I substitute the lines concerning the *X* anions in the mode decomposition equation in to the V_A/V_B formula of Avdeev *et al.* (2007), I can obtain the V_A/V_B formula in terms of the amplitudes of the displacive modes of the *X* anions. The resulting V_A/V_B formulae for the 15 perovskite structures are shown in Table 2.2. In the *Cmcm*, *I*4/*mmm*, $P2_1/m$, $P4_2/nmc$, $Im\bar{3}$ and *Immm* structures, *A* or *B* cation occupies more than one symmetry independent sites and hence has more than one polyhedral volumes as denoted in Table 1 of Avdeev *et al.* (2007). In these cases, the expression for the ratio of the average polyhedral volumes is used for substitution. As expected, only the modes involving the *X* anions are present in the formulae. All of the formulae have a common general form in which if all of the mode amplitudes in the denominator are zero, V_A/V_B becomes 5, the value in the cubic aristotype structure without any distortion. V_A/V_B can become

smaller or larger than 5 depending on the mode amplitudes. I should note that the V_A/V_B formulae given in Table 2.2 are based on the mode decomposition equations given in Appendix A. If I substitute a mode amplitude d' with - d' in the mode decomposition equation, the resulting V_A/V_B formula would also have the d' replaced by - d'.

Table 2.2 V_A/V_B as a function of mode amplitudes for 15 tilted perovskite structures.

The expression of V_A/V_B following the equal sign is in terms of the amplitudes of all the symmetry-adapted modes of X anions condensed in each tilted perovskite structure and that following the approximately equal sign is in terms of only the tilt mode amplitudes. The mode amplitude is a fraction of a_p, the unit cell dimension of the cubic aristotype. The prime symbol in d' is omitted for tidiness. The three subscripts of d are, in sequence: the relevant atom type, the irrep and the group of digits indicating the linear combination of the corresponding basis modes of the irrep.

---

a $a^0a^0a^0$ No. 221 $Pm\bar{3}m$

$$\frac{V_{\mathrm{A}}}{V_{\mathrm{B}}} = 5$$

---

b $a^-a^-a^-$ No. 167 $R\bar{3}c$

$$\frac{V_{\mathrm{A}}}{V_{\mathrm{B}}} = \frac{6}{1+4\cdot 3d^2_{\mathrm{X},R_4^+,123}} - 1$$

---

c $a^0a^0c^+$ No. 127 $P4/mbm$

$$\frac{V_{\mathrm{A}}}{V_{\mathrm{B}}} = \frac{6}{1+4d^2_{\mathrm{X},M_3^+,1}} - 1$$

---

d $a^0a^0c^-$ No. 140 $I4/mcm$

$$\frac{V_\mathrm{A}}{V_\mathrm{B}} = \frac{6}{1+4d^2_{\mathrm{X},R_4^+,1}} - 1$$

---

e $a^0b^-b^-$ No. 74 *Imma*

$$\frac{V_\mathrm{A}}{V_\mathrm{B}} = \frac{6}{1+8d^2_{\mathrm{X},R_4^+,12} - 8d^2_{\mathrm{X},R_5^+,12}} - 1$$
$$\approx \frac{6}{1+4\cdot 2d^2_{\mathrm{X},R_4^+,12}} - 1$$

---

f $a^0b^-c^-$ No. 12 *I*2/*m* (non-standard setting of *C*2/*m*)

$$\frac{V_\mathrm{A}}{V_\mathrm{B}} = \frac{6}{1+4d^2_{\mathrm{X},R_4^+,1} + 4d^2_{\mathrm{X},R_4^+,2} - 4d^2_{\mathrm{X},R_5^+,1} - 4d^2_{\mathrm{X},R_5^+,2}} - 1$$
$$\approx \frac{6}{1+4\left(d^2_{\mathrm{X},R_4^+,1} + d^2_{\mathrm{X},R_4^+,2}\right)} - 1$$

---

g $a^-b^-b^-$ No. 15 *I*2/*a* (non-standard setting of *C*2/*c*)

$$\frac{V_\mathrm{A}}{V_\mathrm{B}} = \frac{6}{1-4d^2_{\mathrm{X},R_3^+,12} + 8d^2_{\mathrm{X},R_4^+,13} + 4d^2_{\mathrm{X},R_4^+,2} - 8d^2_{\mathrm{X},R_5^+,13}} - 1$$
$$\approx \frac{6}{1+4\left(2d^2_{\mathrm{X},R_4^+,13} + d^2_{\mathrm{X},R_4^+,2}\right)} - 1$$

---

h $a^+b^-b^-$ No. 62 *Pnma*

$$\frac{V_\mathrm{A}}{V_\mathrm{B}} = \frac{6}{1-4d^2_{\mathrm{X},M_2^+,3} + 4d^2_{\mathrm{X},M_3^+,3} + 8d^2_{\mathrm{X},R_4^+,12} - 8d^2_{\mathrm{X},R_5^+,12} + 16\left(d_{\mathrm{X},M_2^+,3} + d_{\mathrm{X},M_3^+,3}\right)\left(d_{\mathrm{X},R_4^+,12} + d_{\mathrm{X},R_5^+,12}\right)d_{\mathrm{X},X_5^+,1}} - 1$$
$$\approx \frac{6}{1+4\left(d^2_{\mathrm{X},M_3^+,3} + 2d^2_{\mathrm{X},R_4^+,12}\right)} - 1$$

---

i $a^+a^+c^-$ No. 137 $P4_2/nmc$

$$\frac{V_\mathrm{A}}{V_\mathrm{B}} = \frac{6}{1+8d^2_{\mathrm{X},M_3^+,23}-4d^2_{\mathrm{X},M_4^+,1}-8d^2_{\mathrm{X},M_4^+,23}+4d^2_{\mathrm{X},R_4^+,1}-16d_{\mathrm{X},M_4^+,1}\left(d^2_{\mathrm{X},M_3^+,23}-d^2_{\mathrm{X},M_4^+,23}\right)} -1$$
$$-16\left(d_{\mathrm{X},M_3^+,23}-d_{\mathrm{X},M_4^+,23}\right)d_{\mathrm{X},R_4^+,1}d_{\mathrm{X},X_5^+,1256}$$
$$\approx \frac{6}{1+4\left(2d^2_{\mathrm{X},M_3^+,23}+d^2_{\mathrm{X},R_4^+,1}\right)}-1$$

j $a^0b^+c^-$ No. 63 $Cmcm$

$$\frac{V_\mathrm{A}}{V_\mathrm{B}} = \frac{6}{1+4d^2_{\mathrm{X},M_3^+,1}-4d^2_{\mathrm{X},M_4^+,1}+4d^2_{\mathrm{X},R_4^+,3}-4d^2_{\mathrm{X},R_5^+,3}-8\left(d_{\mathrm{X},M_3^+,1}-d_{\mathrm{X},M_4^+,1}\right)\left(d_{\mathrm{X},R_4^+,3}-d_{\mathrm{X},R_5^+,3}\right)d_{\mathrm{X},X_5^+,34}} -1$$
$$\approx \frac{6}{1+4\left(d^2_{\mathrm{X},M_3^+,1}+d^2_{\mathrm{X},R_4^+,3}\right)}-1$$

k $a^+b^-c^-$ No. 11 $P2_1/m$

$$\frac{V_\mathrm{A}}{V_\mathrm{B}} = \frac{6}{1+4d^2_{\mathrm{X},M_1^+,3}-4d^2_{\mathrm{X},M_2^+,3}+4d^2_{\mathrm{X},M_3^+,3}-4d^2_{\mathrm{X},M_4^+,3}+4d^2_{\mathrm{X},R_4^+,1}+4d^2_{\mathrm{X},R_4^+,2}-4d^2_{\mathrm{X},R_5^+,1}-4d^2_{\mathrm{X},R_5^+,2}} -1$$
$$+8\begin{pmatrix}\left(d_{\mathrm{X},M_1^+,3}+d_{\mathrm{X},M_2^+,3}+d_{\mathrm{X},M_3^+,3}+d_{\mathrm{X},M_4^+,3}\right)\left(d_{\mathrm{X},R_4^+,1}+d_{\mathrm{X},R_5^+,1}\right)\\+\left(d_{\mathrm{X},M_1^+,3}-d_{\mathrm{X},M_2^+,3}-d_{\mathrm{X},M_3^+,3}+d_{\mathrm{X},M_4^+,3}\right)\left(d_{\mathrm{X},R_4^+,2}-d_{\mathrm{X},R_5^+,2}\right)\end{pmatrix}d_{\mathrm{X},X_5^+,1}$$
$$-8\begin{pmatrix}\left(d_{\mathrm{X},M_1^+,3}+d_{\mathrm{X},M_2^+,3}-d_{\mathrm{X},M_3^+,3}-d_{\mathrm{X},M_4^+,3}\right)\left(d_{\mathrm{X},R_4^+,1}+d_{\mathrm{X},R_5^+,1}\right)\\-\left(d_{\mathrm{X},M_1^+,3}-d_{\mathrm{X},M_2^+,3}+d_{\mathrm{X},M_3^+,3}-d_{\mathrm{X},M_4^+,3}\right)\left(d_{\mathrm{X},R_4^+,2}-d_{\mathrm{X},R_5^+,2}\right)\end{pmatrix}d_{\mathrm{X},X_5^+,2}$$
$$\approx \frac{6}{1+4\left(d^2_{\mathrm{X},M_3^+,3}+d^2_{\mathrm{X},R_4^+,1}+d^2_{\mathrm{X},R_4^+,2}\right)}-1$$

l $a^+a^+a^+$ No. 204 $Im\bar{3}$

$$\frac{V_{\mathrm{A}}}{V_{\mathrm{B}}} = \frac{6}{1+12d^2_{\mathrm{X},M_3^+,123}-12d^2_{\mathrm{X},M_4^+,123}+16\left(3d^2_{\mathrm{X},M_3^+,123}+d^2_{\mathrm{X},M_4^+,123}\right)d_{\mathrm{X},M_4^+,123}} - 1$$
$$\approx \frac{6}{1+4\cdot 3d^2_{\mathrm{X},M_3^+,123}} - 1$$

---

m $a^0b^+b^+$ No. 139 *I*4/*mmm*

$$\frac{V_{\mathrm{A}}}{V_{\mathrm{B}}} = \frac{6}{1+8d^2_{\mathrm{X},M_3^+,23}-4d^2_{\mathrm{X},M_4^+,1}-8d^2_{\mathrm{X},M_4^+,23}-16d_{\mathrm{X},M_4^+,1}\left(d^2_{\mathrm{X},M_3^+,23}-d^2_{\mathrm{X},M_4^+,23}\right)} - 1$$
$$\approx \frac{6}{1+4\cdot 2d^2_{\mathrm{X},M_3^+,23}} - 1$$

---

n $a^+b^+c^+$ No. 71 *Immm*

$$\frac{V_{\mathrm{A}}}{V_{\mathrm{B}}} = \frac{6}{1+4d^2_{\mathrm{X},M_3^+,1}+4d^2_{\mathrm{X},M_3^+,2}+4d^2_{\mathrm{X},M_3^+,3}-4d^2_{\mathrm{X},M_4^+,1}-4d^2_{\mathrm{X},M_4^+,2}-4d^2_{\mathrm{X},M_4^+,3}} - 1$$
$$+16d_{\mathrm{X},M_3^+,3}\left(d_{\mathrm{X},M_3^+,2}d_{\mathrm{X},M_4^+,1}+d_{\mathrm{X},M_3^+,1}d_{\mathrm{X},M_4^+,2}\right)+16\left(d_{\mathrm{X},M_3^+,1}d_{\mathrm{X},M_3^+,2}+d_{\mathrm{X},M_4^+,1}d_{\mathrm{X},M_4^+,2}\right)d_{\mathrm{X},M_4^+,3}$$
$$\approx \frac{6}{1+4\left(d^2_{\mathrm{X},M_3^+,1}+d^2_{\mathrm{X},M_3^+,2}+d^2_{\mathrm{X},M_3^+,3}\right)} - 1$$

---

o $a^-b^-c^-$ No. 2 $P\bar{1}$

$$\frac{V_{\mathrm{A}}}{V_{\mathrm{B}}} = \frac{6}{1+12d^2_{\mathrm{X},R_1^+,1}-3d^2_{\mathrm{X},R_3^+,1}-4d^2_{\mathrm{X},R_3^+,2}+4d^2_{\mathrm{X},R_4^+,1}+4d^2_{\mathrm{X},R_4^+,2}+4d^2_{\mathrm{X},R_4^+,3}-4d^2_{\mathrm{X},R_5^+,1}-4d^2_{\mathrm{X},R_5^+,2}-4d^2_{\mathrm{X},R_5^+,3}} - 1$$
$$\approx \frac{6}{1+4\left(d^2_{\mathrm{X},R_4^+,1}+d^2_{\mathrm{X},R_4^+,2}+d^2_{\mathrm{X},R_4^+,3}\right)} - 1$$

2.4.2 Effect of octahedral tilt modes on V_A/V_B

Of all of the displacive modes of X anions, the M_3^+ and R_4^+ modes can induce in-phase and out-of-phase octahedral tilts respectively and hence are called octahedral tilt modes. The other modes only contribute to the distortion of the octahedra and hence are called octahedral distortion modes. I should emphasise that, even in the absence of octahedral distortion modes, it is possible for the octahedra to be distorted as a consequence of the deviation of the metric from cubic symmetry. These types of distortions are therefore included in the Γ-point strain modes and not in the octahedral distortion modes.

If I keep only the octahedral tilt modes in the V_A/V_B formula and set the octahedral distortion modes to zero, I can obtain the V_A/V_B formula as a function of the amplitudes of the octahedral tilt modes alone. The results for the 15 tilted perovskite structures are shown in Table 2.2 and are indicated by the use of "approximately equal" signs. The resulting formulae are much simpler and have a general form:

$$\frac{V_A}{V_B} = \frac{6}{1+4\sum_i n_i d_i'^2} - 1 \qquad (2.5)$$

where the sum is over all of the condensed octahedral tilts (at most three modes in all tilted perovskite structures), d_i' is the amplitude of the ith octahedral tilt mode which is a linear combination of the basis modes of irrep M_3^+ or R_4^+, and n_i is the number of basis modes involved in the ith mode. Note that the simplified form given in equation (2.5) shows that when only the octahedral tilt modes condense, V_A/V_B is never greater than 5 and it decreases with increasing mode amplitudes, in accord with the experimental observation that the polyhedral volume ratio V_A/V_B can be reduced by octahedral tilting (e.g. Thomas and Beitollahi, 1994; Thomas, 1996, 1998; Angel *et al.*, 2005).

The octahedral tilt modes condensed in each tilted perovskite structure coincide with the tilt system. For example, in the structure with $a^+b^-b^-$ tilting and space group *Pnma*, the M_3^+ and R_4^+ modes are condensed with order parameters (0, 0, $d_{\mathrm{X},M_3^+,3}$) and ($d_{\mathrm{X},R_4^+,12}$, $-d_{\mathrm{X},R_4^+,12}$, 0), which correspond to the in-phase tilt a^+ and the two out-of-phase tilts b^-b^-, respectively. If I denote the

amplitudes of the basis modes, of either irrep M_3^+ or R_4^+, associated with a, b and c pseudo-cubic axes as d_a, d_b and d_c, then I have $d_a = d_{\mathrm{X},M_3^+,3}$, $d_b = d_{\mathrm{X},R_4^+,12}$, $d_c = -d_{\mathrm{X},R_4^+,12}$ and equation (2.5) for $a^+b^-b^-$ (Table 2.2h) can be rewritten as

$$\frac{V_A}{V_B} = \frac{6}{1+4\left(d_a^2 + d_b^2 + d_c^2\right)} - 1. \tag{2.6}$$

It is straightforward to test this form for the remainder of the 15 tilt systems.

Recall equation (2.2) showing the relationship between the octahedral tilt angle around a pseudo-cubic axis and the corresponding octahedral tilt mode. Because I attribute the unit cell deformation of the tilted structure to the strain modes, as in *ISODISTORT*, the unit cell volume can be rounded to the multiple of that of the cubic aristotype, $V = Na_p^3$. Then, equation (2.2) becomes:

$$\phi = \arctan 2d' \tag{2.7}$$

where $d' = d/a_p$, is just one of the d_a, d_b and d_c. If I substitute equation (2.7) in to (2.6) three times, I have

$$\frac{V_A}{V_B} = \frac{6}{1+\tan^2\phi_a + \tan^2\phi_b + \tan^2\phi_c} - 1 \tag{2.8}$$

where ϕ_a, ϕ_b and ϕ_c are the octahedral tilt angles around a, b and c pseudo-cubic axes, respectively. Thus, after neglecting the unit cell deformation of the tilted structure (which does not affect V_A/V_B) and all the octahedral distortion modes, the polyhedral volume ratio V_A/V_B becomes a simple function of the octahedral tilt mode amplitudes or the octahedral tilt angles associated with the three pseudo-cubic axes.

For tilt systems involving a tilt about a single axis equation (2.8) reduces to $V_A/V_B = 6/(1 + \tan^2\phi) - 1$ which is identical to the more common form of $V_A/V_B = 6\cos^2\phi - 1$. The latter can be derived by simple geometry and is a special case of $V_A/V_B = 6\cos^2\theta_m\cos\theta_z - 1$ proposed by Thomas

(1996) for orthorhombic and tetragonal perovskites, where because the octahedra only rotate around the *z* axis, the angle between the *z* axis and the corresponding octahedral stalk θ_z is zero and the other two axis-stalk angles, and hence their average θ_m,is equal to the tilt angle ϕ. For the $a^-a^-a^-$ and $a^+a^+a^+$ tilt systems where the three tilt angles and the three mode amplitudes are equal (*i.e.* $\phi_a = \phi_b = \phi_c = \phi$ and $d_a = d_b = d_c = d'$) equation (2.8) reduces to $V_A/V_B = 6/(1 + 3\tan^2\phi) - 1 = 6/(1 + 12d'^2) - 1$. The rotation angle ω of the octahedra around the [111] axis can be derived as $\tan\omega = 2\sqrt{3}d'$ from the displacements of the octahedral vertices, so by substitution I obtain $V_A/V_B = 6\cos^2\omega - 1$ which was proposed by Thomas & Beitollahi (1994) for rhombohedral perovskites.

2.4.3 Geometric proof

Although equation (2.6) emerges by inspection of the V_A/V_B formulae for all the 15 tilt systems, it can actually be proved quite simply by geometry. Consider the BX_6 octahedron centered at the origin of the unit cell of the cubic aristotype. I use X_a, X_b and X_c to denote the three *X* anions with the fractional coordinates ($\frac{1}{2}$, 0, 0), (0, $\frac{1}{2}$, 0) and (0, 0, $\frac{1}{2}$), respectively. The basis mode, of either irrep M_3^+ or R_4^+, associated with the *a* axis imposes on X_b and X_c displacements (0, 0, d_a) and (0, - d_a, 0), respectively. Similarly, the basis mode associated with *b* axis imposes on X_c and X_a displacements (d_b, 0, 0) and (0, 0, - d_b), respectively and that associated with *c* axis imposes on X_a and X_b displacements (0, d_c, 0) and (- d_c, 0, 0), respectively. If the octahedral distortion modes are not considered, X_a, X_b and X_c are moved by the combination of all three modes to ($\frac{1}{2}$, d_c, - d_b), (- d_c, $\frac{1}{2}$, d_a) and (d_b, - d_a, $\frac{1}{2}$), respectively. The volume of the tetrahedron bounded by X_a, X_b, X_c and the origin *O* can be calculated as

$$V_{OX_aX_bX_c} = \frac{1}{6}\cdot\begin{vmatrix} \frac{1}{2} & -d_c & d_b \\ d_c & \frac{1}{2} & -d_a \\ -d_b & d_a & \frac{1}{2} \end{vmatrix} = \frac{1+4\left(d_a^2+d_b^2+d_c^2\right)}{48} \qquad (2.9)$$

where all lengths are fractions of a_p and the volume is a fraction of a_p^3. The remaining three X anions of the BX_6 octahedron centered at the origin are just related by inversion through the origin to X_a, X_b and X_c. The volumes of these other seven tetrahedra making up the octahedron can be calculated by a determinant as equation (2.9) and the results are all equal to $V_{OX_aX_bX_c}$. So, the octahedral volume is eight times $V_{OX_aX_bX_c}$, and is the same for all of the other octahedra in the super cell of the tilted perovskite. The volume of the AX_{12} cuboctahedra V_A can be obtained by subtracting the octahedral volume V_B from the total volume a_p^3 associated with each cubic lattice point and the polyhedral volume ratio V_A/V_B can be calculated by

$$\frac{V_A}{V_B} = \frac{1 - 8 \cdot V_{OX_aX_bX_c}}{8 \cdot V_{OX_aX_bX_c}} = \frac{6}{1 + 4\left(d_a^2 + d_b^2 + d_c^2\right)} - 1$$

which is just equation (2.6). Although this result is obtained in reference to the cubic lattice, it applies to all tilted perovskites because, as noted above, the deformation of the unit cell has no effect on the volume ratio V_A/V_B.

2.5 Worked Example with *ISODISTORT*

As an example of how to extract the information required to calculate the mode amplitudes and tilt angles from *ISODISTORT*, I use the room-pressure structure of pure $MgSiO_3$ *Pnma* perovskite published by Dobson & Jacobsen (2004). The original structure was published in space group *Pbnm*, so the first step is to transform the published atom coordinates in to *Pnma*. Comparison of the resulting coordinates with those given in Appendix A section h for *Pnma* shows that in addition an origin shift has to be applied to place the *B* cation site (Si) at the origin, and that the oxygen atoms have then to be moved to equivalent positions by the space group operators so that they correspond exactly to those positions listed in Appendix A section h. The resulting coordinate list is given in Table 2.3. The cubic perovskite structure never becomes stable under any conditions for $MgSiO_3$, so a fictive structure has to be constructed to act as a parent reference structure for the *ISODISTORT* program. Note that, although the individual values of *As* and *normfactor* produced by *ISODISTORT* depend on the cell parameter of the cubic parent structure, their product used in equation (2.4) does not. The only requirement is that

the volume strain between the parent structure and the distorted structure is sufficiently small to allow *ISODISTORT* to identify the equivalent atoms, and this can be achieved by setting the unit cell volume of the cubic parent structure equal to the sub-cell volume of the distorted structure (Table 2.3).

Table 2.3 Cif files for the example calculation in section 2.5 [a].

Distorted structure:

```
data_MgSiO3_Pnma_P0_DobsonJacobsen
_space_group_name_H-M_alt 'P n m a'
_diffrn_ambient_pressure           0

_cell_length_a        4.9298(3)
_cell_length_b        6.8990(3)
_cell_length_c        4.7780(2)
_cell_angle_alpha     90.0000
_cell_angle_beta      90.0000
_cell_angle_gamma     90.0000


loop_
    _atom_site_label
    _atom_site_fract_x
    _atom_site_fract_y
    _atom_site_fract_z


Mg  0.55588  0.25000  0.01378
Si  0.00000  0.00000  0.00000
O1  -.03355  0.25000  -.10189
O2  0.79867  0.05258  0.30374
```

Parent structure:

```
data_MgSiO3_Pm_3m_P0
_space_group_name_H-M_alt 'P m -3 m'
_diffrn_ambient_pressure           0

_cell_length_a        3.438
_cell_length_b        3.438
_cell_length_c        3.438
_cell_angle_alpha     90.0000
_cell_angle_beta      90.0000
_cell_angle_gamma     90.0000


loop_
```

```
    _atom_site_label
    _atom_site_fract_x
    _atom_site_fract_y
    _atom_site_fract_z


Mg  0.50000  0.50000  0.50000
Si  0.00000  0.00000  0.00000
O   0.50000  0.00000  0.00000
```

[a] The items with name '_space_group_symop_operation_xyz' in the cif file are needed by *ISODISTORT*. They are omitted here to save space.

Table 2.4 Output from *ISODISTORT*: mode details for the perovskite structure defined in Table 2.3.

Mode [a]	As	normfactor	Atom	dx	dy	dz	*F* factor	d′
R_4^+ (a,-a,0)	1.42368	0.07272	O2	0.0	0.5	0.0	1	0.10353
			O1	0.0	0.0	-1.0		
R_5^+ (a,a,0)	0.02248	0.07272	O2	0.0	0.5	0.0	1	0.00163
			O1	0.0	0.0	1.0		
X_5^+ (a,0,0,0,0,0)	0.32624	0.10284	O2	0.0	0.0	0.0	1	0.03355
			O1	-1.0	0.0	0.0		
M_2^+ (0,0,a)	0.04930	0.05142	O2	-1.0	0.0	1.0	2	0.00507
			O1	0.0	0.0	0.0		
M_3^+ (0,0,a)	0.99585	0.05142	O2	1.0	0.0	1.0	2	0.10241
			O1	0.0	0.0	0.0		

[a] Only those modes involving oxygen displacements are listed in this table. The order parameter for each mode is in the parenthesis.

After loading the structures to *ISODISTORT* , and performing the mode decomposition (Method 4 for the search) with the appropriate basis (in this case $[10\bar{1}]$,[020],[101]), all of the information required for the calculation of mode amplitudes, tilt angles and the polyhedral volume ratios is provided on the 'modes details' page. The values of *As* and *normfactor* for the modes involving

only the oxygen atoms can be copied directly (Table 2.4). The *F* factors have to be calculated by transforming the displacive mode direction vectors back in to the parent sub-cell. For example, for the O2 atom under the R_4^+ mode, the mode direction vector [d*x* d*y* d*z*] is given as $[0\frac{1}{2}0]$ in the supercell, which is equivalent to 0.5 times the basis vector [020] in the parent cubic cell, and is thus [010] . As this is a simple lattice vector, the *F* factor is 1. As it should be, the same result is obtained for R_4^+ if the O1 atom is considered; [d*x* d*y* d*z*] = $[00\bar{1}]$ so in the parent cubic cell this is equal to -1·[101] and thus $[\bar{1}0\bar{1}]$, another simple lattice vector. The *F* factor for the M_3^+ mode is equal to 2, because for O2 [d*x* d*y* d*z*] is given as [101] in the distorted structure, and is thus equal to $[10\bar{1}]$ + [101] in the parent cubic structure or [200] which is twice the cubic lattice vector. All of the displacive mode definitions and *F* factors for the example are listed in Table 2.4.

By inserting the mode amplitudes in to the equations listed in Table 2.2h, the polyhedral volume ratio for this $MgSiO_3$ perovskite structure is calculated as 4.29, but 4.32 when only the tilt modes are considered. The tilt angles can also now be calculated using equation (2.7) as ϕ_a = arctan(2 $d_{X,M_3^+,3}$) = 11.6° and $\phi_b = \phi_c$ = arctan(2 $d_{X,R_4^+,12}$) = 11.7°.

2.6 Experimental data analysis

Review of the expressions given in Table 2.2 for the polyhedral volume ratio V_A/V_B reveals three distinct classes in terms of the relationship to the mode amplitudes. In this section I review selected experimental data for one example from each of these three classes in order to demonstrate how the interplay between the octahedral tilt modes and the octahedral distortion modes controls the variation of the polyhedral volume ratio in each case.

2.6.1 Perovskites without octahedral distortion

There are three tilt systems, apart from the trivial un-tilted case of $Pm\bar{3}m$ symmetry, in which no octahedral distortion modes are allowed: $a^-a^-a^-$ ($R\bar{3}c$), $a^0a^0c^+$ ($P4/mbm$) and $a^0a^0c^-$ ($I4/mcm$). The $R\bar{3}c$ perovskite structure is produced by three out-of-phase tilts of equal magnitude around the

three pseudo-cubic axes. Correspondingly, the out-of-phase tilt R_4^+ mode condensed in the $R\bar{3}c$ structure is a linear combination of the three R_4^+ basis modes with equal magnitude coefficients. The R_4^+ mode amplitude is thus the only internal degree of freedom. The expression for V_A/V_B in terms of the mode amplitude is therefore a simple function of the tilt mode amplitude alone, as it is for the tilt systems $a^0a^0c^+$ and $a^0a^0c^-$ (Table 2.2b-d). For all three of these tilt systems there is a unique relationship between increasing amplitude of the tilt mode and decreasing V_A/V_B ratio.

As an example of a purely-tilted perovskite, consider $LaCrO_3$ perovskite above its orthorhombic to rhombohedral phase transition at approximately 260 °C (Hashimoto *et al.*, 2000). The rhombohedral structure with space group $R\bar{3}c$ was determined by neutron powder diffraction up to 740 °C (Oikawa *et al.*, 2000). I calculated the polyhedral volume ratio V_A/V_B from the only free coordinate x_O in the hexagonal unit cell at each temperature using the formula from Avdeev *et al.* (2007), and the mode amplitude $d_{X,R_4^+,123}$ from *ISODISTORT* following equation (2.4). Figure 2.1 shows that the $LaCrO_3$ experimental data fall on the curve representing the theoretical relationship between the two given in Table 2.2b. As the temperature increases, the octahedral tilt mode amplitude $d_{X,R_4^+,123}$ decreases and the polyhedral volume ratio V_A/V_B increases towards 5, both showing that, as normal for $R\bar{3}c$ perovskite structures, $LaCrO_3$ becomes less tilted at higher temperatures and may eventually transform to the aristotype with $Pm\bar{3}m$ symmetry (e.g. Hofer and Kock, 1993).

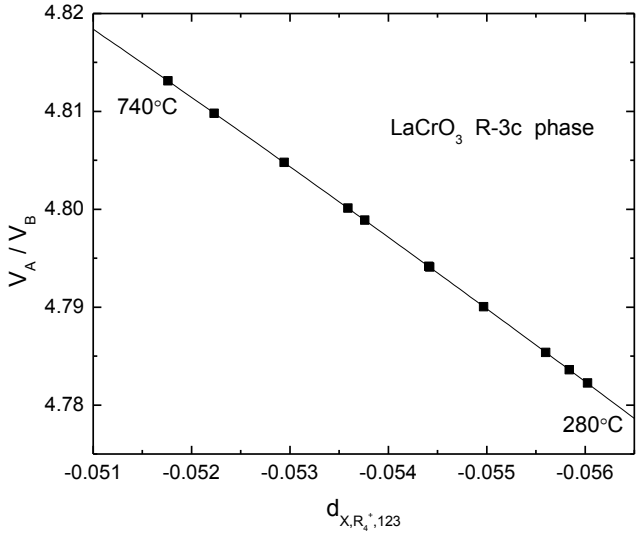

Figure 2.1 Variation of V_A/V_B calculated from the atomic coordinates (Avdeev *et al.*, 2007) with mode amplitude $d_{\mathrm{X},R_4^+,123}$ of the $R\bar{3}c$ phase of $LaCrO_3$ perovskite. The curve is the V_A/V_B ($d_{\mathrm{X},R_4^+,123}$) expression for the $R\bar{3}c$ structure given in Table 2.2b.

2.6.2 Perovskites with separated tilts and distortions

The *Imma* perovskite structure is produced by $a^0b^-b^-$ tilting which is composed of two out-of-phase tilts around two pseudo-cubic axes by an equal angle and no tilt around the third axis. Correspondingly, the out-of-phase tilt R_4^+ mode condensed in the *Imma* structure is a linear combination of two of the three R_4^+ basis modes with equal magnitude coefficients. There is also an octahedral distortion R_5^+ mode which is a linear combination of two of the three R_5^+ basis modes. The V_A/V_B ($d_{\mathrm{X},R_4^+,12}$, $d_{\mathrm{X},R_5^+,12}$) expression for the *Imma* structure (Table 2.2e) is plotted as a surface in Figure 2.2, which shows that V_A/V_B decreases with the octahedral tilt mode amplitude $d_{\mathrm{X},R_4^+,12}$ while it increases with the octahedral distortion mode amplitude $d_{\mathrm{X},R_5^+,12}$. The curve in the $d_{\mathrm{X},R_5^+,12}=0$ plane just displays the decreasing function V_A/V_B ($d_{\mathrm{X},R_4^+,12}$) omitting the octahedral distortion mode amplitude $d_{\mathrm{X},R_5^+,12}$. This same form of complete separation of the

influence of the tilt modes and distortion modes on V_A/V_B is also displayed by two other tilt systems, $a^0b^-c^-$ ($I2/m$) and $a^-b^-b^-$ ($I2/a$) (Table 2.2fg). In all three cases the octahedral distortions always contribute to an increase in V_A/V_B as shown in Figure 2.2.

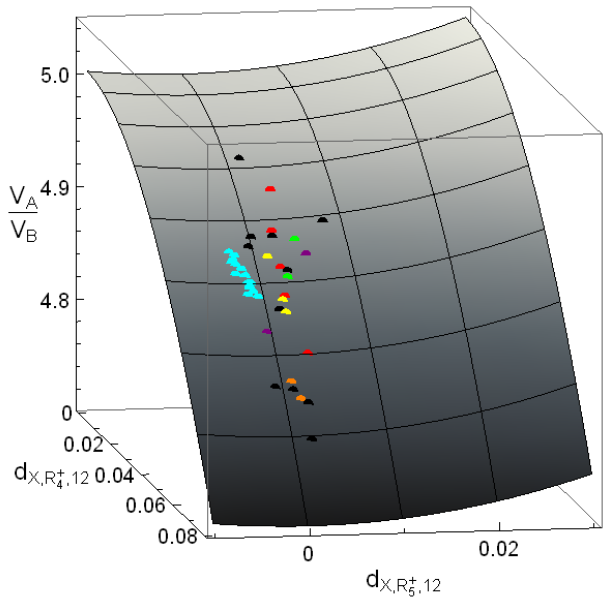

Figure 2.2 Variation of V_A/V_B with mode amplitudes $d_{X,R_4^+,12}$ and $d_{X,R_5^+,12}$ of *Imma* perovskites. The surface is the V_A/V_B ($d_{X,R_4^+,12}$, $d_{X,R_5^+,12}$) expression for the *Imma* structure given in Table 2.2e. The series of dots are $BaPbO_3$ at 4.2 ~ 553 K (red, Fu *et al.*, 2005; Fu *et al.*, 2007), $BaCe_{0.8}Zr_{0.2}O_3$ at 300, 345 K (orange, Pagnier *et al.*, 2000), $SrSnO_3$ at 650 ~ 790 K (cyan, Goodwin *et al.*, 2007), $BaTbO_3$ at 40 ~ 260 K (yellow, Fu *et al.*, 2004), $Sr_{1-x}Ce_xMnO_3$ x = 0.35, 0.40 (purple, Kennedy *et al.*, 2008), $(Na_{0.5}Nd_{0.5})_{1-x}Sr_xTiO_3$ x = 0.3, 0.4 (green, Ranjan *et al.*, 2006). The black dots are $Sr_{0.6}Ba_{0.4}SnO_3$ (Mountstevens *et al.*, 2003), $CeAlO_3$ at 373 K (Fu and IJdo, 2006), $BaCeO_3$ at 573 K (Knight, 1994), $PrAlO_3$ at 185 K (Carpenter *et al.*, 2005), $Ca_{0.4}La_{0.4}TiO_3$ (Zhang *et al.*, 2007), $BaPrO_3$ at 573 K (Saines *et al.*, 2009), $Pr_{0.76}La_{0.24}AlO_3$ at 170 K (Basyuk *et al.*, 2009), $BaCe_{0.80}Y_{0.20}O_{2.9}$ at 773 K (Malavasi *et al.*, 2008), $BaPr_{0.9}Y_{0.1}O_{3-\delta}$ at 573 K (Knee *et al.*, 2009), $0.3La(Mg_{0.5}Ti_{0.5})O_3$-$0.7SrTiO_3$ (Avdeev *et al.*, 2002) and $SrMoO_3$ at 5 K (Macquart *et al.*, 2010).

There are limited experimental data for *Imma* perovskites because they normally only exist as an intermediate phase with a limited temperature range of stability (e.g. Howard *et al.*, 2000), although $BaPbO_3$ (Fu *et al.*, 2005; Fu *et al.*, 2007) appears to be an exception. Experimental structural data of several *Imma* perovskites are added in to the coordinate frame in Figure 2.2. As for the experimental data in Figure 2.1, the V_A/V_B in Figure 2.2 were calculated from the *X* anion coordinates following the formula from Avdeev *et al.* (2007) and the mode amplitudes $d_{\mathrm{X},R_4^+,12}$ and $d_{\mathrm{X},R_5^+,12}$ are calculated from *ISODISTORT*. In Figure 2.2, the experimental points lie on the theoretical surface from Table 2.2e and hence validate the V_A/V_B expression for the *Imma* structure. Note that the series of experimental points are very close to the $d_{\mathrm{X},R_5^+,12}=0$ plane, which shows that in real *Imma* perovskite structures the octahedral distortion mode amplitude $d_{\mathrm{X},R_5^+,12}$ is very small compared to the octahedral tilt mode amplitude $d_{\mathrm{X},R_4^+,12}$. So, it is a good approximation to neglect $d_{\mathrm{X},R_5^+,12}$ in calculating V_A/V_B of an *Imma* structure. For the compositions for which experimental data are available over a range of temperature the octahedral tilt mode amplitude $d_{\mathrm{X},R_4^+,12}$ decreases with increasing temperature. However, while the octahedral distortion mode amplitude $d_{\mathrm{X},R_5^+,12}$ decreases with increasing temperature in some cases such as $BaCe_{0.8}Zr_{0.2}O_3$ and $BaTbO_3$ (Pagnier *et al.*, 2000; Fu *et al.*, 2004), in others such as in $SrSnO_3$ (Goodwin *et al.*, 2007) it increases (Figure 2.2). Nonetheless, the change in the tilt mode amplitude is the greater in all cases so that V_A/V_B increases with increasing temperature as required for the general evolution of the structure towards a higher-symmetry, less tilted, polymorph.

2.6.3 Perovskites with combined tilts and distortions

Seven of the remaining 8 tilt systems have expressions for the volume ratio V_A/V_B that contain three types of terms in the denominator (Table 2.2h-n). In addition to the separate terms in the squares of the individual amplitudes of the tilt and distortion modes found, for example, for *Imma*, the expressions for these tilt systems include third-order products of the amplitudes of both types of modes. As a consequence, the volume ratio of these perovskites can be either larger

or smaller than the V_A/V_B ratio due to tilting alone. The last case, of tilt system $a^-b^-c^-$ ($P\bar{1}$), does not contain these triplets, but terms with different signs that can also lead to the distortional modes increasing or decreasing V_A/V_B (Table 2.2o).

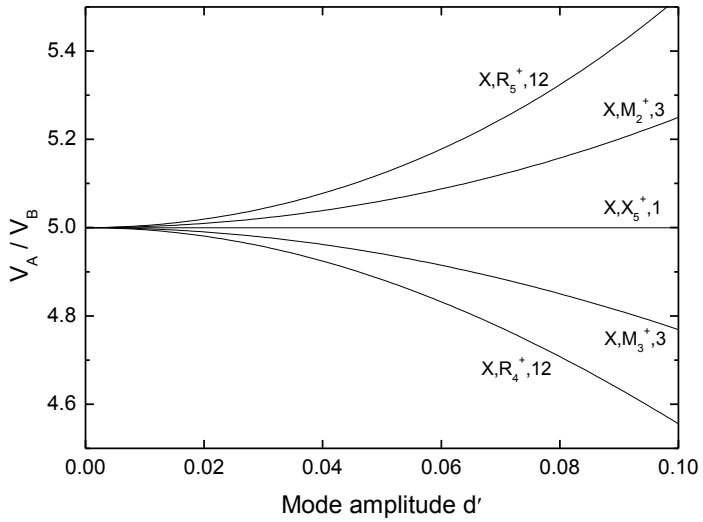

Figure 2.3 Variation of V_A/V_B of *Pnma* perovskite with individual mode amplitudes $d_{\mathrm{X},M_2^+,3}$, $d_{\mathrm{X},M_3^+,3}$, $d_{\mathrm{X},R_4^+,12}$, $d_{\mathrm{X},R_5^+,12}$ or $d_{\mathrm{X},X_5^+,1}$.

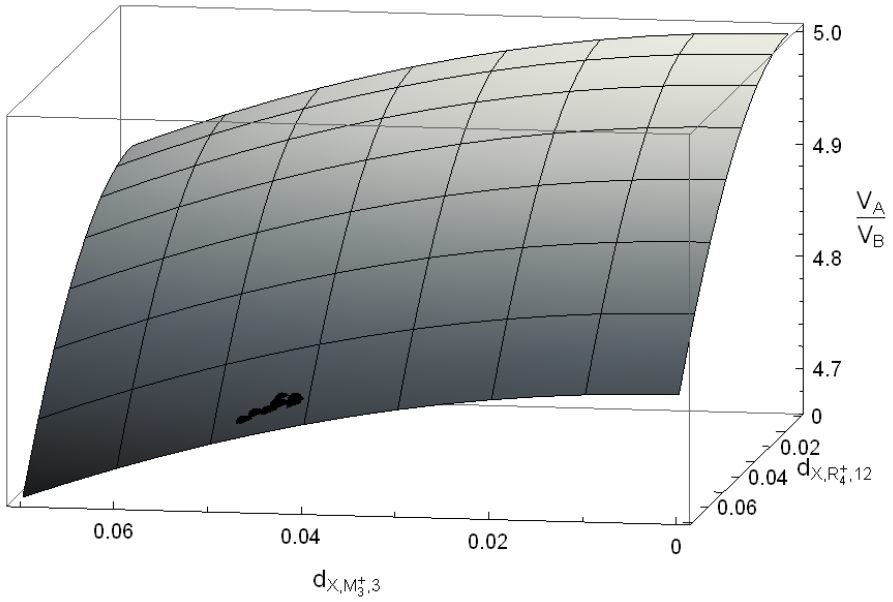

Figure 2.4 Variation of V_A/V_B with octahedral tilt mode amplitudes $d_{X,M_3^+,3}$ and $d_{X,R_4^+,12}$ of the *Pnma* phase of $LaCrO_3$ perovskite. The surface is the V_A/V_B ($d_{X,M_3^+,3}$, $d_{X,R_4^+,12}$) expression for the *Pnma* structure given in Table 2.2h.

The *Pnma* perovskite structure is the most commonly-found tilt system in perovskites. It is produced by $a^+b^-b^-$ tilting which is composed of one in-phase tilt around a pseudo-cubic axis and two out-of-phase tilts around the other two pseudo-cubic axes by an equal angle. Correspondingly, condensed in the *Pnma* structure is an in-phase tilt M_3^+ basis mode and an out-of-phase tilt R_4^+ mode which is a linear combination of two of the three R_4^+ basis modes with equal magnitude coefficients. In addition there are three octahedral distortion modes: an M_2^+ basis mode, a linear combination of two R_5^+ basis modes and an X_5^+ basis mode (Table 2.1). The *Pnma* structure thus has a five-variable function for V_A/V_B. The volume ratio as a function of each individual mode amplitude can be obtained simply by making the other four variables zero. The resulting five single-variable functions plotted in Figure 2.3 show that V_A/V_B decreases with the octahedral tilt mode amplitudes $d_{X,M_3^+,3}$ and $d_{X,R_4^+,12}$ and increases with the octahedral distortion mode amplitudes $d_{X,M_2^+,3}$ and $d_{X,R_5^+,12}$. Note that the mode amplitudes $d_{X,R_4^+,12}$ and

$d_{\mathrm{X},R_5^+,12}$ change V_A/V_B faster than $d_{\mathrm{X},M_2^+,3}$ and $d_{\mathrm{X},M_3^+,3}$ because they both control two basis modes simultaneously. This is obvious when the V_A/V_B is plotted as a function of the two octahedral tilt mode amplitudes $d_{\mathrm{X},M_3^+,3}$ and $d_{\mathrm{X},R_4^+,12}$ in the absence of distortion (Figure 2.4), in which the curves in the $d_{\mathrm{X},R_4^+,12}=0$ and $d_{\mathrm{X},M_3^+,3}=0$ planes are the same as the curves for $d_{\mathrm{X},M_3^+,3}$ and $d_{\mathrm{X},R_4^+,12}$ in Figure 2.3, respectively.

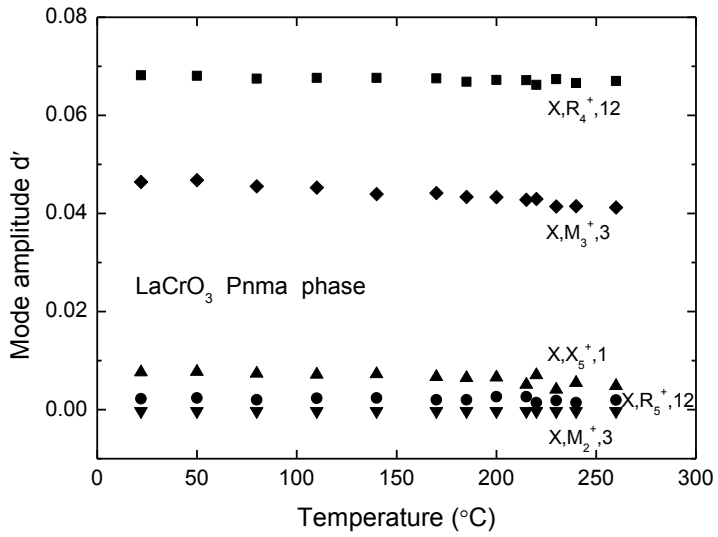

Figure 2.5 Variation of the mode amplitudes $d_{\mathrm{X},M_2^+,3}$, $d_{\mathrm{X},M_3^+,3}$, $d_{\mathrm{X},R_4^+,12}$, $d_{\mathrm{X},R_5^+,12}$ and $d_{\mathrm{X},X_5^+,1}$ with temperature in the *Pnma* phase of $LaCrO_3$ perovskite.

The X_5^+ distortional mode is a special case in this respect. It only appears in the four tilt systems that involve both in-phase and out-of-phase tilts because it is associated with the *X* point in the Brillouin zone. As a consequence its amplitude only appears in product terms with other modes in the expression for the volume ratio V_A/V_B and only in tilt systems $a^+b^-b^-$ (*Pnma*), $a^+a^+c^-$ ($P4_2/nmc$), $a^0b^+c^-$ (*Cmcm*) and $a^+b^-c^-$ ($P2_1/m$) (Table 2.2h-k). Therefore this mode *alone* does not change the volume ratio V_A/V_B away from 5. Conversely, when the amplitude of the X_5^+ mode in

Pnma perovskite is zero, the third-order terms in the expression for V_A/V_B are zero, and the expression reduces to the form discussed in section 2.6.2, so that the polyhedral volume ratio is increased by the other distortional modes from that given by the tilts alone (Table 2.2h).

In real *Pnma* perovskites all of the symmetry-allowed modes have non-zero amplitudes, and the effect of the distortional modes on the value of the volume ratio V_A/V_B depends on a subtle balance between the terms in the squares of the distortion mode amplitudes $d_{\mathrm{X},M_2^+,3}$ and $d_{\mathrm{X},R_5^+,12}$ alone and the third-order product terms. As an example of the more common case in *Pnma* perovskites, I use $LaCrO_3$ perovskite once more but at temperatures below the orthorhombic to rhombohedral phase transition temperature at 260 °C (Hashimoto *et al.*, 2000). The five mode amplitudes $d_{\mathrm{X},M_2^+,3}$, $d_{\mathrm{X},M_3^+,3}$, $d_{\mathrm{X},R_4^+,12}$, $d_{\mathrm{X},R_5^+,12}$ and $d_{\mathrm{X},X_5^+,1}$ were calculated with *ISODISTORT* for the structures down to 22 °C determined by neutron powder diffraction (Oikawa *et al.*, 2000). The results plotted in Figure 2.5 show that the two octahedral tilt mode amplitudes $d_{\mathrm{X},M_3^+,3}$ and $d_{\mathrm{X},R_4^+,12}$ are significantly larger than the three octahedral distortion mode amplitudes $d_{\mathrm{X},M_2^+,3}$, $d_{\mathrm{X},R_5^+,12}$ and $d_{\mathrm{X},X_5^+,1}$. The $d_{\mathrm{X},M_3^+,3}$, $d_{\mathrm{X},R_4^+,12}$ and the V_A/V_B calculated from the *X* anion coordinates of *Pnma* $LaCrO_3$ structures over the experimental temperature range are shown in the coordinate frame in Figure 2.4. An enlargement and re-alignment of this surface in Figure 2.6, shows that the experimental volume ratios are very close (typically within 0.002, but as much as 0.03 for the example of extremely-distorted $MgSiO_3$ perovskite) but smaller than the ratios calculated from the contributions of the tilt modes alone. The fact that the actual volume ratios fall below the surface calculated for tilts alone is the typical case for the perovskites in this class, and indicates that the contribution of the terms in the triplets in the denominator is positive and larger in magnitude than the sum of the terms in the squares of $d_{\mathrm{X},M_2^+,3}$ and $d_{\mathrm{X},R_5^+,12}$. The opposite case occurs when there is a significant M_2^+ distortion, as typically occurs in compounds with Jahn-Teller distorted octahedra such as $LaMnO_3$ (e.g. Rodriguez-Carvajal *et al.*, 1998). In these cases the term in square of $d_{\mathrm{X},M_2^+,3}$ out-weighs the triplet terms and the true V_A/V_B becomes slightly larger (of the order of 0.01) than the value calculated from the amplitudes of the tilt modes alone.

Therefore, even in the presence of significant amplitudes of the distortional modes the octahedral tilt mode amplitudes play a dominant role in changing V_A/V_B because the distortional modes contribute at most a change of the order of 0.03 to the volume ratio, or typically less than 5% of the difference of V_A/V_B from 5. This is in agreement with the observation that the majority of 761 experimental *Pnma* structures have V_A/V_B between 4.4 and 4.8 determined mostly by the tilting (Avdeev *et al.*, 2007). Returning to the example of *Pnma* $LaCrO_3$ perovskite, I also note that it also displays the general trend that as temperature increases both the distortional and tilt modes show a decrease in amplitude and the deviation of the true V_A/V_B from that calculated for the tilts alone becomes smaller (Figure 2.6). So, as in real *Imma* perovskites, for many practical purposes the contributions to the volume ratio from the distortional modes can be neglected.

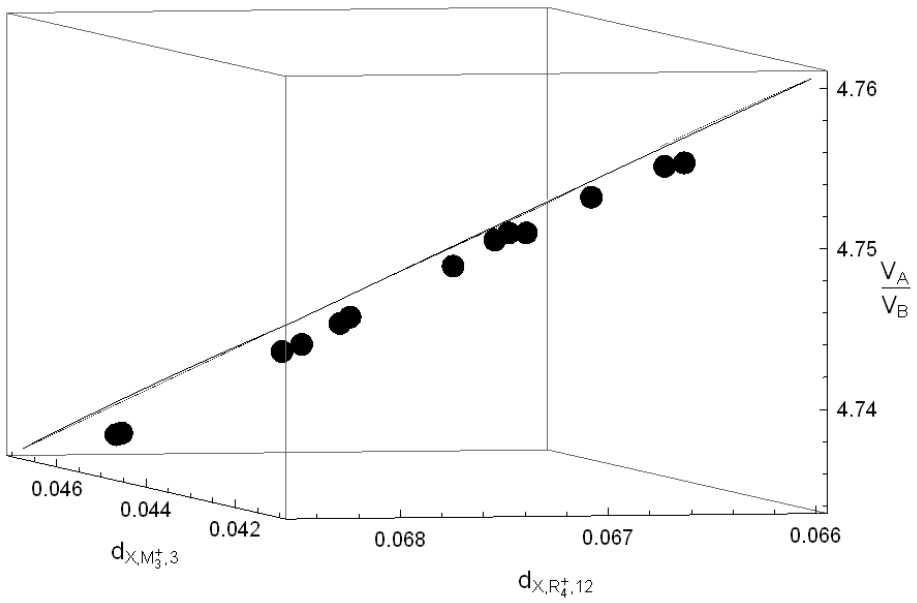

Figure 2.6 The variation of V_A/V_B with octahedral tilt mode amplitudes $d_{\mathrm{X},M_3^+,3}$ and $d_{\mathrm{X},R_4^+,12}$ of *Pnma* phase of $LaCrO_3$ perovskite replotted from Figure 2.4 over a smaller range of mode amplitudes and oriented to view edge-on the surface of V_A/V_B ($d_{\mathrm{X},M_3^+,3}$, $d_{\mathrm{X},R_4^+,12}$) of *Pnma* perovskites given in Table 2.2h.

2.7 Conclusions

I have used the computer programs *ISOTROPY* and *ISODISTORT* to decompose perovskite structures in terms of symmetry-adapted displacive modes following the methodology of Knight (2009). With a new definition $d' = d/a_p$, the mode amplitudes only reflect the internal degrees of freedom of the structure, and not the influence of the deformation of the cell parameters of the supercell away from those of the cubic parent structure. The polyhedral volume ratio V_A/V_B that defines whether a perovskite structure becomes more or less distorted with changes in pressure or temperature, has been defined in terms of the mode amplitudes involving the *X* anions for each of 15 tilt systems. These expressions have been reduced to a simple universal form (equation (2.6)) applicable to all tilt systems by neglecting the octahedral distortion modes and V_A/V_B as a function of the tilt angles about the three pseudo-cubic axes (equation (2.8)) has also been obtained. The dominance of octahedral tilt modes over the distortional modes found in real perovskites justifies the use of the simple uniform expression for most cases.

2.8 References

Andrault D and Poirier J P 1991 Evolution of the distortion of perovskites under pressure: An EXAFS study of $BaZrO_3$, $SrZrO_3$ and $CaGeO_3$ *Phys. Chem. Miner.* **18** 91-105

Angel R J, Zhao J and Ross N L 2005 General rules for predicting phase transitions in perovskites due to octahedral tilting *Phys. Rev. Lett.* **95** 025503

Avdeev M, Caspi E N and Yakovlev S 2007 On the polyhedral volume ratios VA/VB in perovskites ABX_3 *Acta Cryst.* **B63** 363-72

Avdeev M, Seabra M P and Ferreira V M 2002 Structure evolution in $La(Mg_{0.5}Ti_{0.5})O_3$-$SrTiO_3$ system *Mater. Res. Bull.* **37** 1459-68

Basyuk T, Vasylechko L, Fadeev S, Syvorotka I I, Trots D and Niewa R 2009 Phase and structural behaviour of the $PrAlO_3$-$LaAlO_3$ pseudo-binary system *Rad. Phys. Chem.* **78** S97-100

Campbell B J, Stokes H T, Tanner D E and Hatch D M 2006 ISODISPLACE: a web-based tool for exploring structural distortions *J. Appl. Cryst.* **39** 607-14

Carpenter M A 2007 Elastic anomalies accompanying phase transitions in $(Ca,Sr)TiO_3$ perovskites: Part I. Landau theory and a calibration for $SrTiO_3$ *Am. Miner.* **92** 309-27

Carpenter M A, Howard C J, Kennedy B J and Knight K S 2005 Strain mechanism for order-parameter coupling through successive phase transitions in $PrAlO_3$ *Phys. Rev. B* **72** 024118

Carpenter M A, Sinogeikin S V and Bass J D 2010 Elastic relaxations associated with the Pm-3m - R-3c transition in LaAlO3: II. Mechanisms of static and dynamical softening *J. Phys. Condens. Matter* **22** 035404

Cohen R E 1992 Origin of ferroelectricity in perovskite oxides *Nature* **358** 136-8

Cowley R A 1964 Lattice Dynamics and Phase Transitions of Strontium Titanate *Phys. Rev.* **134** A981

Darlington C N W 2002a Normal-mode analysis of the structures of perovskites with tilted octahedra *Acta Cryst.* **A58** 66-71

Darlington C N W 2002b Normal-mode analysis of the structures of perovskites with tilted octahedra. Erratum *Acta Cryst.* **A58** 299-300

Dobson D P and Jacobsen S D 2004 The flux growth of magnesium silicate perovskite single crystals *Am. Miner.* **89** 807-11
Fu W T and IJdo D J W 2006 "Unusual" phase transitions in $CeAlO_3$ *J. Solid State Chem.* **179** 2732-8
Fu W T, Visser D and IJdo D J W 2005 High-resolution neutron powder diffraction study on the structure of $BaPbO_3$ *Solid State Commun.* **134** 647-52
Fu W T, Visser D, Knight K S and IJdo D J W 2004 Temperature-induced phase transitions in $BaTbO_3$ *J. Solid State Chem.* **177** 1667-71
Fu W T, Visser D, Knight K S and IJdo D J W 2007 High-resolution neutron powder diffraction study on the phase transitions in $BaPbO_3$ *J. Solid State Chem.* **180** 1559-65
Glazer A M 1972 The classification of tilted octahedra in perovskites *Acta Cryst.* **B28** 3384-92
Goodwin A L, Redfern S A T, Dove M T, Keen D A and Tucker M G 2007 Ferroelectric nanoscale domains and the 905 K phase transition in $SrSnO_3$: A neutron total-scattering study *Phys. Rev. B* **76** 174114
Hashimoto T, Tsuzuki N, Kishi A, Takagi K, Tsuda K, Tanaka M, Oikawa K, Kamiyama T, Yoshida K, Tagawa H and Dokiya M 2000 Analysis of crystal structure and phase transition of $LaCrO_3$ by various diffraction measurements *Solid State Ionics* **132** 181-8
He T, Huang Q, Ramirez A P, Wang Y, Regan K A, Rogado N, Hayward M A, Haas M K, Slusky J S, Inumara K, Zandbergen H W, Ong N P and Cava R J 2001 Superconductivity in the non-oxide perovskite $MgCNi_3$ *Nature* **411** 54-6
Hofer H E and Kock W F 1993 Crystal Chemistry and Thermal Behavior in the $La(Cr,Ni)O_3$ Perovskite System *J. Electrochem. Soc.* **140** 2889-94
Howard C J, Knight K S, Kennedy B J and Kisi E H 2000 The structural phase transitions in strontium zirconate revisited *J. Phys. Condens. Matter* **12** L677-83
Howard C J and Stokes H T 1998 Group-Theoretical Analysis of Octahedral Tilting in Perovskites *Acta Cryst.* **B54** 782-9
Howard C J and Stokes H T 2002 Group-Theoretical Analysis of Octahedral Tilting in Perovskites. Erratum *Acta Cryst.* **B58** 565
Howard C J and Stokes H T 2004 Octahedral tilting in cation-ordered perovskites - a group-theoretical analysis *Acta Cryst.* **B60** 674-84
Kennedy B J, Saines P J, Zhou Q, Zhang Z, Matsuda M and Miyake M 2008 Structural and electronic phase transitions in $Sr_{1-x}Ce_xMnO_3$ perovskites *J. Solid State Chem.* **181** 2639-45
Knee C S, Magraso A, Norby T and Smith R I 2009 Structural transitions and conductivity of $BaPrO_3$ and $BaPr_{0.9}Y_{0.1}O_3$ *J. Mater. Chem.* **19** 3238-47
Knight K S 1994 Structural phase transitions in $BaCeO_3$ *Solid State Ionics* **74** 109-17
Knight K S 2009 Parameterization of the crystal structures of centrosymmetric zone-boundary-tilted perovskites: an analysis in terms of symmetry-adapted basis-vectors of the cubic aristotype phase *Can. Mineral.* **47** 381-400
Liu L G 1976 Orthorhombic perovskite phases observed in olivine, pyroxene and garnet at high pressures and temperatures *Phys. Earth Planet. Inter.* **11** 289-98
Macquart R B, Kennedy B J and Avdeev M 2010 Neutron diffraction study of phase transitions in perovskite-type strontium molybdate $SrMoO_3$ *J. Solid State Chem.* **183** 249-54
Malavasi L, Ritter C and Chiodelli G 2008 Correlation between Thermal Properties, Electrical Conductivity, and Crystal Structure in the $BaCe_{0.80}Y_{0.20}O_{2.9}$ Proton Conductor *Chem. Mater.* **20** 2343-51
Mao H K, Yagi T and Bell P M 1977 (Washington DC: Carnegie Institution) pp 502-4
Megaw H D 1966 ed V Dvorak*, et al.* (Prague: Institute of Physics of the Czechoslovak Academy of Sciences) pp 314-21
Miller S C and Love W F 1967 *Tables of irreducible representations of space groups and co-representations of magnetic space groups* (Boulder: Preutt)

Mountstevens E H, Attfield J P and Redfern S A T 2003 Cation-size control of structural phase transitions in tin perovskites *J. Phys. Condens. Matter* **15** 8315-26
Oikawa K, Kamiyama T, Hashimoto T, Shimojyo Y and Morii Y 2000 Structural Phase Transition of Orthorhombic $LaCrO_3$ Studied by Neutron Powder Diffraction *J. Solid State Chem.* **154** 524-9
Pagnier T, Charrier-Cougoulic I, Ritter C and Lucazeau G 2000 A neutron diffraction study of $BaCe_xZr_{1-x}O_3$ *Eur. Phys. J. Appl. Phys.* **9** 1-9
Perez-Mato J M, Orobengoa D and Aroyo M I 2010 Mode crystallography of distorted structures *Acta Cryst.* **A66** 558-90
Ranjan R, Agrawal A, Senyshyn A and Boysen H 2006 Phases in the system $Na_{1/2}Nd_{1/2}TiO_3$–$SrTiO_3$: a powder neutron diffraction study *J. Phys. Condens. Matter* **18** 9679-90
Reid A F and Ringwood A E 1975 High‐Pressure Modification of $ScAlO_3$ and Some Geophysical Implications *J. Geophys. Res.* **80** 3363-70
Ringwood A E 1962 Mineralogical Constitution of the Deep Mantle *J. Geophys. Res.* **67** 4005-10
Rodriguez-Carvajal J, Hennion M, Moussa F, Moudden A H, Pinsard L and Revcolevschi A 1998 Neutron-diffraction study of the Jahn-Teller transition in stoichiometric $LaMnO_3$ *Phys. Rev. B* **57** R3189-92
Saines P J, Kennedy B J and Smith R I 2009 Structural phase transitions in $BaPrO_3$ *Mater. Res. Bull.* **44** 874-9
Stokes H T, Hatch D M and Campbell B J 2007 ISOTROPY.
Tamazyan R and van Smaalen S 2007 Quantitative description of the tilt of distorted octahedra in ABX_3 structures *Acta Cryst.* **B63** 190-200
Thomas N W 1996 The compositional dependence of octahedral tilting in orthorhombic and tetragonal perovskites *Acta Cryst.* **B52** 16-31
Thomas N W 1998 A New Global Parameterization of Perovskite Structures *Acta Cryst.* **B54** 585-99
Thomas N W and Beitollahi A 1994 Inter-relationship of octahedral geometry, polyhedral volume ratio and ferroelectric properties in rhombohedral perovskites *Acta Cryst.* **B50** 549-60
Uher C 1990 Thermal conductivity of high-Tc superconductors *J. Supercond.* **3** 337-89
Woodward P M 1997 Octahedral Tilting in Perovskites. I. Geometrical Considerations *Acta Cryst.* **B53** 32-43
Zhang Z, Lumpkin G R, Howard C J, Knight K S, Whittle K R and Osaka K 2007 Structures and phase diagram for the system $CaTiO_3$-$La_{2/3}TiO_3$ *J. Solid State Chem.* **180** 1083-92
Zhao J, Ross N L and Angel R J 2004 New view of the high-pressure behaviour of $GdFeO_3$-type perovskites *Acta Cryst.* **B60** 263-71

Chapter 3: Phase transition and elasticity of $LaAlO_3$ perovskite at high pressures: a first-principles and Landau study

3.1 Abstract

First-principles plane-wave pseudopotential calculations were used to investigate the $R\bar{3}c$ – $Pm\bar{3}m$ phase transition and elasticity of $LaAlO_3$ perovskite at high pressures. The variation of the AlO_6 octahedral tilt angle, relative volumes and enthalpies all confirmed the second-order character of the phase transition. A transition pressure of about 14 GPa was obtained by the pressure variation of the frequency of the soft *R*-point mode in the $Pm\bar{3}m$ structure. Elastic moduli were inverted from the calculated stress-strain data by the singular value decomposition method. The structures, enthalpies and phonon frequencies from first-principles calculations were used to calibrate the Landau parameters of the phase transition for the first time. The results were tested using the elastic moduli.

3.2 Introduction

$LaAlO_3$ perovskite has the rhombohedral $R\bar{3}c$ structure at ambient conditions (e.g. Zhao *et al.*, 2004). The distorted perovskite structure comes from the cubic $Pm\bar{3}m$ aristotype by rotations of the AlO_6 octahedra along the [111] cubic axis, or equivalently, by equal out-of-phase octahedral tiltings along the three cubic axes and so has the $a^-a^-a^-$ tilt system (Glazer, 1972). The ambient $R\bar{3}c$ structure has been found to transform to the $Pm\bar{3}m$ structure at 14 – 15 GPa by Raman spectroscopy, synchrotron X-ray diffraction and first-principles calculation (Bouvier and Kreisel, 2002; Guennou *et al.*, 2011; Tohei *et al.*, 2005). The $R\bar{3}c$ – $Pm\bar{3}m$ phase transition also occurs at 813 – 817 K as found by differential scanning calorimetry measurements (Bueble *et al.*, 1998; Hayward *et al.*, 2005). The elasticity of $LaAlO_3$ perovskite has previously been investigated by Brillouin scattering measurements (Carpenter *et al.*, 2010b) and first-principles calculation (Luo and Wang, 2008).

Although the $R\bar{3}c - Pm\bar{3}m$ phase transition was allowed to be of second order by group theory (Howard and Stokes, 1998), and experiments show it to be at least close to second order (Guennou *et al.*, 2011), the previous first-principles calculation showed a volume drop accompanied with the phase transition at high pressures (Luo and Wang, 2008), which is a sign of the first-order phase transition. This needs to be reexamined from the first-principles perspective. Carpenter *et al.* (2010b) analyzed the high-temperature $R\bar{3}c - Pm\bar{3}m$ using Landau theory in combination with various experimental data. A similar analysis can be done for the phase transition at high pressures based on the first-principles calculations.

3.3 Calculation

3.3.1 Method

All of the calculations were performed using the plane-wave pseudopotential (PW-PP) method based on the density functional theory (DFT) (Hohenberg and Kohn, 1964) implemented in the Quantum ESPRESSO suite (Giannozzi *et al.*, 2009). I used the local density approximation (LDA) with the exchange-correlation functional of Ceperley and Alder (1980) as parameterized by Perdew and Zunger (1981).

The norm-conserving pseudopotentials were generated for La, Al and O atoms using the Troullier-Martins method (Troullier and Martins, 1991) implemented in the ATOMIC code included in the Quantum ESPRESSO suite (Giannozzi *et al.*, 2009). The valence electron configurations for La, Al and O are $4f^{0}5s^{2}5p^{6}5d^{1}6s^{2}6p^{0}$, $3s^{2}3p^{1}3d^{0}$ and $2s^{2}2p^{4}3d^{0}$ respectively, with corresponding cutoff radii 1.7, 1.4, 1.5, 2.0, 1.4, 1.5 Bohr for La, 1.6, 1.6, 1.6 Bohr for Al, and 1.2, 1.3, 1.4 Bohr for O, following their valence electron sequences. A pseudized all-electron potential was used as the local potential of La and the $3d$ potentials were used as the local potentials of Al and O (Kleinman and Bylander, 1982). Bound and unbound states were used for the angular momenta s, p, d, f of La, and s, p of Al and O to improve the transferability of the pseudopotentials.

A 4×4×4 special k-point grid (Monkhorst and Pack, 1976) with half-step shifts in three directions was used in the Brillouin zone sampling for both $R\bar{3}c$ and $Pm\bar{3}m$ phases. The kinetic energy cutoff for plane waves was chosen to be 100 Ry, where the total energy convergence with respect to the cutoff energy is ~0.5 mRy per atom per 10 Ry and the pressure convergence is ~0.15 GPa per 10 Ry.

Variable cell shape molecular dynamics (Wentzcovitch, 1991) was used in the structural relaxations of the $R\bar{3}c$ and $Pm\bar{3}m$ phases between −6 and 20 GPa at 2 GPa intervals. The phonons of the optimized structures were calculated using the density functional perturbation theory (Baroni *et al.*, 2001). The dynamical matrices were calculated on a 4×4×4 q-point grid for both $R\bar{3}c$ and $Pm\bar{3}m$ phases.

3.3.2 Structural evolution

The optimized structures of $R\bar{3}c$ and $Pm\bar{3}m$ phases at 0 GPa are compared with previous experimental and theoretical results (Table 3.1). For the $R\bar{3}c$ phase, our hexagonal unit cell parameters *a* and *c* are ~1.6% smaller than the experimental results, while the ratio *c*/*a* is in better agreement with experiments than other theoretical results are. Our *x*(O) is in the middle of the two experimental values. For the $Pm\bar{3}m$ phase, the unit cell parameter *a* was measured to be 3.8106(1) at 821 K (Howard *et al.*, 2000) and 3.7099(2) at 15.35(10) GPa (Guennou *et al.*, 2011), thus the value at ambient condition should be in between. Ours and other theoretical results are all within this region while ours is smaller than others by less than ~1.7%.

The structural evolution of $R\bar{3}c$ $LaAlO_3$ perovskite with pressure can be examined by the bond lengths, bond angle and tilt angles. The lengths of the three symmetry independent La-O bonds get closer with increasing pressure, showing that the distortion from the cubic perovskite structure gets smaller (Figure 3.1). The symmetry independent Al-O bond gets shorter with increasing pressure (Figure 3.1) and the symmetry independent O-Al-O bond angle approaches 90° (Figure 3.2), showing that the AlO_6 octahedra have a more regular shape while getting smaller with increasing pressure. The pseudo-cubic cell angle α_{pc} approaches 90° with increasing

pressure showing that the pseudo-cubic cell of the rhombohedral perovskite approaches the ideal cubic one (Figure 3.3).

The tilt system of $R\bar{3}c$ $LaAlO_3$ perovskite is $a^-a^-a^-$ where the AlO_6 octahedra rotate around three pseudo-cubic axes by an equal angle (Glazer, 1972; Howard and Stokes, 1998). The equal tilt angle φ around the [100], [010] and [001] pseudo-cubic axes results in an overall tilt angle ϕ around the [111] body diagonal. The tilt angle φ was calculated using

$$\varphi = \arctan 2d', \tag{3.1}$$

where d' is the amplitude of the symmetry-adapted R_4^+ mode (Chapter 2), which equals x(O) − 1/2 in this case. The overall tilt angle ϕ around [111] cubic was calculated using

$$\phi = \arctan 2\sqrt{3}d', \tag{3.2}$$

which was derived from Equation (3.1) as described in Chapter 2 and is equivalent to the equation of Howard *et al.* (2000). Both tilt angles decrease towards 0° with increasing pressure showing a trend towards the cubic perovskite structure (Figure 3.4). The two tilt angle curves together with those of the La-O bond lengths and the O-Al-O bond angle suggest that $LaAlO_3$ perovskite undergoes a $R\bar{3}c$ to $Pm\bar{3}m$ phase transition between 14 and 16 GPa.

Table 3.1 Unit cell parameters and atomic position of $R\bar{3}c$ and $Pm\bar{3}m$ $LaAlO_3$ perovskites at 0 GPa.

	$R\bar{3}c$					$Pm\bar{3}m$
	a (Å)	*c* (Å)	*c*/*a*	*V* (Å^3)	*x*(O) [a]	*a* (Å)
This work	5.279	12.895	2.442	311.261	0.5258	3.725
XRD [b]	5.36603(15)	13.1105(6)	2.443	326.86(4)	0.5265(5)	
Neutron [c]	5.3647(1)	13.1114(3)	2.444	326.79[j]	0.5251(2)	
XRD [d]	5.3619(1)	13.1045(1)	2.444	326.28[j]		
LDA [e]	5.331[i]	12.955[i]	2.430	318.86[j]	0.538[i]	3.79
GGA [f]	5.370	13.139	2.447	328.071		3.753

LDA [g]	3.744
LDA [h]	3.79

[a] Hexagonal setting is used, where atomic fractional coordinates are La (0 0 1/4), Al (0 0 0) and O (x 0 1/4). [b] Zhao *et al.* (2004). [c] Howard *et al.* (2000). [d] Taspinar and Cuneyt Tas (1997). [e] Vali (2008). [f] Stands for generalized gradient approximation, Luo and Wang (2008). [g] Lee and Demkov (2007). [h] PW-PP result of Boudali *et al.* (2009). [i] Converted from rhombohedral setting by present authors. [j] Calculated according to a and c by present authors.

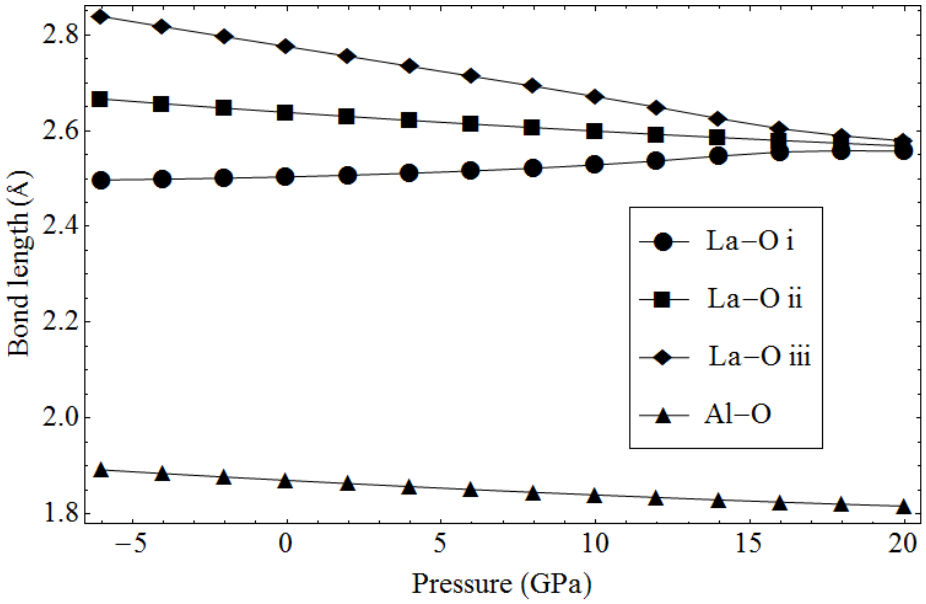

Figure 3.1 Bond lengths of $R\bar{3}c$ $LaAlO_3$ perovskite as a function of pressure.

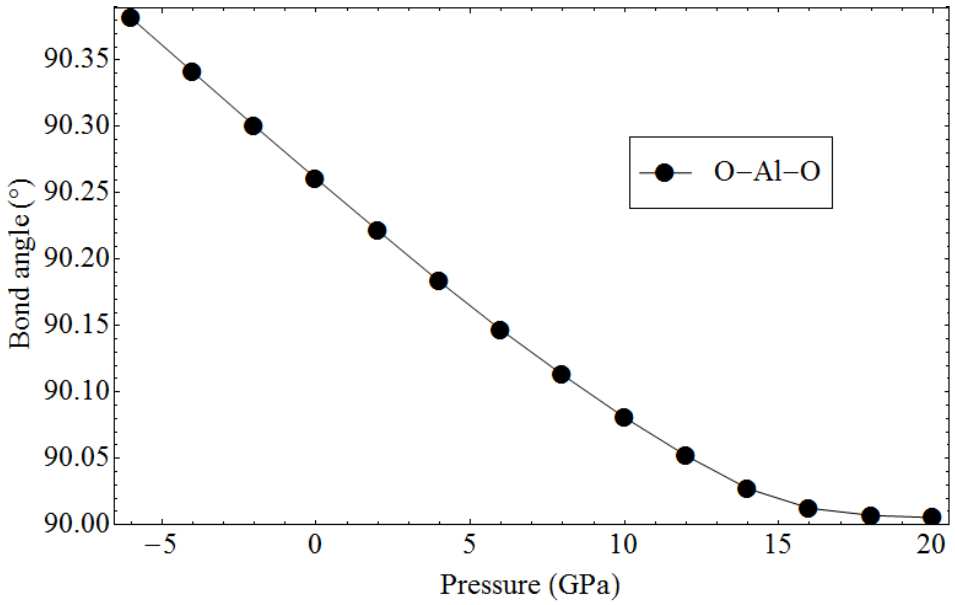

Figure 3.2 O-Al-O bond angle of $R\bar{3}c$ $LaAlO_3$ perovskite as a function of pressure.

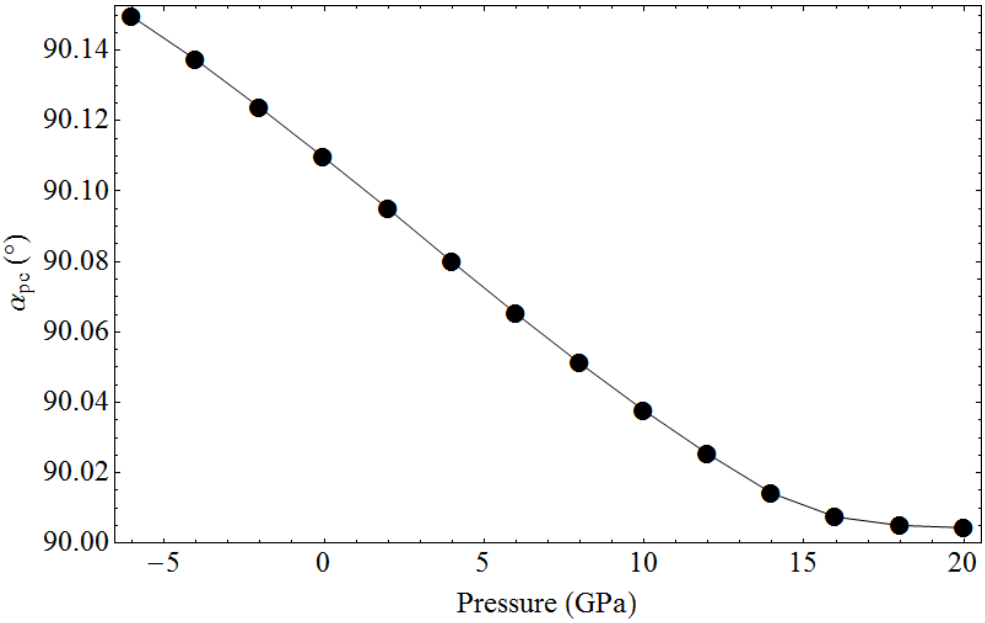

Figure 3.3 Pseudo-cubic lattice angle α_{pc} of $R\bar{3}c$ $LaAlO_3$ perovskite as a function of pressure.

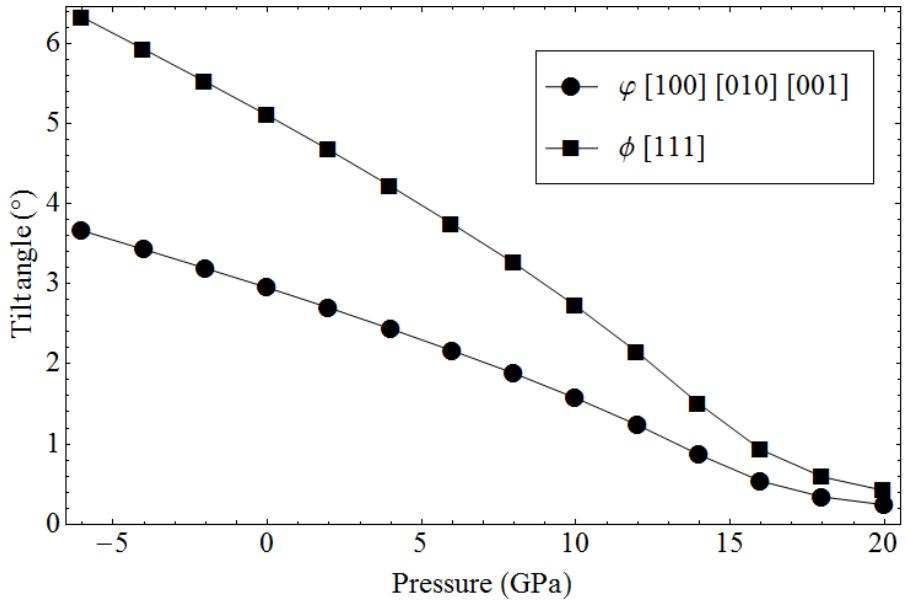

Figure 3.4 Tilt angles of the AlO_6 octahedra of $R\bar{3}c$ $LaAlO_3$ perovskite as a function of pressure.

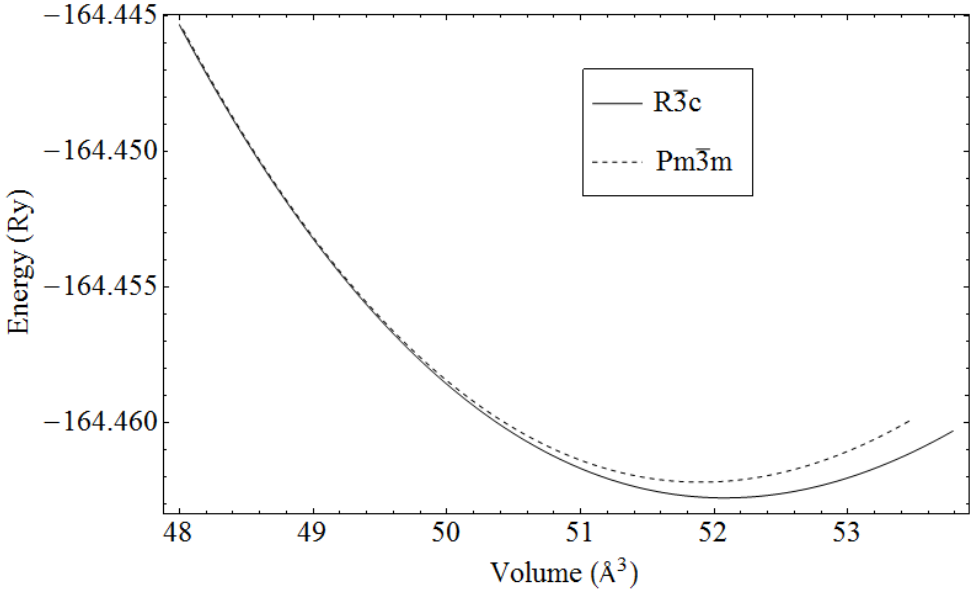

Figure 3.5 Total energy of $R\bar{3}c$ and $Pm\bar{3}m$ $LaAlO_3$ perovskites as a function of volume per formula unit.

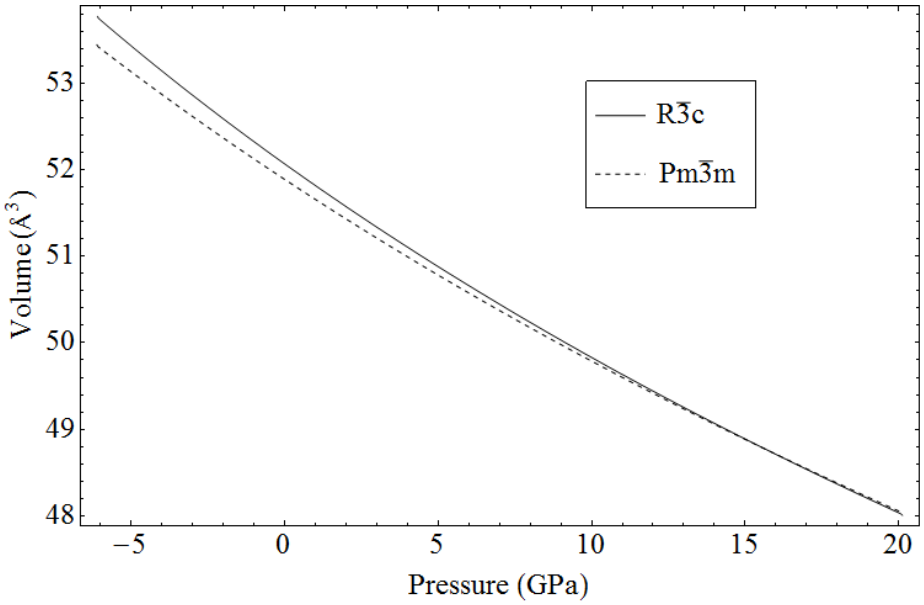

Figure 3.6 Volume per formula unit of $R\bar{3}c$ and $Pm\bar{3}m$ $LaAlO_3$ perovskites as a function of pressure.

3.3.3 Equation of state

The *E*-*V* curves of $R\bar{3}c$ and $Pm\bar{3}m$ phases were obtained by interpolating the total energy of the optimized structures between −6 and 20 GPa at 2 GPa intervals onto dense volume grid (Figure 3.5). The *E*-*V* curve of the $R\bar{3}c$ phase is below that of $Pm\bar{3}m$ at bigger volumes in agreement with that the $R\bar{3}c$ phase is stable at low pressures. The two curves become coincident at smaller volumes in agreement with that the $R\bar{3}c$ phase transits to $Pm\bar{3}m$ at high pressures. From the *E*-*V* curves, pressure was calculated by finite difference $-\mathrm{d}E/\mathrm{d}V$ at each volume grid point and the *V*-*P* curves were obtained for $R\bar{3}c$ and $Pm\bar{3}m$ phases (Figure 3.6). As expected from the *E*-*V* curves, the two *V*-*P* curves become coincident at high pressures. Enthalpy was calculated by $H = E + PV$ at each volume grid point and *H*-*P* curves were obtained for $R\bar{3}c$ and $Pm\bar{3}m$ phases. To see the enthalpy difference between the two phases as a function of pressure, the two *H*-*P* curves were interpolated onto one dense pressure grid and the ΔH-*P* curve was obtained by subtracting the enthalpy of the $R\bar{3}c$ phase from that of the $Pm\bar{3}m$ phase at each pressure grid point (Figure

3.7). The Δ*H-P* curve gradually approaches zero which is a characteristic of a second-order transition.

Notice that the Δ*H-P* curve is still ~0.06 mRy from zero above ~14 GPa. The reason for Δ*H* not being exactly zero is that during the DFT calculations the k-point grids used for $R\bar{3}c$ and $Pm\bar{3}m$ phases have different density with respect to the number of atoms or formula unit. For the $R\bar{3}c$ phase, the reciprocal cell of the rhombohedral unit cell with two formula units was sampled by 4×4×4, while for the $Pm\bar{3}m$ phase, its reciprocal cell was also sampled by 4×4×4 but the $Pm\bar{3}m$ unit cell only contains one formula unit. It is, however, reassuring that ~0.06 mRy per formula unit is even smaller than the total energy variation caused by changing 1 Ry in the kinetic energy cutoff. Luo and Wang (2008) obtained *E-V*, *V-P* and Δ*H-P* curves of $R\bar{3}c$ and $Pm\bar{3}m$ phases from DFT full-potential linearized augmented plane-wave calculation. Their Δ*H-P* curve crosses zero at 15.4 GPa and the *V-P* curves of the two phases do not get closer towards the transition pressure, hence their results suggest a first-order phase transition rather than a second-order one. One possible reason for this might lie in their partially manual procedure of the structural optimization for the $R\bar{3}c$ phase.

Table 3.2 Bulk modulus and its pressure derivative from fit of the equation of state.

	$R\bar{3}c$		$Pm\bar{3}m$	
	K_0	K'_0	K_0	K'_0
This work *E-V*	205.43	4.45	221.01	4.19
This work *P-V*	208.66	4.33	223.24	4.18
XRD[a]	196(2)	4	215(4)	3.6(1)
XRD[b]	190(5)	7.2(4)		
XRD[c]	177(4)	8.9(1.6)		
LDA[d]	192.9364	4.1506	194.0217	4.1209
LDA[e]			228	4
GGA[f]			199.24	4.20

[a] Guennou *et al.* (2011). [b] Bouvier and Kreisel (2002). [c] Zhao *et al.* (2004). [d] Luo and Wang (2008). [e] Lee and Demkov (2007). [f] PW-PP result of Boudali *et al.* (2009).

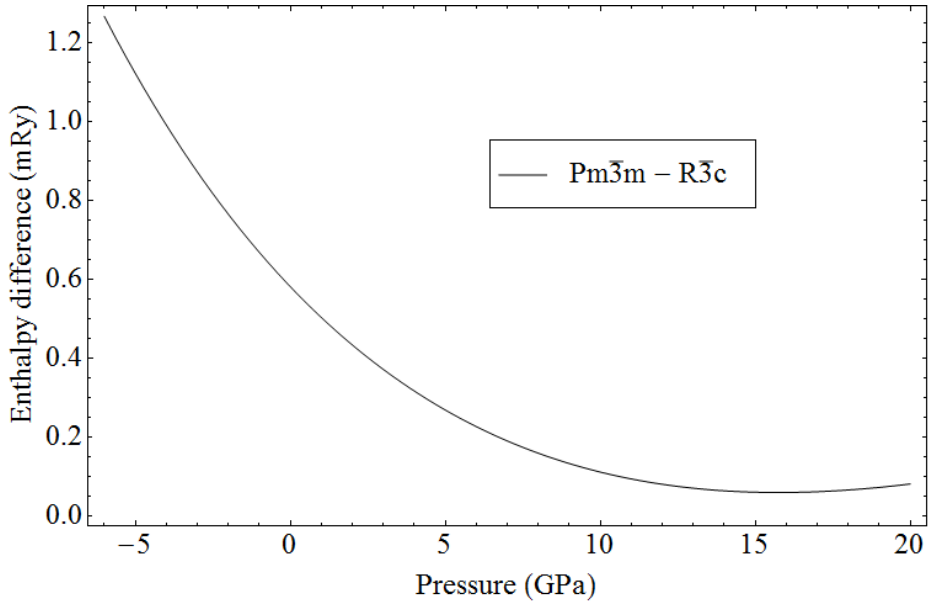

Figure 3.7 Enthalpy difference per formula unit between $R\bar{3}c$ and $Pm\bar{3}m$ $LaAlO_3$ perovskites as a function of pressure.

3.3.4 Phonons

The phonon dispersion of the $R\bar{3}c$ phase was calculated along a path in the Brillouin zone connecting high symmetry k-points Γ (0,0,0), L (0,0.5,0), F (0,0.5,0.5) and Z (0.5,0.5,0.5) expressed as fractions of three reciprocal lattice vectors. For the $Pm\bar{3}m$ phase, k-points Γ (0,0,0), X (0,0.5,0), M (0.5,0.5,0) and R (0.5,0.5,0.5) were used. The phonon dispersions of the $Pm\bar{3}m$ and $R\bar{3}c$ phases at 0 GPa agree with those of Vali (2008) in spite that a different k-point path was used for the $Pm\bar{3}m$ phase here (Figure 3.8, Figure 3.10).

At 0 GPa, the $Pm\bar{3}m$ phase has imaginary phonon frequencies at the zone-boundary R point (Figure 3.8), which is from the triply degenerate F_{2u} mode involving the rotation of the AlO_6 octahedra around the [111] axis (Cochran and Zia, 1968). The frequency of this soft mode becomes positive when pressure increases as shown by the phonon dispersion at 16 GPa (Figure 3.9), indicating that the $Pm\bar{3}m$ phase becomes stable at high pressures. The squared frequency of

the F_{2u} mode $\omega_F{}^2$ was plotted against pressure and a phase transition pressure of 13.93 GPa was obtained by linear fitting (Figure 3.12), which is close to the 13 GPa of Tohei *et al.* (2005) by a similar method.

The $R\bar{3}c$ phase stable at low pressures is the result of the freezing of the soft F_{2u} mode and this triplet in the $Pm\bar{3}m$ phase splits into an A_{1g} singlet and an E_g doublet in the $R\bar{3}c$ phase (Figure 3.10, Figure 3.11) (Thomas and Müller, 1968). These two Raman active modes are rotations of the AlO_6 octahedra around the hexagonal *c* axis and a perpendicular axis, respectively (e.g. Iliev and Abrashev, 2001). Comparison of the phonon frequencies at Γ point at 0 GPa and 6 GPa of the $R\bar{3}c$ phase reveals the softening of the A_{1g} mode with increasing pressure (Figure 3.10, Figure 3.11). Its frequency squared shows a linear downward trend against pressure before the phase transition at ~14 GPa, except that it curves up approaching 14 GPa and does not go to zero at 14 GPa (Figure 3.12). Our squared frequencies of the A_{1g} mode are greater than the Raman spectroscopy data of Bouvier and Kreisel (2002) but smaller than the DFT calculations of Tohei *et al.* (2005).

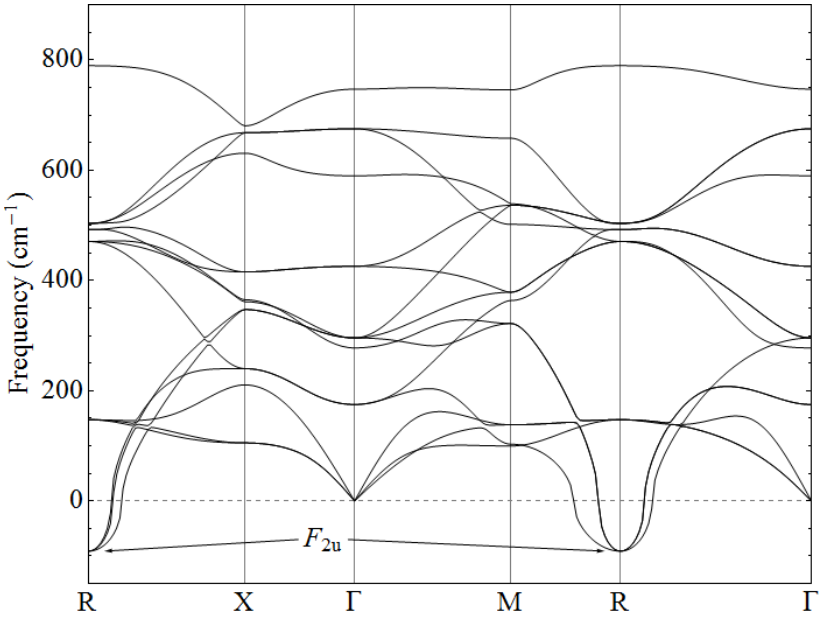

Figure 3.8 Phonon dispersion of $Pm\bar{3}m$ $LaAlO_3$ perovskite at 0 GPa.

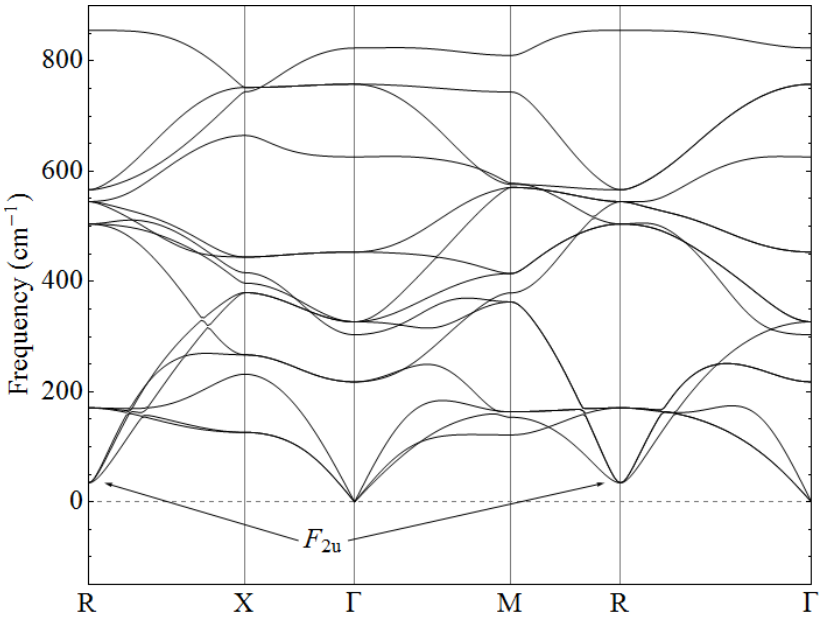

Figure 3.9 Phonon dispersion of $Pm\bar{3}m$ $LaAlO_3$ perovskite at 16 GPa.

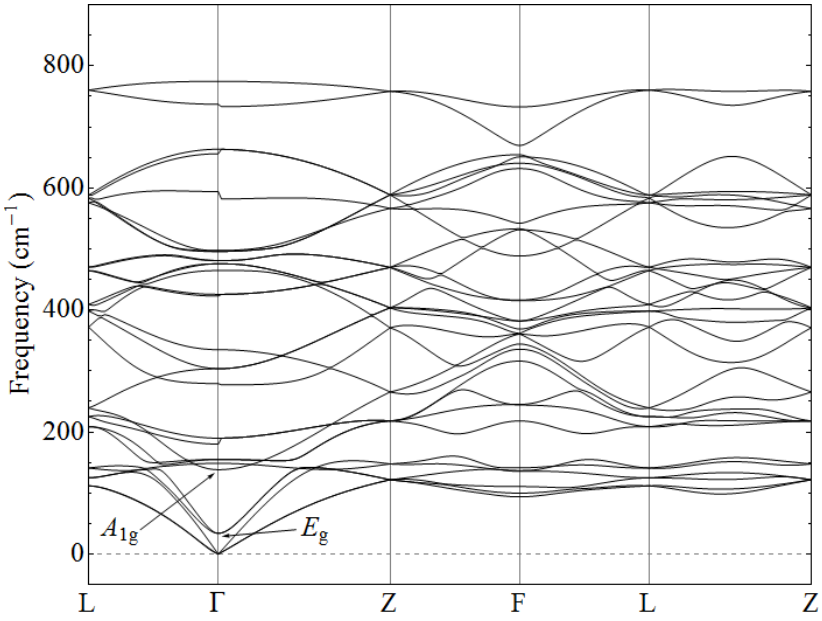

Figure 3.10 Phonon dispersion of $R\bar{3}c$ $LaAlO_3$ perovskite at 0 GPa.

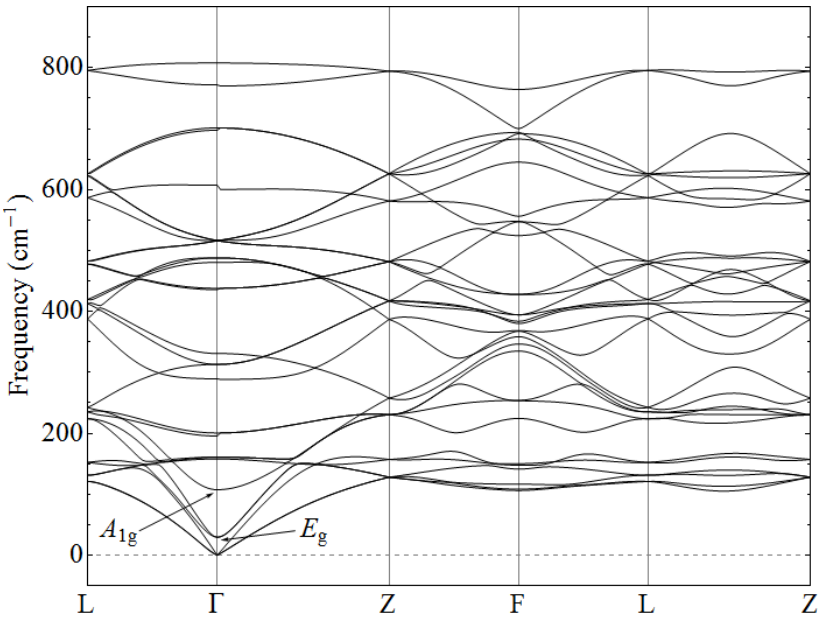

Figure 3.11 Phonon dispersion of $R\bar{3}c$ $LaAlO_3$ perovskite at 6 GPa.

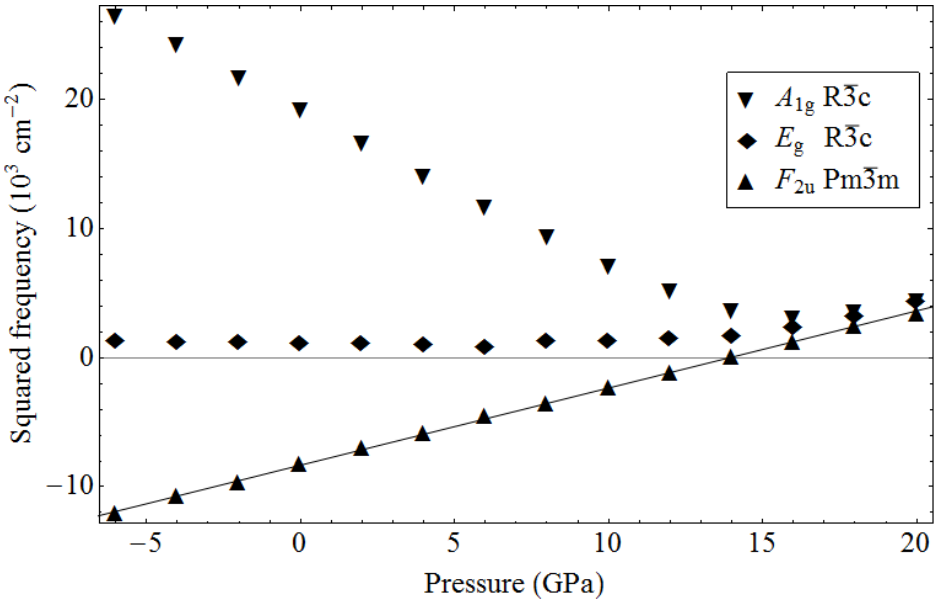

Figure 3.12 Squared frequencies of soft modes of $R\bar{3}c$ and $Pm\bar{3}m$ $LaAlO_3$ perovskites as a function of pressure. The line is linear fitting result.

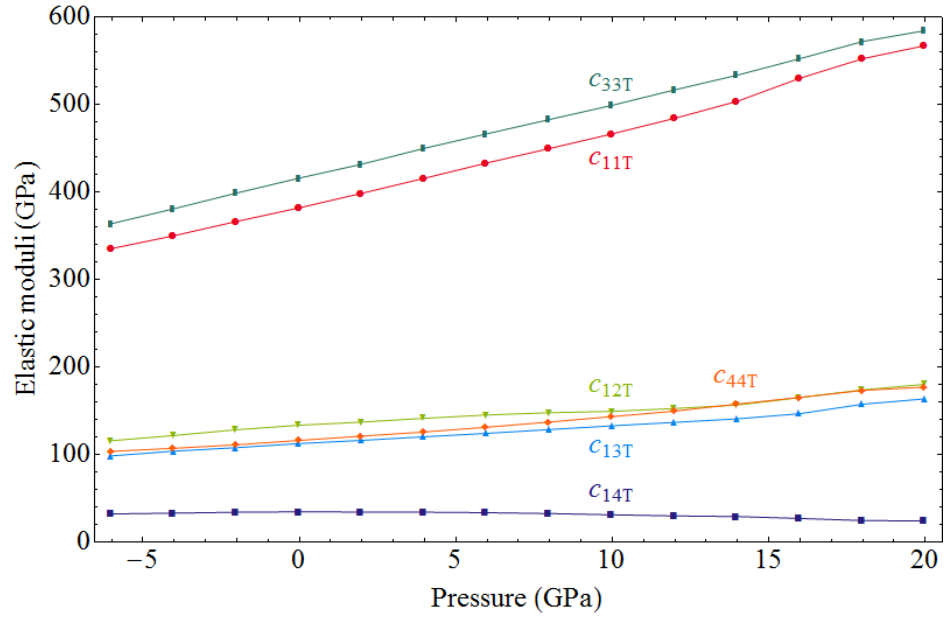

Figure 3.13 Elastic moduli of the $R\bar{3}c$ $LaAlO_3$ perovskite as a function of pressure.

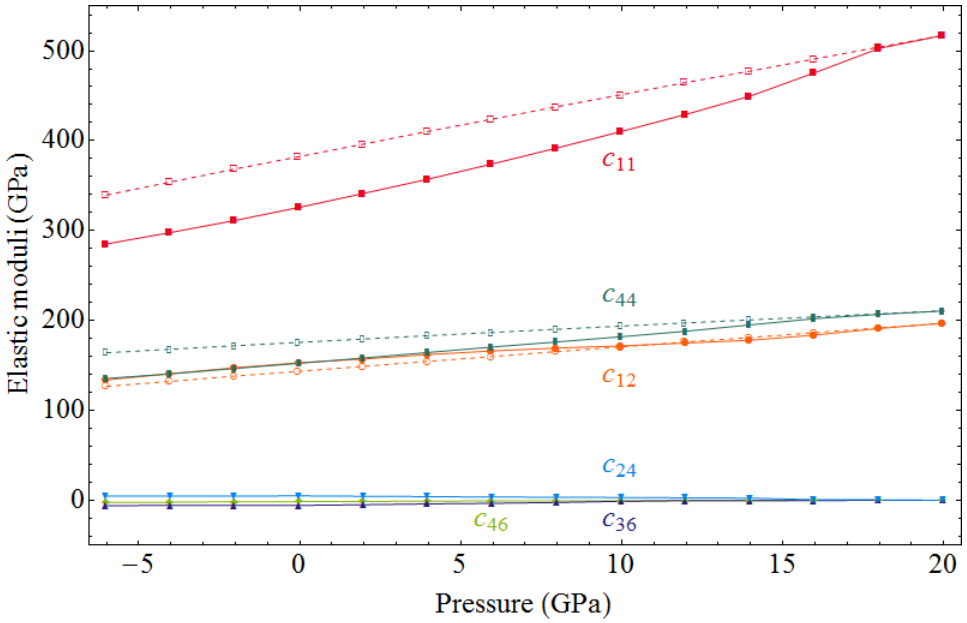

Figure 3.14 Elastic moduli of $R\bar{3}c$ and $Pm\bar{3}m$ $LaAlO_3$ perovskites referred to the cubic reference system. Filled symbols connected with solid lines are for $R\bar{3}c$ structure, open symbols connected with dash lines are for $Pm\bar{3}m$ structure.

3.3.5 Elasticity

The elastic moduli of the $R\bar{3}c$ and $Pm\bar{3}m$ phases were calculated using the linear stress-strain relationship $\sigma_i = c_{ij}\varepsilon_j$ ($i, j = 1 - 6$) (Figure 3.13, Figure 3.14). In order to solve the stiffness coefficients c_{ij} of the $R\bar{3}c$ phase, 42 different strains were applied, which are $\pm\varepsilon_1$, $\pm\varepsilon_2$, $\pm\varepsilon_3$, $\pm(\varepsilon_1 - \varepsilon_2)$, $\pm(\varepsilon_1 - \varepsilon_3)$, $\pm(\varepsilon_2 - \varepsilon_3)$, $\pm\varepsilon_4$, $\pm\varepsilon_5$, $\pm\varepsilon_6$, $\pm(\varepsilon_4 - \varepsilon_5)$, $\pm(\varepsilon_4 - \varepsilon_6)$, $\pm(\varepsilon_5 - \varepsilon_6)$, $\pm(\varepsilon_1 - \varepsilon_4)$, $\pm(\varepsilon_1 - \varepsilon_5)$, $\pm(\varepsilon_1 - \varepsilon_6)$, $\pm(\varepsilon_2 - \varepsilon_4)$, $\pm(\varepsilon_2 - \varepsilon_5)$, $\pm(\varepsilon_2 - \varepsilon_6)$, $\pm(\varepsilon_3 - \varepsilon_4)$, $\pm(\varepsilon_3 - \varepsilon_5)$ and $\pm(\varepsilon_3 - \varepsilon_6)$, where $\varepsilon_1 = \varepsilon_2 = \varepsilon_3 = 0.01$, $\varepsilon_4 = \varepsilon_5 = \varepsilon_6 = 0.02$. The unit cell of the optimized structure at each pressure was strained and the internal atomic positions were relaxed. The resulting 6 stress components σ_i together with the 6 strain components ε_j generate 6 linear equations $\sigma_i = \sum_{j=1}^{6} c_{ij}\varepsilon_j$, $i = 1 - 6$, with respect to the 36 c_{ij}. The 42 different strains applied, therefore, generate $42 \times 6 = 252$ equations. Because the stiffness matrix is symmetric, another 15 equations $c_{ij} - c_{ji} = 0$, $i = 1 - 5$, $j = i+1 - 6$, were raised to impose this symmetric dependency between upper and lower off-diagonal c_{ij}. More dependencies are imposed by the $R\bar{3}c$ symmetry of the system on the fourth rank stiffness tensor and result in 6 independent stiffness coefficients c_{11}, c_{33}, c_{12}, c_{13}, c_{14} and c_{44}. To impose these dependencies, only those between the upper triangular c_{ij} are needed because the symmetric dependency can constrain the lower diagonal c_{ij}. Thus, 15 equations with respect to the upper diagonal c_{ij} were raised, e.g. $c_{11} - c_{22} = 0$, $c_{15} = 0$. As expected, the number of variables, i.e. 36 c_{ij}, minus the number of constraints, i.e. 15 + 15 = 30 equations, equals the number of degrees of freedom, i.e. 6 independent c_{ij}.

To solve the stiffness coefficients of the $Pm\bar{3}m$ phase, 6 different strains were applied, which are $\pm\varepsilon_1$, $\pm(\varepsilon_1 - \varepsilon_2)$ and $\pm\varepsilon_4$. Therefore, the linear stress-strain relationship provides $6 \times 6 = 36$ equations. The diagonal symmetry of the stiffness matrix provides the same 15 equations as in the $R\bar{3}c$ case. The $Pm\bar{3}m$ symmetry of the system reduces the independent stiffness coefficients to c_{11}, c_{12} and c_{44} and provides 18 equations with respect to the upper triangular c_{ij}. Similar to the $R\bar{3}c$ case, the number of independent c_{ij} 3 equals the number of total c_{ij} 36 minus the number of constraints, i.e. 15 + 18 = 33. For $R\bar{3}c$ and $Pm\bar{3}m$ phases, I have respectively 252 + 30 = 282 and 36 + 33 = 69 equations with respect to 36 c_{ij}. The singular value decomposition (SVD)

method (e.g. Parker, 1994) was used to solve the two sets of linear equations. A weight factor was applied to the coefficients of the constraint equations in order to control how strictly the constraints are satisfied.

Table 3.3 Elastic, bulk and shear moduli[a] of $R\bar{3}c$ and $Pm\bar{3}m$ $LaAlO_3$ perovskites at 0 GPa.

	$R\bar{3}c$				$Pm\bar{3}m$				
	This work	Brillouin[b]	LDA[c]	GGA[c]	This work	LDA[d]	GGA[e]	LDA[c]	GGA[c]
c_{11}	382.15	337.2	390.70	381.56	382.40	382	328.20	324.47	313.56
c_{33}	416.24	411.3	411.3	411.17					
c_{12}	133.31	151.5	146.03	100.30	143.60	150	134.76	120.65	134.62
c_{13}	112.38	92.7	69.79	72.54					
c_{14}	34.30	45.7	34.56	29.66					
c_{44}	115.97	120.6	119.84	115.33	175.75		178.167	169.16	175.61
K	210.72	195.5	196.03	185.63	223.20	227[f]	199.24[f]	187.94	199.45
G	121.25	105.3	133.10	134.92	150.53		139.43[f]	137.37	133.67

[a] All bulk and shear moduli are Voigt-Reuss-Hill values based on elastic moduli. [b] Carpenter *et al.* (2010b). [c] Luo and Wang (2008). [d] Lee and Demkov (2007). [e] PW-PP result of Boudali *et al.* (2009). [f] Calculated according to elastic moduli by present authors.

3.4 Landau analysis

3.4.1 Theory

Structural phase transitions can be analyzed using Landau theory, in which the excess free energy can be expressed as a function of pressure, order parameter and strain (e.g. Carpenter *et al.*, 2000). The order parameter for phase transitions between different perovskite structures is composed of octahedral rotations around the three pseudo-cubic axes associated with *M* and *R* points (e.g. Howard and Stokes, 1998; Chapter 2). The $Pm\bar{3}m$ to $R\bar{3}c$ phase transition only involves *R*-point octahedral rotations around the three pseudo-cubic axes $\mathbf{q} = (q_1, q_2, q_3)$, and the strain takes the symmetry-adapted form $\mathbf{e} = (e_a, e_o, e_t, e_4, e_5, e_6)$, where e_4, e_5, e_6 are the shear

strain components in Voigt notation and e_a, e_o, e_t are combinations of the linear strain components e_1, e_2, e_3 (Carpenter *et al.*, 2001; Carpenter, 2007) as

$$e_a = e_1 + e_2 + e_3, \tag{3.3}$$

$$e_o = e_1 - e_2, \tag{3.4}$$

$$e_t = \frac{1}{\sqrt{3}}(2e_3 - e_1 - e_2). \tag{3.5}$$

The expression of the excess free energy is taken from Carpenter *et al.* (2010a) except that pressure has been substituted for temperature:

$$\begin{aligned} G(P,\mathbf{q},\mathbf{e}) = {} & \frac{1}{2}a(P-P_c)\left(q_1^2+q_2^2+q_3^2\right) \\ & + \frac{1}{4}b\left(q_1^2+q_2^2+q_3^2\right)^2 + \frac{1}{4}b'\left(q_1^4+q_2^4+q_3^4\right) \\ & + \lambda_1 e_a\left(q_1^2+q_2^2+q_3^2\right) + \lambda_2\left[\sqrt{3}e_o\left(q_2^2-q_3^2\right) + e_t\left(2q_1^2-q_2^2-q_3^2\right)\right] \\ & + \lambda_3\left(e_4 q_1 q_3 + e_5 q_1 q_2 + e_6 q_2 q_3\right) \\ & + \frac{1}{4}\left(c_{11}^0 - c_{12}^0\right)\left(e_o^2+e_t^2\right) + \frac{1}{6}\left(c_{11}^0 + 2c_{12}^0\right)e_a^2 + \frac{1}{2}c_{44}^0\left(e_4^2+e_5^2+e_6^2\right), \end{aligned} \tag{3.6}$$

where P_c is critical pressure, a, b, b' are normal Landau coefficients, λ_1, λ_2, λ_3 are order parameter/strain coupling coefficients, c_{11}^0, c_{12}^0, c_{44}^0 are bare elastic moduli which are the elastic moduli of the cubic structure.

The equilibrium condition $\partial G/\partial e_i = 0$ yields the relationship between spontaneous strain and order parameter $\mathbf{e}(\mathbf{q})$ which, after $q_1 = q_2 = q_3$ is applied for the $R\bar{3}c$ structure, becomes $\mathbf{e}(q_1)$ as

$$e_a = -\frac{\lambda_1\left(q_1^2+q_2^2+q_3^2\right)}{\frac{1}{3}\left(c_{11}^0+2c_{12}^0\right)} = -\frac{3\lambda_1 q_1^2}{\frac{1}{3}\left(c_{11}^0+2c_{12}^0\right)}, \tag{3.7}$$

$$e_o = -\frac{\lambda_2\sqrt{3}\left(q_2^2-q_3^2\right)}{\frac{1}{2}\left(c_{11}^0-c_{12}^0\right)} = 0, \tag{3.8}$$

$$e_{\mathrm{t}} = \frac{\lambda_2\left(2q_1^2 - q_2^2 - q_3^2\right)}{\frac{1}{2}\left(c_{11}^0 - c_{12}^0\right)} = 0, \tag{3.9}$$

$$e_4 = -\frac{\lambda_3 q_1 q_3}{c_{44}^0} = -\frac{\lambda_3 q_1^2}{c_{44}^0}, \tag{3.10}$$

$$e_5 = -\frac{\lambda_3 q_1 q_2}{c_{44}^0} = -\frac{\lambda_3 q_1^2}{c_{44}^0}, \tag{3.11}$$

$$e_6 = -\frac{\lambda_3 q_2 q_3}{c_{44}^0} = -\frac{\lambda_3 q_1^2}{c_{44}^0}. \tag{3.12}$$

The above six equations are the same as those of Carpenter *et al.* (2010a) although pressure has been substituted for temperature in the excess free energy expression. Substituting Equations (3.7) – (3.12) into (3.6) and applying $q_1 = q_2 = q_3$ give

$$G\left(P, q_1, \mathbf{e}\left(q_1\right)\right) = \frac{3}{2}a\left(P - P_{\mathrm{c}}\right)q_1^2 + \frac{3}{4}\left(3b + b' - \frac{6\lambda_1^2}{\frac{1}{3}\left(c_{11}^0 + 2c_{12}^0\right)} - \frac{2\lambda_3^2}{c_{44}^0}\right)q_1^4. \tag{3.13}$$

Taking ${q_1}^2$ as a single variable and applying the equilibrium condition $\partial G/\partial({q_1}^2) = 0$ to Equation (3.13) yields the relationship between order parameter and pressure as

$$\left(q_1\left(P\right)\right)^2 = -\frac{a\left(P - P_{\mathrm{c}}\right)}{3b + b' - \frac{6\lambda_1^2}{\frac{1}{3}\left(c_{11}^0 + 2c_{12}^0\right)} - \frac{2\lambda_3^2}{c_{44}^0}}. \tag{3.14}$$

Rearranging the above $q_1(P)$ to the $P(q_1)$ form and substituting it to Equation (3.13) give the relationship between excess free energy and order parameter as

$$G\left(P\left(q_1\right), q_1, \mathbf{e}\left(q_1\right)\right) = -\frac{3}{4}\left(3b + b' - \frac{6\lambda_1^2}{\frac{1}{3}\left(c_{11}^0 + 2c_{12}^0\right)} - \frac{2\lambda_3^2}{c_{44}^0}\right)q_1^4. \tag{3.15}$$

The squared frequencies of A_{1g} singlet and E_g doublet modes $\omega_A{}^2$ and $\omega_E{}^2$ are proportional to the eigenvalues of the susceptibility matrix $\partial G/\partial q_i \partial q_j$ ($i, j = 1, 2, 3$) (Slonczewski and Thomas, 1970). To calculate $\partial G/\partial q_i \partial q_j$, the $G(P,\mathbf{q},\mathbf{e})$ expression (Equation (3.6)) was subject to the partial differentiation and then the relationships $P(q_1)$, $q_1 = q_2 = q_3$, and $\mathbf{e}(q_1)$ (Equations (3.7) – (3.12)) were applied. The results were the same as those of Carpenter *et al.* (2010a) although pressure rather than temperature is involved here, thus the $\omega_E{}^2/\omega_A{}^2$ expression as the ratio of the eigenvalues was cited from Carpenter *et al.* (2010a) as

$$\frac{\omega_E^2}{\omega_A^2} = \frac{2b' + \dfrac{3\lambda_3^2}{c_{44}^0}}{2\left(3b + b'\right)}. \tag{3.16}$$

The elastic moduli of the lower symmetry structure can be related to the bare elastic moduli (Slonczewski and Thomas, 1970) by

$$c_{ij} = c_{ij}^0 - \sum_{kl} \frac{\partial^2 G}{\partial e_i \partial q_k} R_{kl} \frac{\partial^2 G}{\partial q_l \partial e_j} \tag{3.17}$$

where c_{ij} and c_{ij}^0 are referred to the cubic reference system, R_{kl} are the components of the inverse matrix of the susceptibility matrix. To calculate $\partial G/\partial e_i \partial q_k$ or $\partial G/\partial q_l \partial e_j$, symmetry-adapted strain expressions (Equations (3.3) – (3.5)) were first substituted into the $G(P,\mathbf{q},\mathbf{e})$ expression (Equation (3.6)) and after partial differentiation $q_1 = q_2 = q_3$ was applied. Again, the c_{ij} results are the same as those of Carpenter *et al.* (2010a), in spite that rather than their intermediate formula, the final formula are given here as

$$c_{11} = c_{11}^0 - \left(\frac{6\lambda_1^2}{3b + b'} + \frac{32\lambda_2^2}{2b' + \dfrac{3\lambda_3^2}{c_{44}^0}} \right), c_{12} = c_{12}^0 - \left(\frac{6\lambda_1^2}{3b + b'} - \frac{16\lambda_2^2}{2b' + \dfrac{3\lambda_3^2}{c_{44}^0}} \right), \tag{3.18}$$

$$c_{44} = c_{44}^0 - \left(\frac{\frac{2}{3}\lambda_3^2}{3b + b'} + \frac{\frac{2}{3}\lambda_3^2}{2b' + \dfrac{3\lambda_3^2}{c_{44}^0}} \right), c_{46} = -\left(\frac{\frac{2}{3}\lambda_3^2}{3b + b'} - \frac{\frac{1}{3}\lambda_3^2}{2b' + \dfrac{3\lambda_3^2}{c_{44}^0}} \right), \tag{3.19}$$

$$c_{36} = -\left(\frac{2\lambda_1\lambda_3}{3b+b'} - \frac{\frac{8}{\sqrt{3}}\lambda_2\lambda_3}{2b' + \frac{3\lambda_3^2}{c_{44}^0}} \right), c_{24} = -\left(\frac{2\lambda_1\lambda_3}{3b+b'} + \frac{\frac{4}{\sqrt{3}}\lambda_2\lambda_3}{2b' + \frac{3\lambda_3^2}{c_{44}^0}} \right). \quad (3.20)$$

3.4.2 Calibration of Landau coefficients

The order parameter/strain coupling coefficients λ_1 and λ_3 can be determined by fitting the $\mathbf{e}(q_1)$ equations involving spontaneous strain and order parameter to the calculated data. The spontaneous symmetry-adapted strains e_a and e_4 can be evaluated (Carpenter *et al.*, 2005) by

$$e_a = 3\left(\frac{a_{pc}}{a_0} - 1 \right), \quad (3.21)$$

$$e_4 = \frac{a_{pc}}{a_0}\cos\alpha_{pc}, \quad (3.22)$$

where a_{pc} and α_{pc} are the pseudo-cubic cell parameters of the rhombohedral structure, a_0 is the cell parameter of the cubic structure. In the high-temperature experimental study of $LaAlO_3$ by Hayward *et al.* (2005), a_0 at low temperatures in the rhombohedral stability field were extrapolated from the high-temperature data measured in the cubic stability field. In this study, I have optimized the cubic structures at low pressures and the cubic cell parameters so obtained were used as a_0. Similarly, the elastic moduli calculated for the cubic structures at low pressures (Figure 3.14) were used as bare elastic moduli c_{11}^0, c_{12}^0, c_{44}^0 and it is not needed to assume the bare elastic moduli to be constant or linearly dependent on pressure. The value of the order parameter for pressure-induced phase transition has previously been defined arbitrarily (Carpenter *et al.*, 2000). In this study, I use the rotation angle in degrees of the AlO_6 octahedra around either of the three pseudo-cubic axes, i.e. angle φ in Figure 3.4, as the value of q_1 to give the order parameter a structural meaning.

The phase transition pressure 13.93 GPa has been obtained by linear fitting of the squared frequency of cubic F_{2u} mode. To simplify the fitting procedure below, a critical pressure P_c = 14 GPa was assumed and data calculated at −6 – 14 GPa were considered in the fits. The $e_a(q_1)$ and

$e_4(q_1)$ equations (3.7), (3.10)were used to fit the calculated e_a , e_4, q_1 and c_{11}^0, c_{12}^0, c_{44}^0 to determine λ_1 and λ_3 respectively (Figure 3.15, Figure 3.16). As pressure drops from 14 GPa, e_a , e_4 and q_1 all depart from zero. If c_{11}^0, c_{12}^0, c_{44}^0 are constant with respect to pressure, e_a and e_4 should be proportional to ${q_1}^2$ according to the $e_a(q_1)$ and $e_4(q_1)$ equations (3.7), (3.10). However, c_{11}^0, c_{12}^0, c_{44}^0 actually decrease as pressure drops (Figure 3.14), and therefore cause e_a to curve up and e_4 to curve down with increasing ${q_1}^2$ as suggested by the fitted lines in Figure 3.15 and Figure 3.16 respectively. While the calculated e_a follow the fitted line well, e_4 show an opposite curvature with respect to the fit. The reason is not clear. Note that e_a , e_4 and q_1 should all be zero at 14 GPa, but none of them are, although close to, zero in our calculations. Thus I disregarded four data points at 8 – 14 GPa during the fitting. Also, the ${\omega_E}^2/{\omega_A}^2$ results at these four pressures are unreasonably high (see below). The fitting results are $\lambda_1 = -2.817\times10^{-2}$ GPa, $\lambda_3 = 3.574\times10^{-2}$ GPa.

The $G(q_1)$ equation (3.15) can be used to determine the coefficient combination $3b + b'$ given that the values of λ_1 and λ_3 are known. Static calculation means $T = 0$ K, thus the excess free energy equals the enthalpy difference between the two phases in Figure 3.17 with an opposite sign. Due to different k-point samplings for the two structures as discussed earlier, the enthalpy difference is not zero at 14 GPa where it should be, therefore the enthalpy differences at all pressures were shifted downward uniformly by its amount at 14 GPa so that it becomes zero at 14 GPa. The unit of G in relevant equations is GPa, i.e. the excess free energy per unit volume, thus the enthalpy difference was divided by the volume per formula unit of the cubic phase at 14 GPa. The G increases with ${q_1}^2$ approximately quadratically, except that c_{11}^0, c_{12}^0, c_{44}^0 are not constant (Figure 3.17). The four data points at 8 – 14 GPa were disregarded during the fitting for the same reason as $e_a(q_1)$ and $e_4(q_1)$ fits and $3b + b' = 4.396\times10^{-4}$ GPa was obtained.

The coefficient a was determined from the fit of $q_1(P)$ equation (3.14), given the values of λ_1, λ_3 and $3b + b'$ (Figure 3.18). The dependency of ${q_1}^2$ on pressure is close to linear. The a is dimensionless and its value is $a = 2.574\times10^{-4}$. The ${\omega_E}^2/{\omega_A}^2$ equation (3.16) has coefficients b and b' and was combined with the $3b + b'$ value to obtain the individual values of b and b' (Figure 3.19). Because ${\omega_E}^2$ begins to increase above 6 GPa while ${\omega_A}^2$ is still decreasing below 14 GPa

(Figure 3.12), their ratio ω_E^2/ω_A^2 begins to increase dramatically above 6 GPa, which is inconsistent with the Landau expectation (Figure 3.19). It is hard to explain this inconsistency since there were no other experimental or theoretical data of ω_E in this pressure range for comparison. The four data points at 8 – 14 GPa, thereby, were not considered in the fitting and b' = 1.572×10^{-5} GPa was first obtained. Then b = 1.413×10^{-4} GPa was obtained according to the $3b + b'$ value. All the Landau coefficients fitted are summarized in Table 3.4.

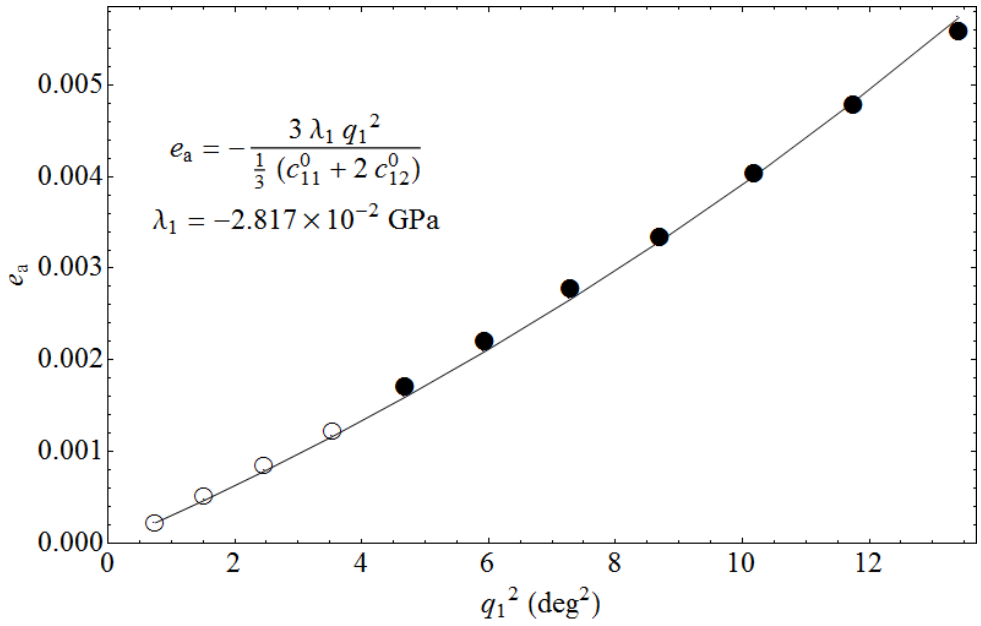

Figure 3.15 Fit of the $e_a(q_1)$ (Equation (3.7)) equation to the calculated data. Circles are calculated data, of which filled ones were used in the fitting, open ones were not. The line is the fitting result.

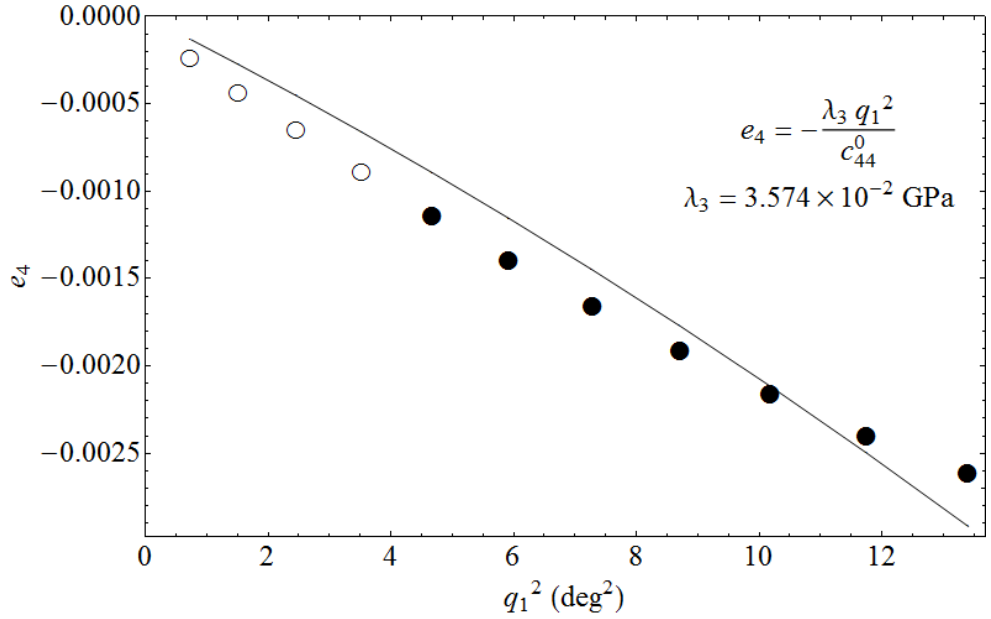

Figure 3.16 Fit of $e_4(q_1)$ (Equation (3.10)) to the calculated data. See the caption of Figure 3.15 for the meaning of notations.

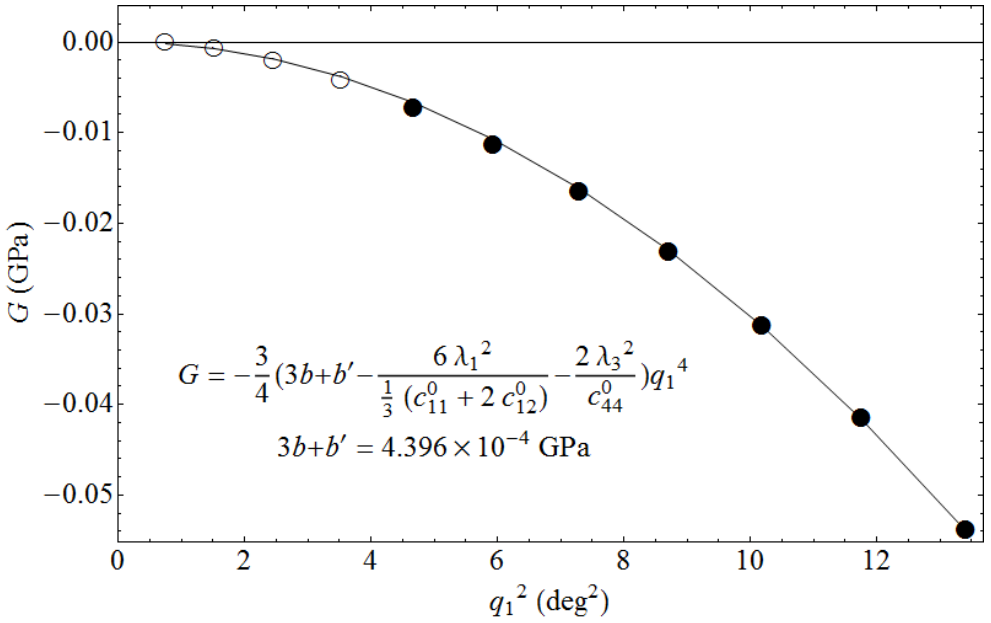

Figure 3.17 Fit of $G(q_1)$ (Equation (3.15)) to the calculated data. See the caption of Figure 3.15 for the meaning of notations.

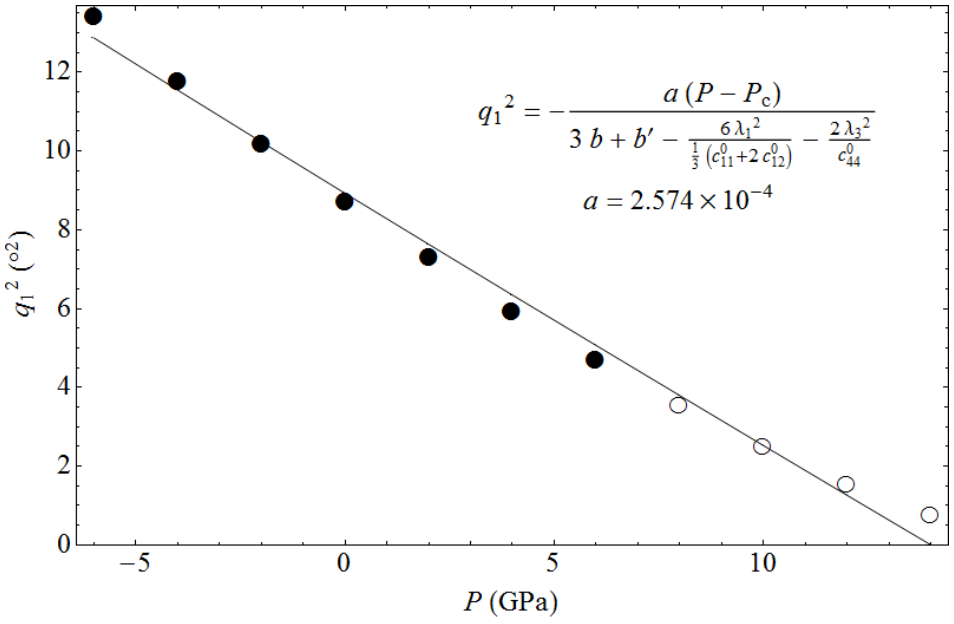

Figure 3.18 Fit of $q_1(P)$ (Equation (3.14)) to the calculated data. See the caption of Figure 3.15 for the meaning of notations.

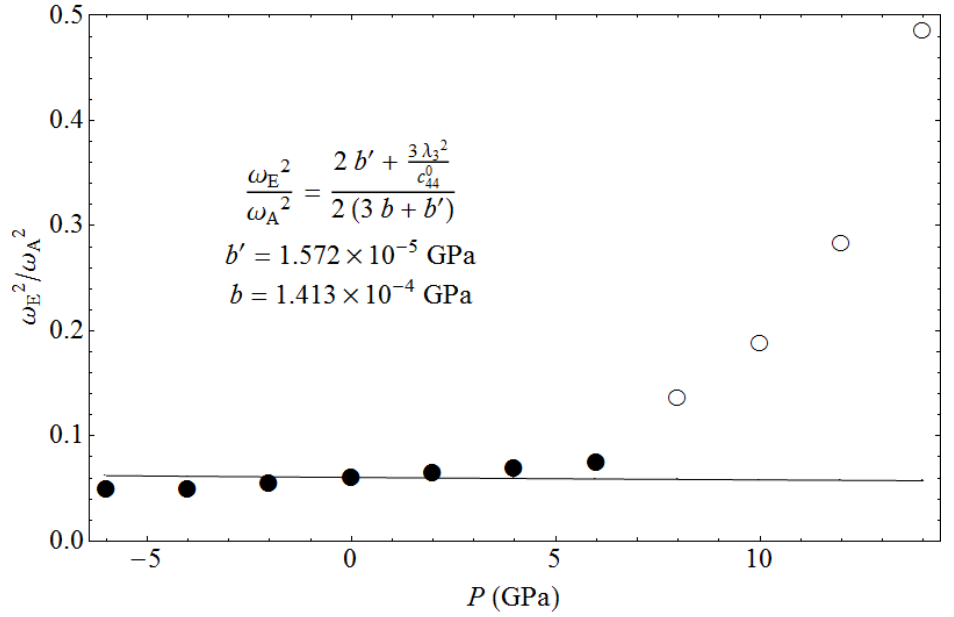

Figure 3.19 Fit of ω_E^2/ω_A^2 (Equation (3.16)) to the calculated data. See the caption of Figure 3.15 for the meaning of notations.

Table 3.4 Values of the Landau coefficients determined by fitting derived equations to calculated spontaneous strain, order parameter, excess free energy and bare elastic moduli at a range of pressures. Values of P_c and λ_2 are assumed.

$a = 2.574\times10^{-4}$
$b = 1.413\times10^{-4}$ GPa
$b' = 1.572\times10^{-5}$ GPa
$\lambda_1 = -2.817\times10^{-2}$ GPa
$\lambda_2 = -6.3\times10^{-3}$ GPa
$\lambda_3 = 3.574\times10^{-2}$ GPa
$P_c = 14$ GPa

3.4.3 Testing

The validity of the fitted Landau coefficients can be tested by comparing the Landau expected elastic moduli given by Equations (3.18) – (3.20) and the calculated elastic moduli. These equations give the Landau expectations for $c_{ij}^0 - c_{ij}$, i.e. the expressions in the parenthesis in terms of Landau coefficients and c_{44}^0. The fitted Landau coefficients and the calculated c_{44}^0 provide the Landau expected $c_{ij}^0 - c_{ij}$, and comparing them with the calculated values can test the whole fitting procedure. The only Landau coefficient which has not been determined is λ_2. Although λ_2 appears in the $e_o(\mathbf{q})$ and $e_t(\mathbf{q})$ equations ((3.8), (3.9)), the two strains vanish spontaneously and make the fits unavailable. An estimated value $\lambda_2 = -6.3\times10^{-3}$ GPa was used.

Figure 3.20 shows that as pressure approaches 14 GPa, the calculated $c_{ij}^0 - c_{ij}$ values tend to approach zero, while the Landau expected values depart from zero slightly due to the increasing c_{44}^0 in Equations (3.18) – (3.20). Because the phase transition occurs at a relatively low pressure, calculations far below the transition pressure were not performed, but they are needed to see if the calculated values follow the Landau expected departing trend far below the transition pressure. Of the six independent c_{ij}, c_{11}, c_{12}, c_{44} have larger absolute values of $c_{ij}^0 - c_{ij}$ than

expected from the Landau theory, while c_{46}, c_{36}, c_{24} have smaller absolute values of $c_{ij}^{0} - c_{ij}$ than expected. The differences between the calculated and Landau expected $c_{ij}^{0} - c_{ij}$ are around 10 GPa for all the c_{ij}, except that it can be as large as 20 GPa for c_{11}, which, by itself, is much larger than the other c_{ij}.

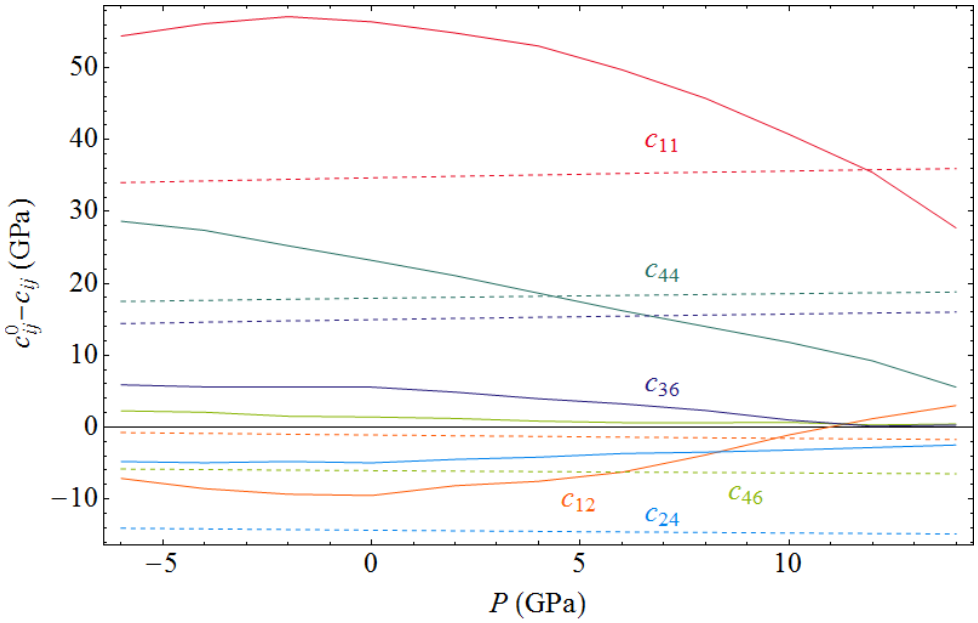

Figure 3.20 Comparison of the calculated (solid) and Landau expected (dash) $c_{ij}^{0} - c_{ij}$.

3.5 Conclusion

The pressure-induced $R\bar{3}c$ to $Pm\bar{3}m$ phase transition of $LaAlO_3$ perovskite was reproduced theoretically using PW-PP method and LDA in the DFT framework. Linear fitting of ω_F^2 with pressure gave transition pressure of ~14 GPa, which is close to experimental results. Softening of the A_{1g} mode of the $R\bar{3}c$ phase was also found. Elastic moduli of the two structures were calculated using stress-strain relationship and SVD inversion. The Landau expression of excess free energy for this phase transition was used to derive subsequent equations, which were fitted to the calculated data to obtain the Landau coefficients. The cell parameter and elastic moduli of the cubic structure were provided by the calculations and no approximations were needed as in

experimental studies. The fitted Landau coefficients were tested by comparing the calculated and Landau expected elastic moduli and the result is reasonably good.

3.6 References

Baroni S, de Gironcoli S, Dal Corso A and Giannozzi P 2001 Phonons and related crystal properties from density-functional perturbation theory *Rev. Mod. Phys.* **73** 515-62

Boudali A, Amrani B, Driss khodja M, Abada A and Amara K 2009 First-principles study of structural, elastic, electronic, and thermal properties of $LaAlO_3$ perovskite *Comp. Mater. Sci.* **45** 1068-72

Bouvier P and Kreisel J 2002 Pressure-induced phase transition in $LaAlO_3$ *J. Phys.: Condens. Matter* **14** 3981-91

Bueble S, Knorr K, Brecht E and Schmahl W W 1998 Influence of the ferroelastic twin domain structure on the {100} surface morphology of $LaAlO_3$ HTSC substrates *Surf. Sci.* **400** 345-55

Carpenter M A 2007 Elastic anomalies accompanying phase transitions in (Ca,Sr)TiO_3 perovskites: Part I. Landau theory and a calibration for $SrTiO_3$ *Am. Miner.* **92** 309-27

Carpenter M A, Becerro A I and Seifert F 2001 Strain analysis of phase transitions in (Ca,Sr)TiO_3 perovskites *Am. Miner.* **86** 348-63

Carpenter M A, Hemley R J and Mao H K 2000 High-pressure elasticity of stishovite and the $P4_2/mnm$ reversible arrow Pnnm phase transition *J. Geophys. Res. Solid Earth* **105** 10807-16

Carpenter M A, Howard C J, Kennedy B J and Knight K S 2005 Strain mechanism for order-parameter coupling through successive phase transitions in $PrAlO_3$ *Phys. Rev. B* **72** 024118

Carpenter M A, Sinogeikin S V and Bass J D 2010a Elastic relaxations associated with the Pm-3m - R-3c transition in $LaAlO_3$: II. Mechanisms of static and dynamical softening *J. Phys.: Condens. Matter* **22**

Carpenter M A, Sinogeikin S V, Bass J D, Lakshtanov D L and Jacobsen S D 2010b Elastic relaxations associated with the Pm-3m – R-3c transition in LaAlO3 : I. Single crystal elastic moduli at room temperature *J. Phys.: Condens. Matter* **22** 035403

Ceperley D M and Alder B J 1980 Ground State of the Electron Gas by a Stochastic Method *Phys. Rev. Lett.* **45** 566-9

Cochran W and Zia A 1968 Structure and dynamics of perovskite-type crystals *phys. status solidi b* **25** 273-83

Giannozzi P, Baroni S, Bonini N, Calandra M, Car R, Cavazzoni C, Ceresoli D, Chiarotti G L, Cococcioni M, Dabo I, Corso A D, Gironcoli S d, Fabris S, Fratesi G, Gebauer R, Gerstmann U, Gougoussis C, Kokalj A, Lazzeri M, Martin-Samos L, Marzari N, Mauri F, Mazzarello R, Paolini S, Pasquarello A, Paulatto L, Sbraccia C, Scandolo S, Sclauzero G, Seitsonen A P, Smogunov A, Umari P and Wentzcovitch R M 2009 QUANTUM ESPRESSO: a modular and open-source software project for quantum simulations of materials *J. Phys.: Condens. Matter* **21** 395502

Glazer A M 1972 The classification of tilted octahedra in perovskites *Acta Cryst.* **B28** 3384-92

Guennou M, Bouvier P, Garbarino G and Kreisel J 2011 Structural investigation of $LaAlO_3$ up to 63 GPa *J. Phys.: Condens. Matter* **23** 395401

Hayward S A, Morrison F D, Redfern S A T, Salje E K H, Scott J F, Knight K S, Tarantino S, Glazer A M, Shuvaeva V, Daniel P, Zhang M and Carpenter M A 2005 Transformation processes in $LaAlO_3$: Neutron diffraction, dielectric, thermal, optical, and Raman studies *Phys. Rev. B* **72**

Hohenberg P and Kohn W 1964 Inhomogeneous Electron Gas *Phys. Rev.* **136** B864-B71

Howard C J, Kennedy B J and Chakoumakos B C 2000 Neutron powder diffraction study of rhombohedral rare-earth aluminates and the rhombohedral to cubic phase transition *J. Phys.: Condens. Matter* **12** 349

Howard C J and Stokes H T 1998 Group-Theoretical Analysis of Octahedral Tilting in Perovskites *Acta Cryst.* **B54** 782-9
Iliev M N and Abrashev M V 2001 Raman phonons and Raman Jahn–Teller bands in perovskite-like manganites *J. Raman Spectrosc.* **32** 805-11
Kleinman L and Bylander D M 1982 Efficacious Form for Model Pseudopotentials *Phys. Rev. Lett.* **48** 1425-8
Lee J and Demkov A A 2007 *Theoretical Investigation of the Band Alignment at the $LaAlO_3/SrTiO_3$ Interface, in Ferroelectric and Multferroics, MRS Symposia Proceedings No. 966,* ed J-P M V. Gopalan, M. Fiebig, C.-W. Nan (Warrendale, PA: Materials Research Society) pp 0966-T07-33
Luo X and Wang B 2008 Structural and elastic properties of $LaAlO_3$ from first-principles calculations *J. Appl. Phys.* **104** 073518-7
Monkhorst H J and Pack J D 1976 Special points for Brillouin-zone integrations *Phys. Rev. B* **13** 5188-92
Parker R L 1994 *Geophysical Inverse Theory* (Princeton: Princeton University Press)
Perdew J P and Zunger A 1981 Self-interaction correction to density-functional approximations for many-electron systems *Phys. Rev. B* **23** 5048-79
Slonczewski J C and Thomas H 1970 Interaction of Elastic Strain with the Structural Transition of Strontium Titanate *Phys. Rev. B* **1** 3599-608
Taspinar E and Cuneyt Tas A 1997 Low-Temperature Chemical Synthesis of Lanthanum Monoaluminate *J. Am. Ceram. Soc.* **80** 133-41
Thomas H and Müller K A 1968 Structural Phase Transitions in Perovskite-Type Crystals *Phys. Rev. Lett.* **21** 1256-9
Tohei T, Kuwabara A, Yamamoto T, Oba F and Tanaka I 2005 General Rule for Displacive Phase Transitions in Perovskite Compounds Revisited by First Principles Calculations *Phys. Rev. Lett.* **94** 035502
Troullier N and Martins J L 1991 Efficient pseudopotentials for plane-wave calculations *Phys. Rev. B* **43** 1993-2006
Vali R 2008 Phonons and heat capacity of $LaAlO_3$ *Comp. Mater. Sci.* **44** 779-82
Wentzcovitch R M 1991 Invariant molecular-dynamics approach to structural phase transitions *Phys. Rev. B* **44** 2358-61
Zhao J, Ross N L and Angel R J 2004 Polyhedral control of the rhombohedral to cubic phase transition in $LaAlO_3$ perovskite *J. Phys.: Condens. Matter* **16** 8763-73

Chapter 4: Phase transition and elasticity of $YAlO_3$ perovskite at high pressures: a first-principles study

4.1 Abstract

First-principles plane-wave pseudopotential calculations were used to investigate the high-pressure phase transitions and elasticity of $YAlO_3$ perovskite. The *Pnma*, *Imma*, *I*4/*mcm*, $R\bar{3}c$, $Pm\bar{3}m$ perovskite structures and the NH_4CdCl_3-, Gd_2S_3-, U_2S_3-, $CaIrO_3$-type structures are considered. The pressure variation of the soft *Z*-point mode of the *Imma* structure clearly shows a second-order *Pnma* to *Imma* phase transition occurring at ~89 GPa, which is followed by a first-order *Imma* to *I*4/*mcm* transition occurring at ~100 GPa, as suggested by the relative enthalpies and phonon dispersions. The pressure ranges of mechanical stability of the perovskite structures from the elastic moduli enclose those of dynamical stability from the phonon dispersions, and so are compatible with the phase transitions. The Gd_2S_3- and U_2S_3-type structures evolve to the dynamically stable NH_4CdCl_3- and $CaIrO_3$-types respectively during the structural relaxations, with the coordination numbers of the Al sites reduced from 7 to 6, suggesting that the latter two structures with smaller octahedral Al sites are preferred by $YAlO_3$, although they are less energetically favorable than the perovskite structures. The energetic mechanism of the high-pressure phase transitions of $YAlO_3$ might be drawn from the qualitatively similarity between the relative *A*/*B* site polyhedral volume ratios and the relative enthalpies of different structures.

4.2 Introduction

$YAlO_3$ perovskite has orthorhombic *Pnma* structure at room conditions the same as $MgSiO_3$ perovskite in the lower mantle (e.g. Diehl and Brandt, 1975). The structure is distorted from the cubic $Pm\bar{3}m$ aristotype by $a^+b^-b^-$ tilting, which means in-phase tilting along one cubic axis and out-of-phase tiltings along the other two cubic axes with equal amplitude (Glazer, 1972; Chapter 2). X-ray diffraction measurements up to 8.5 GPa showed that the structure becomes less distorted with increasing pressure (Ross *et al.*, 2004). First-principles calculations up to more than 100 GPa predicted a *Pnma* – *I*4/*mcm* phase transition at 80 GPa (Wu *et al.*, 2006). The

elastic moduli of the $YAlO_3$ perovskite were obtained also by first-principles calculations (Huang *et al.*, 2011).

So far, only the theoretically predicted results are available as for the high-pressure phase transition and the elasticity of the $YAlO_3$ perovskite. Thus, further independent calculations are needed to test these results. In the previous study (Wu *et al.*, 2006) of the phase transition, the common perovskite structures *Imma* and $R\bar{3}c$ were not considered. The former is an intermediate phase in the high-temperature $Pnma - Imma - I4/mcm - Pm\bar{3}m$ transition series of $SrZrO_3$, $SrRuO_3$, $SrRhO_3$, $SrSnO_3$ and $SrTcO_3$ perovskites (Howard *et al.*, 2000; Kennedy *et al.*, 2002; Kennedy *et al.*, 2004; Mountstevens *et al.*, 2005; Thorogood *et al.*, 2011), while the latter is the structure of $LaAlO_3$, $PrAlO_3$ and many other perovskites (e.g. Zhao *et al.*, 2004b; Zhao *et al.*, 2009). Moreover, apart from the *Pnma* perovskite structure, NH_4CdCl_3-, Gd_2S_3-, U_2S_3- and $CaIrO_3$-type (post-perovskite, PPV) structures are often also considered as potential high pressure phases for sesquioxides such as Ga_2O_3, In_2O_3 and Al_2O_3 (Tsuchiya *et al.*, 2007; Yusa *et al.*, 2008; Umemoto and Wentzcovitch, 2008). They can also be considered as candidates for the high-pressure phases of $YAlO_3$. Elasticity and phonons provide information regarding the mechanical and dynamical stabilities respectively, thus calculating them under high pressures helps to determine the stable high-pressure phases. Phonons may also provide insight into the dynamical reasons for the phase transitions.

4.3 Methods

4.3.1 Computational details

First-principles static calculations were performed using the plane-wave pseudopotential (PW-PP) method based on the density functional theory (DFT) (Hohenberg and Kohn, 1964) implemented in the Quantum ESPRESSO suite (Giannozzi *et al.*, 2009). I used the local density approximation (LDA) with the exchange-correlation functional of Ceperley and Alder (1980) as parameterized by Perdew and Zunger (1981).

The norm-conserving pseudopotentials were generated for Y, Al and O atoms using the Troullier-Martins method (Troullier and Martins, 1991) implemented in the ATOMIC code included in the Quantum ESPRESSO suite (Giannozzi *et al.*, 2009). The valence electron configurations used for Y, Al and O are $4s^2 4p^6 4d^1 5s^2 5p^0$, $3s^2 3p^1 3d^0$ and $2s^2 2p^4 3d^0$ respectively, and the cutoff radii for each orbital in Bohr unit are 1.2, 1.4, 1.4, 1.2, 1.4 for Y, 1.6, 1.6, 1.6 for Al, and 1.2, 1.3, 1.4 for O, in the same order of their valence electrons. The *d* potentials were used as the local potentials of Y, Al and O (Kleinman and Bylander, 1982). Bound and unbound states were used for the angular momenta *s*, *p* of Y, Al and O to improve the transferability of the pseudopotentials.

For the *Imma*, *I*4/*mcm*, $R\bar{3}c$ and PPV structures, primitive unit cells with 10 atoms were used in the calculations. The Brillouin zones of the *Pnma*, NH_4CdCl_3-, Gd_2S_3- and U_2S_3-type structures, which have 20 atoms per primitive cell, were sampled on 4×4×2, 4×4×2, 4×4×2 and 2×8×2 special k-point grids (Monkhorst and Pack, 1976) respectively with half-step shifts in three directions. A 4×4×4 grid with shifts in three directions was used for the *Imma*, *I*4/*mcm*, $R\bar{3}c$, $Pm\bar{3}m$ and PPV structures, which have 10 atoms per primitive cell except that $Pm\bar{3}m$ has 5. The kinetic energy cutoff for plane waves was chosen to be 100 Ry.

Variable cell shape molecular dynamics (Wentzcovitch, 1991) was used in the structural relaxations of $YAlO_3$ polymorphs between −20 and 300 GPa at 20 GPa intervals. The phonons of the optimized structures were calculated using density functional perturbation theory (Baroni *et al.*, 2001). The dynamical matrices of the *Pnma* and NH_4CdCl_3-type structures were calculated on a 2×2×2 q-point grid without shifts, while a 4×4×4 grid without shifts was used for the *Imma*, *I*4/*mcm*, $R\bar{3}c$, $Pm\bar{3}m$ and PPV structures which have higher symmetries.

4.3.2 Elasticity

The elastic moduli of the five perovskite structures *Pnma*, *Imma*, *I*4/*mcm*, $R\bar{3}c$ and $Pm\bar{3}m$ were calculated using the linear stress-strain relationship

$$\sigma_i = \sum_{j=1}^{6} c_{ij}\varepsilon_j, (i = 1,...,6). \quad (4.1)$$

If I apply a strain with components ε_j, (j = 1,…,6) to the unit cell of the optimized structure at one pressure and relax the internal atomic positions, the stress σ_i, (i = 1,…,6) under the strain can be so obtained from the first-principles calculations. The ε_j and σ_i pairs generate 6 equations of the form of (4.1) with respect to the 36 stiffness coefficients c_{ij}. Applying a different strain can bring another 6 such equations and so on. The *Pnma*, *Imma*, *I*4/*mcm*, $R\bar{3}c$ and $Pm\bar{3}m$ structures have 9, 9, 6, 6 and 3 independent c_{ij} respectively, thus in principle, equal numbers of linearly independent equations are sufficient for solving the c_{ij}. However, if more equations are used, they usually give inconsistent solutions of c_{ij}. This may be caused by small violations of the linearity of the stress-strain relationship under some strains and the errors of the first-principles calculations. Thereby, I applied a large number of different strains and averaged the solutions of the equations generated.

A total of 42 different strains were applied, ε_1, ε_2, ε_3, ε_4, ε_5, ε_6, $\varepsilon_1 - \varepsilon_2$, $\varepsilon_1 - \varepsilon_3$, $\varepsilon_2 - \varepsilon_3$, $\varepsilon_4 - \varepsilon_5$, $\varepsilon_4 - \varepsilon_6$, $\varepsilon_5 - \varepsilon_6$, $\varepsilon_1 - \varepsilon_4$, $\varepsilon_1 - \varepsilon_5$, $\varepsilon_1 - \varepsilon_6$, $\varepsilon_2 - \varepsilon_4$, $\varepsilon_2 - \varepsilon_5$, $\varepsilon_2 - \varepsilon_6$, $\varepsilon_3 - \varepsilon_4$, $\varepsilon_3 - \varepsilon_5$, $\varepsilon_3 - \varepsilon_6$ and their negatives, where $\varepsilon_1 = \varepsilon_2 = \varepsilon_3 = 0.01$, $\varepsilon_4 = \varepsilon_5 = \varepsilon_6 = 0.02$. Thus, $42 \times 6 = 252$ equations of the form of (4.1) were generated with respect to the 36 c_{ij}. Additional equations were raised to impose the dependencies between the c_{ij}. For example, the *I*4/*mcm* structure has 6 independent c_{ij} c_{11}, c_{33}, c_{12}, c_{13}, c_{44} and c_{66}, and thus there should be $36 - 6 = 30$ dependency equations. Among them, 15 equations such as $c_{12} - c_{21} = 0$ describe the diagonal symmetry of the stiffness matrix. Twelve equations such as $c_{14} = 0$ indicate the zero values of some c_{ij}. Three equations such as $c_{11} - c_{22} = 0$ impose the relationships between some c_{ij}. The latter two groups of equations arise from the constraints of the crystal class 4/*mmm* of the *I*4/*mcm* structure, and only the upper diagonal c_{ij} are involved because the constraints on the lower diagonal c_{ij} can be implied through the first group of equations specifying the diagonal symmetry. Similarly, the *Pnma*, *Imma*, $R\bar{3}c$ and $Pm\bar{3}m$ perovskite structures have 27, 30, 30 and 33 such dependency equations respectively.

The whole equation system for each structure is the 252 equations of the form of (4.1) plus the dependency equations. Because half of the 42 strains are the negatives of the other half and most

of them are linear combinations of two of ε_1, ε_2, ε_3, ε_4, ε_5 and ε_6, the corresponding equations of the form of (4.1) are linearly dependent. In order to solve such equation systems, the singular value decomposition method (e.g. Parker, 1994) was used. Also, weight factors were applied to the dependency equations to enhance the extent the solution complies with the dependency constraints. The weight factors for *Pnma*, *Imma*, *I*4/*mcm*, $R\bar{3}c$ and $Pm\bar{3}m$ structures are 100, 100, 100,100 and 10 respectively, so that the constraints are obeyed to the fourth digit after the decimal point.

4.4 Results and discussion

4.4.1 Phase transition

The phase transitions between $YAlO_3$ polymorphs at high pressures and 0 K can be determined by their relative enthalpies ΔH, which were obtained from the first-principles calculations as follows. For each polymorph, the *E*-*V* of the optimized structures between −20 and 300 GPa at 20 GPa intervals were interpolated onto a dense volume grid. At each grid point, pressure was calculated by finite difference $P = -\mathrm{d}E/\mathrm{d}V$, and then enthalpy by $H = E + PV$. The *H*-*P* of all of the polymorphs were interpolated onto a uniform pressure grid so that ΔH-*P* could be obtained by subtraction.

The relative enthalpies compared to the *Pnma* structure were used to determine the stabilities of $YAlO_3$ polymorphs with respect to pressure (Figure 4.1). The ΔH to the *I*4/*mcm*, *Imma* and $R\bar{3}c$ structures all fall to zero at ~100 GPa, and above this pressure, they become smaller than, almost equal to and larger than zero respectively. The reduction of ΔH to the *Imma* to zero suggests that the *Pnma* and *Imma* structures evolve to become identical at high pressures. Because the Wentzcovitch algorithm preserves the space group of the structure during its relaxation (Wentzcovitch *et al.*, 1993), the *Pnma* structure can evolve to one of its supergroups *Imma*, but not the reverse. This has been verified by the bond length variation with pressure of the *Pnma* structure (Figure 4.2). Above 100 GPa, two symmetry independent Y-O1 bonds in the *Pnma* structure become equivalent as in the *Imma* structure. Similar behavior is seen in the Y-O2 and Al-O2 bonds. This evolution can also be seen more directly from the tilt angles of the AlO_6

octahedra (Figure 4.3). The *Pnma* structure has the $a^+b^-b^-$ tilt system, meaning in-phase tilting around one pseudo-cubic axis and equal out-of-phase tiltings around the other two axes (Glazer, 1972). The corresponding tilt angles φ_{a^+} and $\varphi_{b^-b^-}$ were calculated following Chapter 2 (Figure 4.3). The φ_{a^+} decreases to zero above 100 GPa and hence results in the $a^0b^-b^-$ tilt system belonging to the *Imma* structure (Glazer, 1972). This transition is allowed to be continuous according to the group theory (Howard and Stokes, 1998).

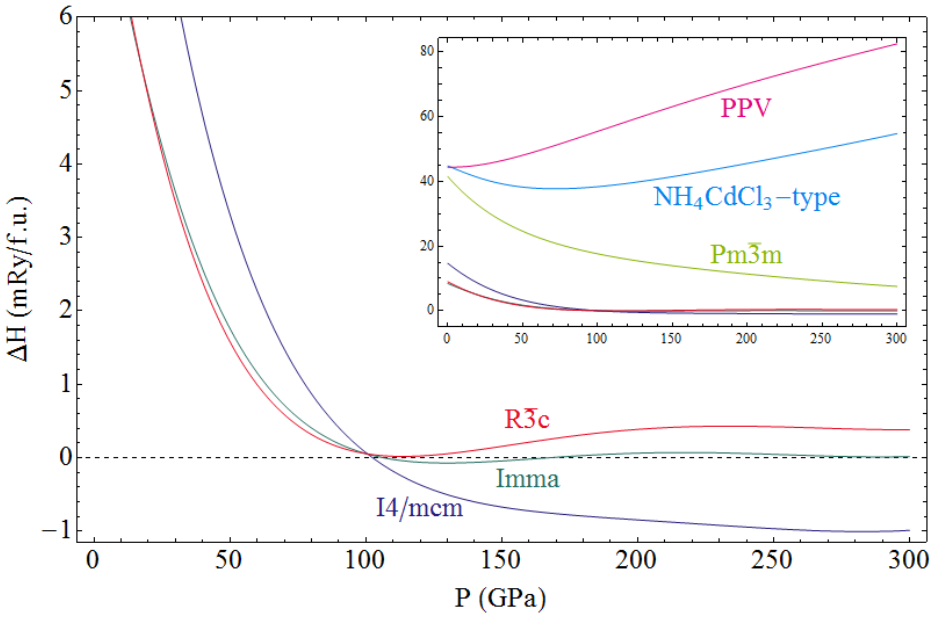

Figure 4.1 Relative enthalpies of $YAlO_3$ polymorphs compared to *Pnma* structure as a function of pressure. The inset figure has full ΔH range.

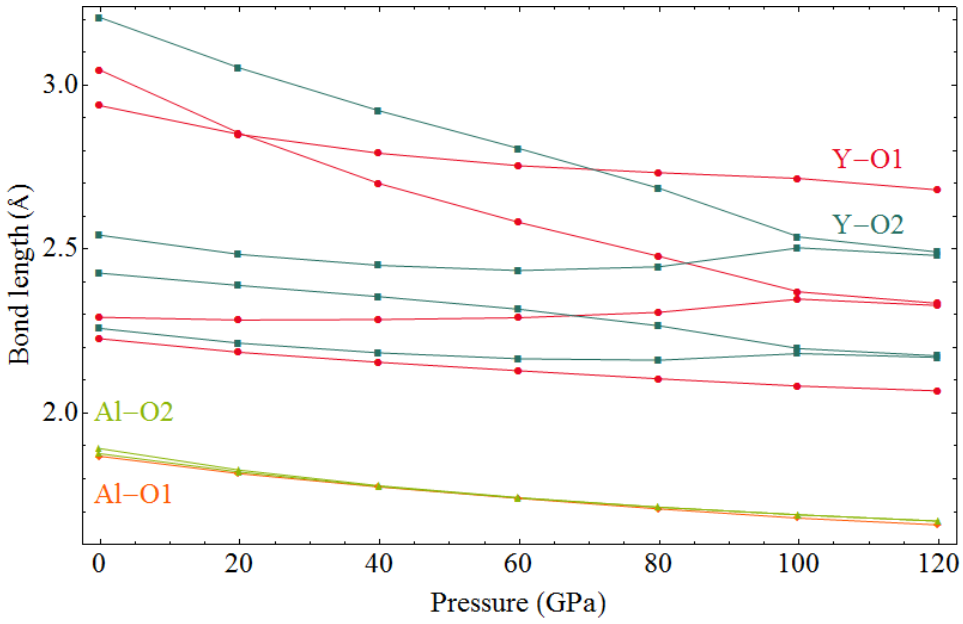

Figure 4.2 Bond lengths of *Pnma* structure as a function of pressure.

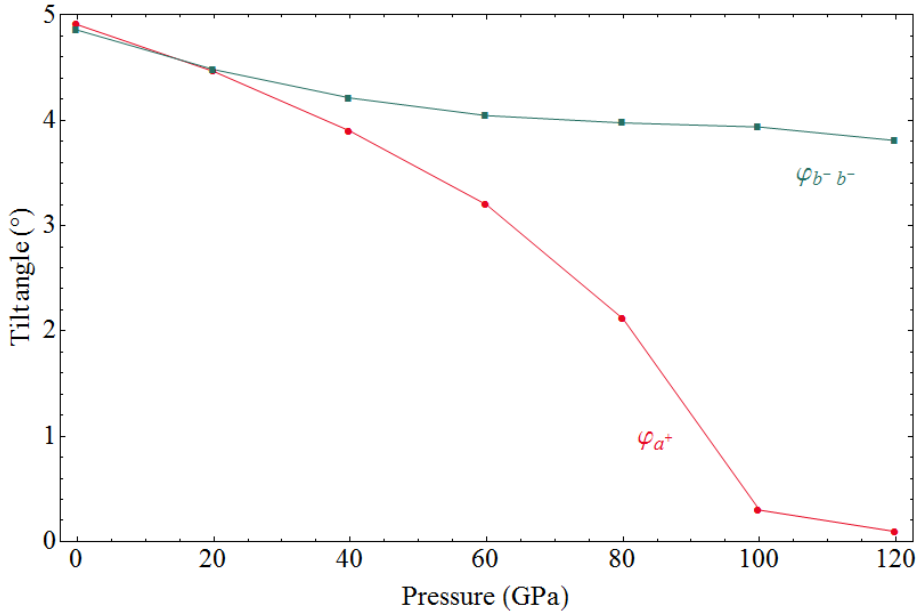

Figure 4.3 Octahedral tilt angles of *Pnma* structure as a function of pressure.

Above 100 GPa, the *I*4/*mcm* structure has the lowest Δ*H* and hence is the stable phase (Figure 4.1). Other than the decreasing bond lengths (Figure 4.4), the only tilt angle φ_{c^-} of the $a^0a^0c^-$ tilt

system of the *I*4/*mcm* structure decreases with increasing pressure (Figure 4.5). If φ_{c^-} continues to approach zero, the *I*4/*mcm* structure will transit to the cubic $Pm\bar{3}m$ structure, as predicted by the general rules for perovskite structural evolution at high pressures (Angel *et al.*, 2005; Zhao *et al.*, 2004a). The ΔH of the $Pm\bar{3}m$ structure drops at a greater rate than that of the *I*4/*mcm* structure (inset in Figure 4.1), which might also be a sign of an *I*4/*mcm* – $Pm\bar{3}m$ transition at some higher pressure. Extrapolation of the φ_{c^-} suggests that the *I*4/*mcm* to $Pm\bar{3}m$ transition would occur at ~1.2 TPa.

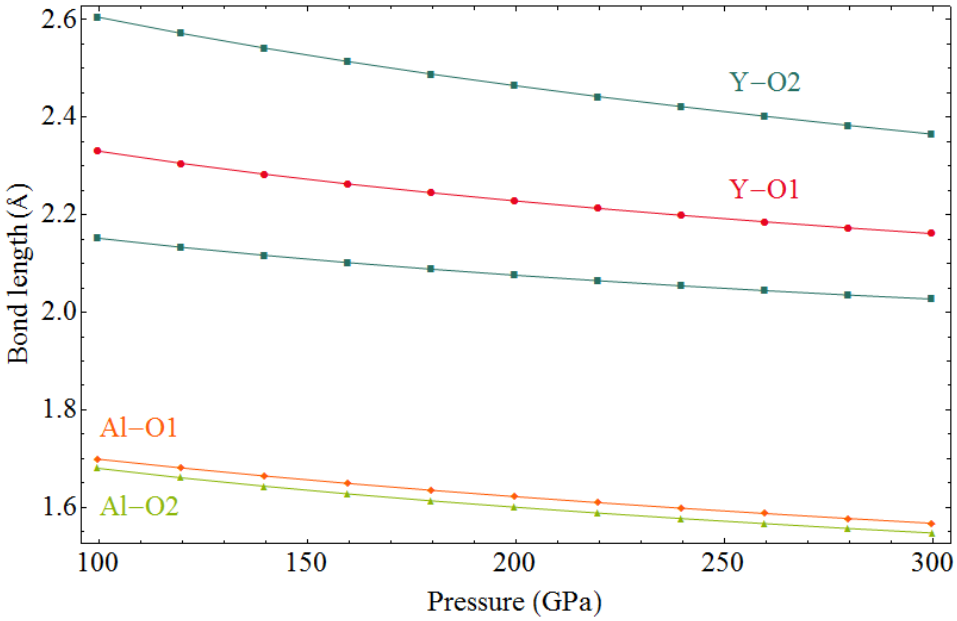

Figure 4.4 Bond lengths of *I*4/*mcm* structure as a function of pressure.

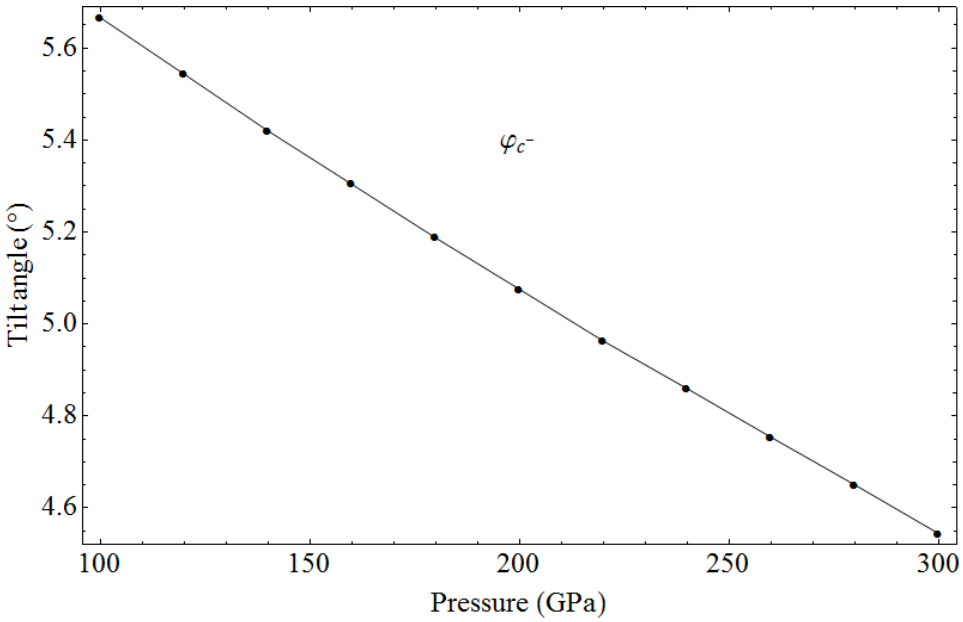

Figure 4.5 Octahedral tilt angle φ_{c^-} of *I*4/*mcm* structure as a function of pressure.

The ΔH values of NH_4CdCl_3-, Gd_2S_3-, U_2S_3-type and PPV structures fall onto just two curves; the NH_4CdCl_3- and Gd_2S_3-type have identical ΔH, as do the U_2S_3-type and PPV (inset in Figure 4.1). Inspection of their optimized structures at all pressures revealed that the Gd_2S_3-type structures change to the NH_4CdCl_3-type after relaxations, and the U_2S_3-type structures change to PPV (Figure 4.6). Both the Gd_2S_3- and NH_4CdCl_3-type structures have *Pnma* space group. The main difference is that in the former the coordination number of the Al site is 7 while it is 6 in the latter. The U_2S_3-type structure has *Pnma* space group but the PPV structure has higher symmetry of *Cmcm*, a supergroup of *Pnma*. The structural difference also lies in the coordination number of the Al site, i.e. 7 in the former while 6 in the latter. When the coordination number changes from 7 to 6, the edge-sharing enneahedra break up into smaller octahedra, which suggests that structures with relatively small octahedral Al sites are energetically favorable for $YAlO_3$. The more stable perovskite structures also belong to this category.

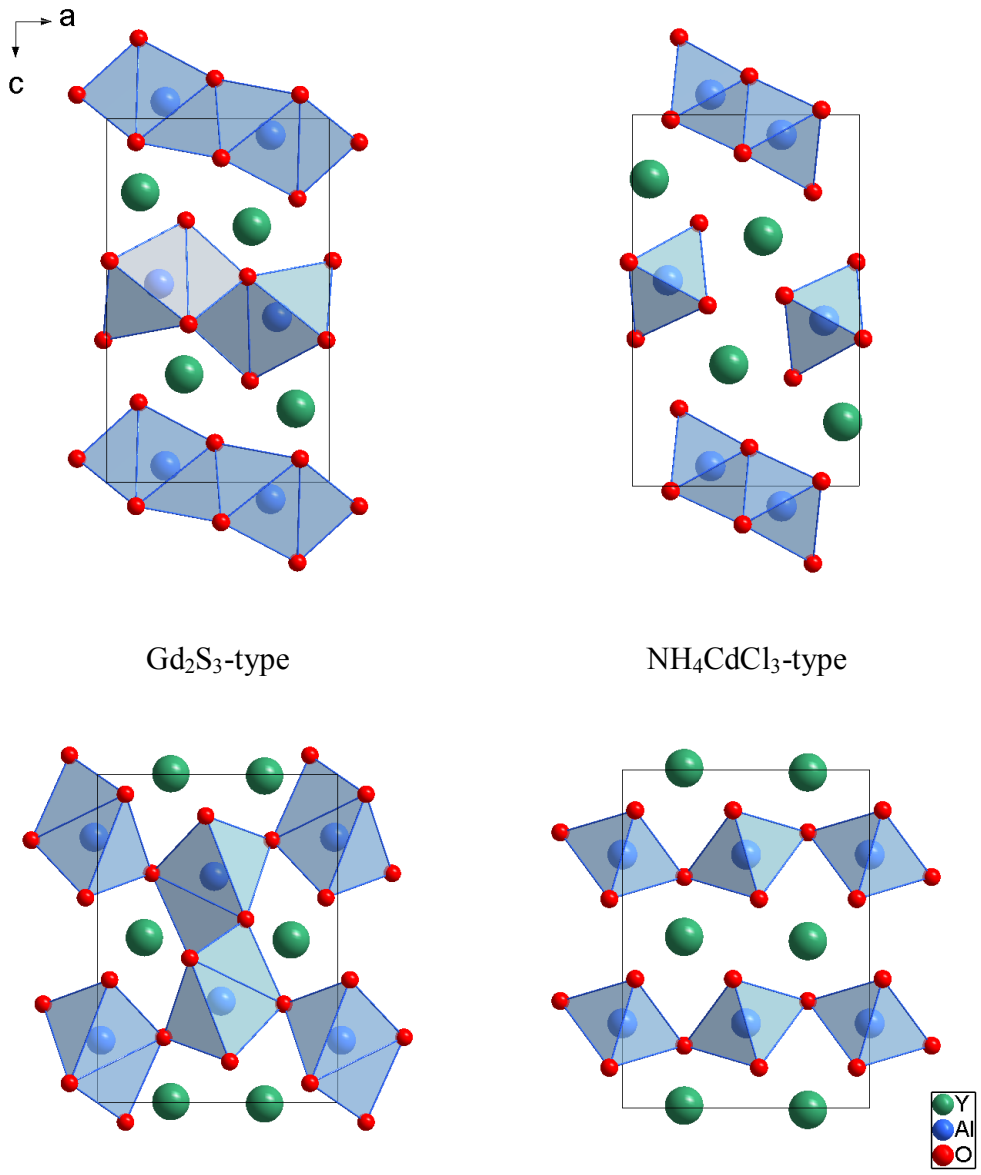

Gd_2S_3-type NH_4CdCl_3-type

U_2S_3-type PPV

Figure 4.6 Structures of NH_4CdCl_3-, Gd_2S_3-, U_2S_3-type and PPV $YAlO_3$ in *Pnma*, *Pnma*, *Pnma* and *Amma* (non-standard of *Cmcm*) settings respectively, viewed along *b* axis. The left two illustrate the initial Gd_2S_3- and U_2S_3-type structures before relaxations and the right two are their final configurations at 0 GPa respectively.

The *Pnma* – *I*4/*mcm* phase transition of $YAlO_3$ perovskite found in this study agrees with the other prediction by first-principles calculations using the generalized gradient approximation

(GGA) (Wu *et al.*, 2006), except that the transition pressure for *Pnma* to *I*4/*mcm* perovskite of 100 GPa determined here is higher than their 80 GPa. This difference is even larger than it seems if considering that LDA often underestimates the transition pressure while GGA may slightly overestimate it (Oganov and Brodholt, 2000). The only reason I could think of is the different structural optimization algorithms used in the two studies. While the Wentzcovitch algorithm I used relaxed both the cell and internal parameters simultaneously, Wu *et al.* (2006) relaxed only one of the two at one time with the other fixed, which might result in non fully optimized structures.

High-temperature experiments of perovskites such as $SrZrO_3$, $SrRuO_3$, $SrRhO_3$, $SrSnO_3$ and $SrTcO_3$ have revealed a *Pnma* – *Imma* – *I*4/*mcm* – $Pm\bar{3}m$ transition series with increasing temperature (Howard *et al.*, 2000; Kennedy *et al.*, 2002; Kennedy *et al.*, 2004; Mountstevens *et al.*, 2005; Thorogood *et al.*, 2011). The stability temperature range of *Imma* can be as limited as 20°C in $SrRhO_3$. In our calculations at high pressures, the ΔH of *Imma* and *I*4/*mcm* structures drop to zero at almost the same pressure (Figure 4.1). If the *Pnma* structure continuously changes to *Imma* shortly before the transition to *I*4/*mcm*, there may be a very small stability pressure range of *Imma* between those of *Pnma* and *I*4/*mcm*, which may be expanded at finite temperatures. This question needs further experimental and theoretical investigations.

4.4.2 Elasticity

The cell parameters of the optimized *Pnma* structure at 0 GPa and 0 K are ~1.5% smaller than the experimental values at room temperature and pressure, leading to the unit cell volume being 4.2% smaller (Table 4.1). The bulk modulus and its pressure derivative at 0 GPa, K_0 and K'_0, were obtained by fitting the third-order $E(V)$ form Birch-Murnaghan equation of state (EOS) to the total energies of the optimized structures. Only the data at −20 – 100 GPa were used in the fitting because the *Pnma* structures actually evolve to *Imma* above 100 GPa. For consistency, the other four perovskite structures also used the data in that pressure range for EOS fittings. The fitted K_0 of the *Pnma* structure is 9.5% greater than the experimental value. The underestimated volume and overestimated bulk modulus are typical for the LDA calculation. Among the other

first-principles studies, our results are in very good agreement with those from Huang *et al.* (2011) using also LDA.

Our static elastic moduli of the *Pnma* structure at 0 GPa compare reasonably with the only other data from Huang *et al.* (2011). Four of the nine independent elastic moduli have differences < 11 GPa while another four have differences < 18 GPa. The biggest difference of 40 GPa lies in c_{22}. But from the percentage perspective, the 12.1% of c_{22} is the third after the 14.4% of c_{13} and 12.4% of c_{12}, both of which have small absolute values. For those structures having no other elastic data to compare, a rough examination is provided by the Voigt-Reuss-Hill (VRH) approximation (Hill, 1952) of the polycrystalline bulk modulus K_H based on the single-crystal elastic moduli. Right elastic moduli should yield K_H which agrees with the K_0 from EOS fitting. In this study, the K_H of the five perovskite structures are all within ±5 GPa of their respective K_0, which suggests that our results of elastic moduli are reasonable.

Table 4.1 Static structural and elastic properties of $YAlO_3$ perovskite at 0 GPa compared with previous studies [a].

	Ross *et al.* (2004) Expt.	Ching and Xu (1999) LDA	Pari *et al.* (2004) LDA	Wu *et al.* (2006) GGA	Muñoz-García *et al.* (2009) GGA	Huang *et al.* (2011) LDA	This study LDA				
							Pnma	*Imma*	*I*4/*mcm*	$R\bar{3}c$	$Pm\bar{3}m$
a	5.32953(49)		5.3288		5.359	5.267	5.248	5.119	5.114	5.187	3.624
b	7.37002(21)		7.5175		7.427	7.290	7.269	7.293			
c	5.17868(29)		5.3087		5.210	5.116	5.107	5.178	7.334	12.415	
V	203.412(16)		212.663	209.9	207.365	196.436	194.814	193.298	191.788	289.303	47.606
K_0	192.1(1.8)	234	218.4	188	207.1	210.2	210.35	208.66	219.50	214.89	227.08
K'_0	7.3(4)	3.75	–	3.82	7.85	4.56	3.863	4.219	4.143	4.117	4.045
c_{11}						299.4	312.99	412.43	384.64	403.95	424.02
c_{22}						330.0	369.79	331.36			
c_{33}						397.0	394.19	465.42	419.85	371.54	
c_{12}						124.2	139.57	107.59	99.36	151.92	132.74
c_{13}						121.7	139.17	107.98	143.26	107.39	

c_{23}	140.3	154.26	147.62			
c_{44}	158.4	149.65	129.48	19.36	131.30	170.28
c_{55}	119.1	108.88	97.41			
c_{66}	162.7	172.57	61.75	112.78		
c_{14}					16.60	
K_{H}^{b}	198.3	214.54	213.05	216.95	211.78	229.84
G_{H}^{b}	127.9	126.29	108.12	61.58	130.75	159.95

[a] Previous studies are all on the stable *Pnma* structure and data in *Pbnm* setting have been converted to *Pnma*. [b] VRH values of bulk and shear moduli are calculated based on elastic moduli.

The *Pnma* – *I*4/*mcm* phase transition are accompanied by the pressure variation in the mechanical stabilities of the provskite structures. The c_{ij}, $i, j = 1, 2, 3$, of the *Pnma*, *Imma* and *I*4/*mcm* structures all increase with increasing pressure, where c_{ii} are much larger than c_{ij} , $i \neq j$ (Figure 4.7, Figure 4.8). Below 60 GPa, the c_{44} of the *I*4/*mcm* structure and the c_{66} of the *Imma* structure become negative indicating that the structures are elastically unstable in this pressure range (Figure 4.9). Above 60 GPa, the c_{44} of the *I*4/*mcm* structure keeps increasing while the c_{55} of the *Imma* structure keeps decreasing towards negative values, which suggests that the *I*4/*mcm* rather than *Imma* is the mechanically stable structure at high pressures. At low pressures, the c_{55} and c_{66} of the *Pnma* structure first increase then decrease, and they approach those of the *Imma* structure at 100 GPa. All the elastic moduli of the *Pnma* structure coincide with those of the *Imma* structure above 100 GPa, which is in accord with the fact that the *Pnma* structures evolve to *Imma* in that pressure range. From the perspective of mechanical stability, the stable structures at low and high pressures are *Pnma* and *I*4/*mcm* respectively.

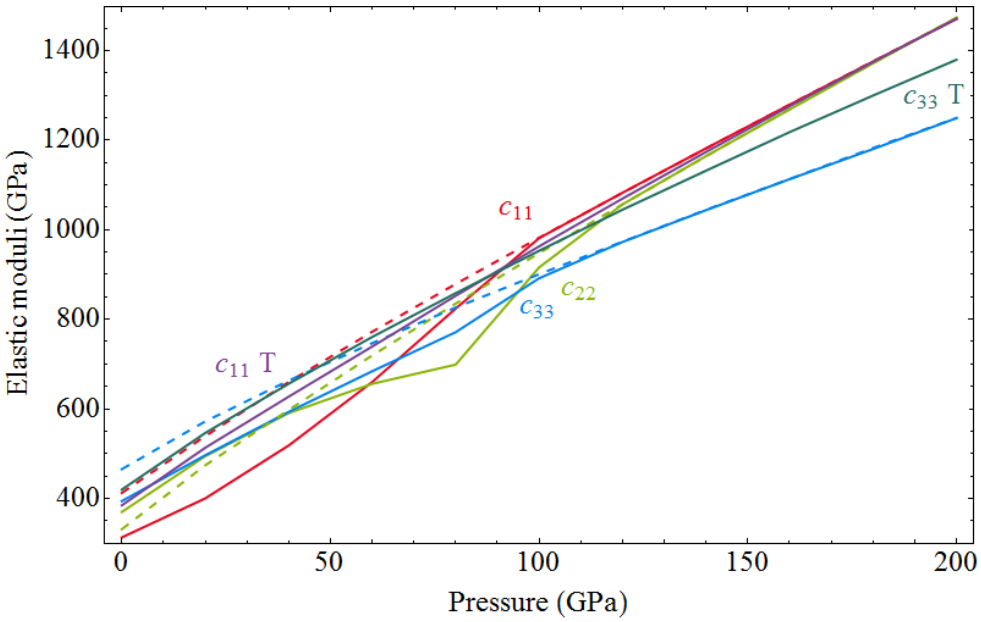

Figure 4.7 Elastic moduli of *Pnma*, *Imma* and *I*4/*mcm* structures as a function of pressure. Labels without T are for *Pnma* (solid) and *Imma* (dashed); Labels with T are for *I*4/*mcm*.

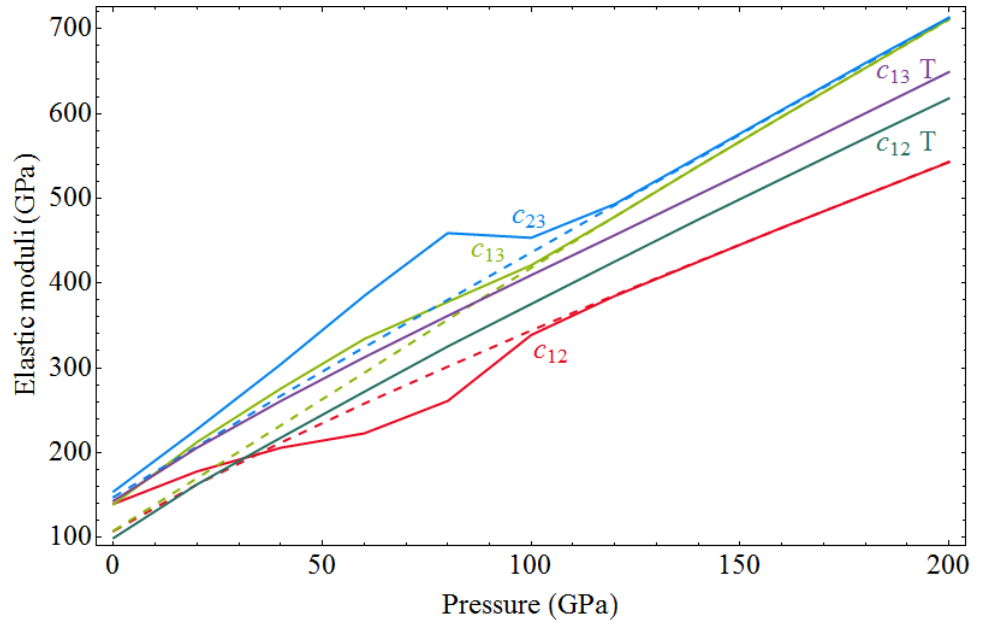

Figure 4.8 Elastic moduli of *Pnma*, *Imma* and *I*4/*mcm* structures as a function of pressure. Labels without T are for *Pnma* (solid) and *Imma* (dashed); Labels with T are for *I*4/*mcm*.

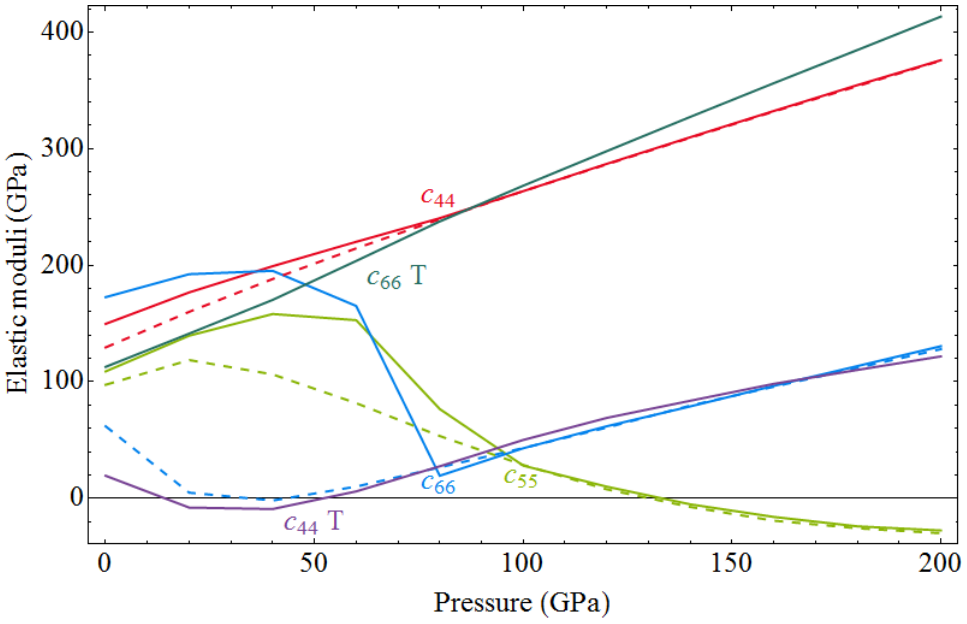

Figure 4.9 Elastic moduli of *Pnma*, *Imma* and *I*4/*mcm* structures as a function of pressure. Labels without T are for *Pnma* (solid) and *Imma* (dashed); Labels with T are for *I*4/*mcm*.

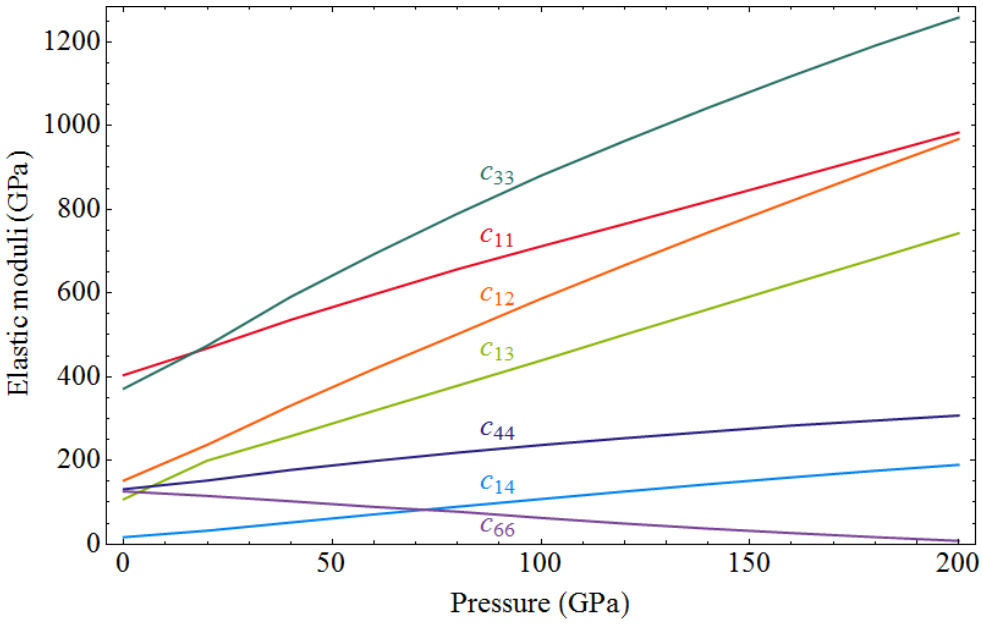

Figure 4.10 Elastic moduli of $R\bar{3}c$ structure as a function of pressure. $c_{66} = (c_{11} - c_{12}) / 2$.

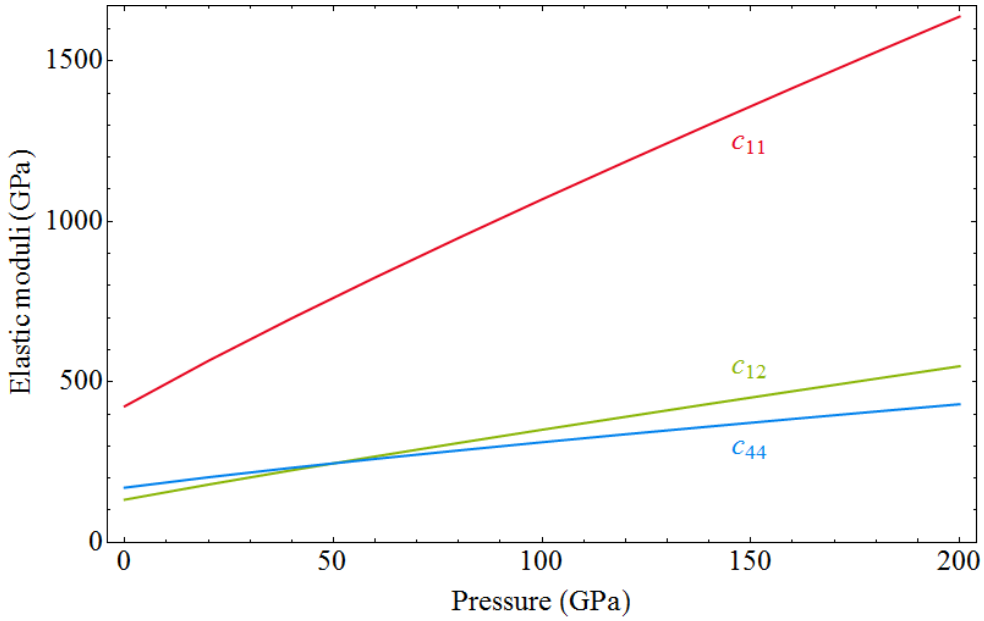

Figure 4.11 Elastic moduli of $Pm\bar{3}m$ structure as a function of pressure.

4.4.3 Phonons

The pressure variations of the stabilities of the five perovskite structures of $YAlO_3$ can be examined through the calculated phonon dispersion curves (Figure 4.13 – Figure 4.17). Although the *Pnma* structure is dynamically stable between 0 and 80 GPa, the A_g mode at the Γ point softens with increasing pressure (Figure 4.13, Figure 4.18). This mode is the in-phase octahedral tilting around the *a* pseudo-cubic axis of the $a^+b^-b^-$ tilt system plus the displacements of the Y atoms (Figure 4.12), so the softening of this mode indicates the $a^+b^-b^-$ to $a^0b^-b^-$ tilt system transformation, i.e. the *Pnma* to *Imma* phase transition. Although the frequency of this mode increases above 100 GPa, imaginary frequencies appear near the Γ point, suggesting that the *Pnma* structure is dynamically unstable above 100 GPa (Figure 4.13).

The *Imma* structure has imaginary frequency at the *Z* point $[\frac{1}{2}\ \frac{1}{2}\ \frac{1}{2}]$ between 0 and 80 GPa (Figure 4.14). With increasing pressure, the imaginary part reduces and the frequency becomes positive. This *Z*-point mode has the same vibrational pattern as the Γ-point A_g mode of the *Pnma*

structure (Figure 4.12). Note that if the *Pnma* symmetry is increased to *Imma*, the reciprocal cell is doubled and the Γ point of *Pnma* becomes the Γ or *Z* point of *Imma*. Actually, when the *Pnma* structure evolves to *Imma*, the soft Γ-point A_g mode of *Pnma* becomes the *Z*-point mode of *Imma* (Figure 4.18). The *Pnma* structure can be seen as the condensation of the in-phase tilting *Z*-point mode of *Imma* (Figure 4.12). The squared frequency of the *Z*-point mode crosses zero at 89 GPa, suggesting that the *Pnma* to *Imma* transition occurs at that pressure (Figure 4.18). At 100 GPa, imaginary frequency reappears near the Γ point, which is clearer at 140 GPa (Figure 4.14). This might imply an *Imma* to *I*4/*mcm* transition occurring shortly after the *Pnma* to *Imma* transition with increasing pressure.

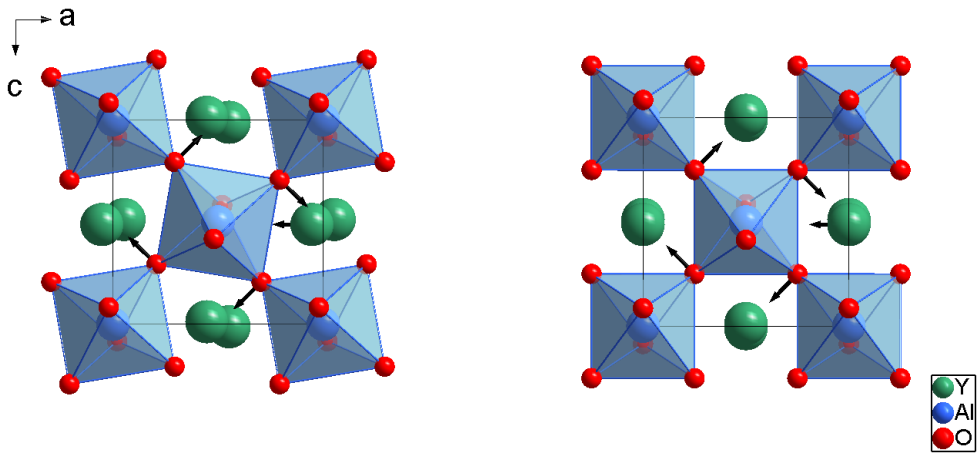

Pnma *Imma*

Figure 4.12 *Pnma* and *Imma* structures viewed along *b* axis. Arrows denote vibrational patterns of soft modes at Γ point of *Pnma* structure and *Z* point $[\frac{1}{2}\ \frac{1}{2}\ \frac{1}{2}]$ of *Imma* structure. Only vibrations of one AlO_6 octahedron and one Y atom are shown for clarity.

The *I*4/*mcm* structure has imaginary frequencies at the *X* and Γ points at 0 GPa (Figure 4.15). The soft doublet E_g modes at the Γ point are the out-of-phase octahedral tiltings around the two *a* pseudo-cubic axes of the $a^0a^0c^-$ tilt system of the *I*4/*mcm* structure, which might suggest that more than one out-of-phase tilting should condense at low pressures as in the *Pnma* structure.

The imaginary frequency near the Γ point disappears above 100 GPa, which is coincident with the appearing of the imaginary frequency near the Γ point in the *Imma* structure (Figure 4.15, Figure 4.14). Also the ΔH of the *Imma* and *I*4/*mcm* structures cross at 100 GPa (Figure 4.1), thus the *Imma* to *I*4/*mcm* transition pressure is 100 GPa. The stability pressure range of the *Imma* structure, i.e. between 89 and 100 GPa, is inside that bounded by the negative c_{66} and c_{55} of the *Imma* structure (Figure 4.9). The squared frequencies of the soft *X*-, Γ-point modes of the *I*4/*mcm* structure become positive above ~60 GPa (Figure 4.18), coincident with that the c_{44} of the *I*4/*mcm* structure becomes positive at ~53 GPa (Figure 4.9).

The Γ-point E_g doublet modes of the $R\bar{3}c$ structure soften with decreasing pressure, with the frequency reduced to zero at 0 GPa (Figure 4.16, Figure 4.18). The c_{14} of the $R\bar{3}c$ structure also approaches zero as pressure decreases to 0 GPa (Figure 4.10), although this does not affect the mechanical stability of the $R\bar{3}c$ structure. The imaginary frequency appears near the Γ point above 100 GPa (Figure 4.16), coincident with that one of the Born stability criteria (Born and Huang, 1954) for rhombohedral structure $(c_{11} - c_{12})\, c_{44} - 2c_{14}^2 > 0$ is violated above ~110 GPa (Figure 4.10). The $R\bar{3}c$ structure is stable dynamically and mechanically between 0 and 100 GPa even though it is energetically metastable relative to *Pnma*.

Although the c_{11}, c_{12} and c_{44} of the $Pm\bar{3}m$ structure meet the Born stability criteria (Born and Huang, 1954) for cubic structure $c_{11} > 0$, $c_{11} - c_{12} > 0$ and $c_{44} > 0$ (Figure 4.11), the Γ-point T_{1u} triplet, *M*-point A_{2g} singlet, and *R*-point T_{1g} triplet modes all soften with decreasing pressure (Figure 4.17, inset in Figure 4.18). The *M*- and *R*-point modes are the in-phase and out-of-phase octahedral tiltings respectively, which might suggest that both tiltings should condense at low pressures as in the *Pnma* structure. Extrapolation of the squared frequency of the *R*-point mode suggests the *I*4/*mcm* to $Pm\bar{3}m$ transition pressure to be ~1.3 TPa, close to the ~1.2 TPa extrapolated from the octahedral tilt angle φ_{c^-} of the *I*4/*mcm* structure. The NH_4CdCl_3-type and PPV structures were found to be dynamically stable up to the highest pressure I did calculations of 300 GPa (Figure 4.19, Figure 4.20).

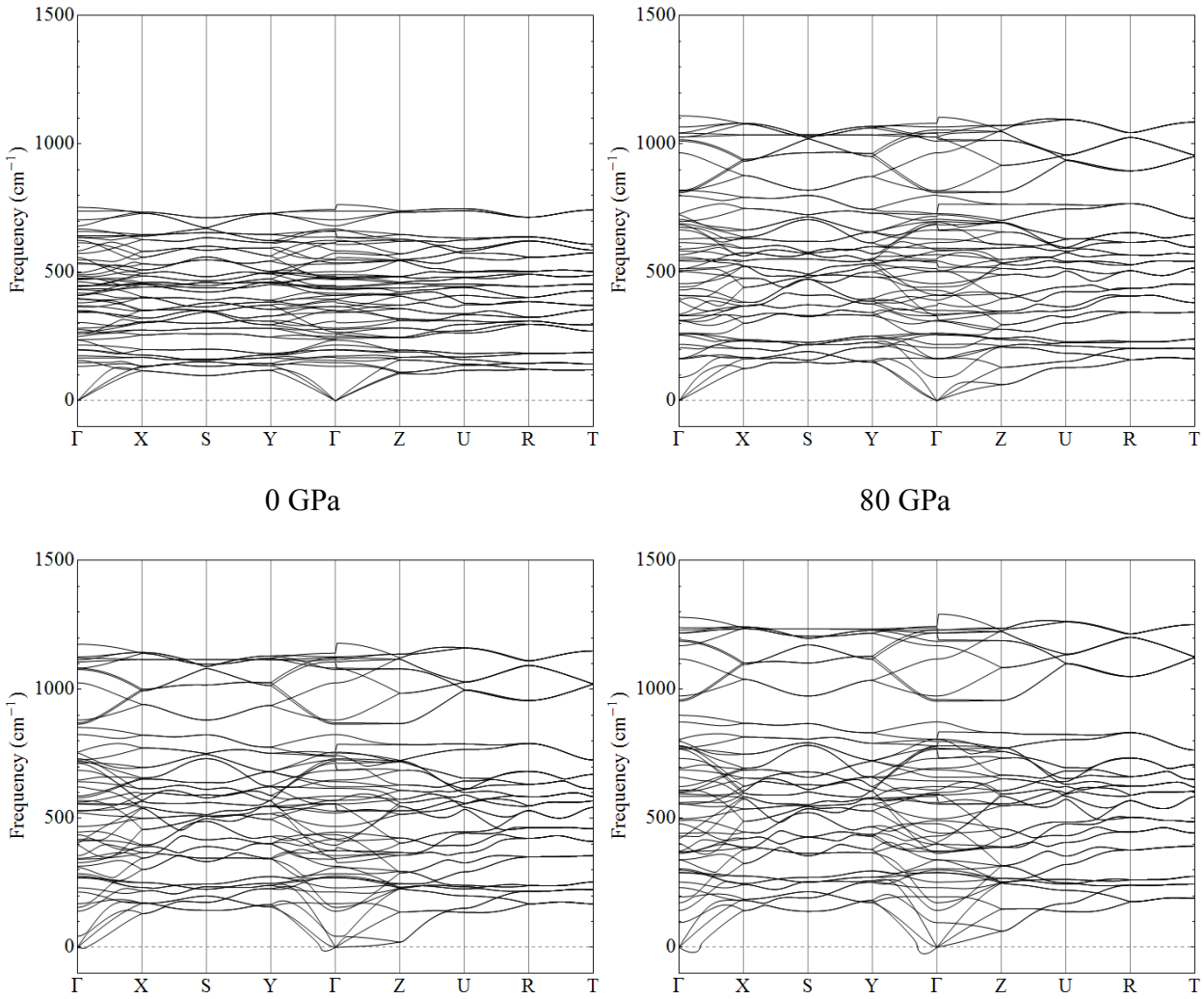

Figure 4.13 Phonon dispersion of *Pnma* structure.

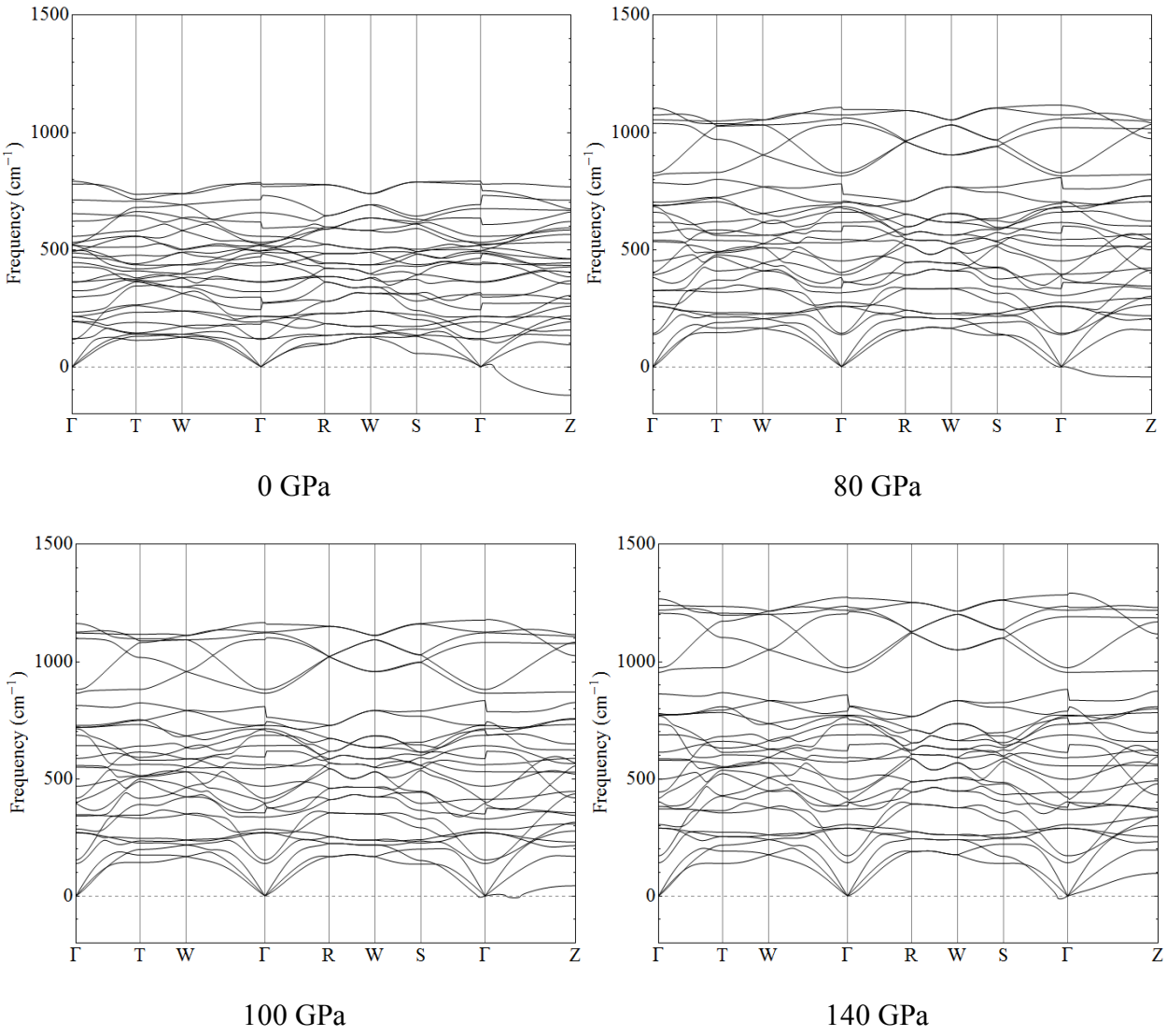

Figure 4.14 Phonon dispersion of *Imma* structure.

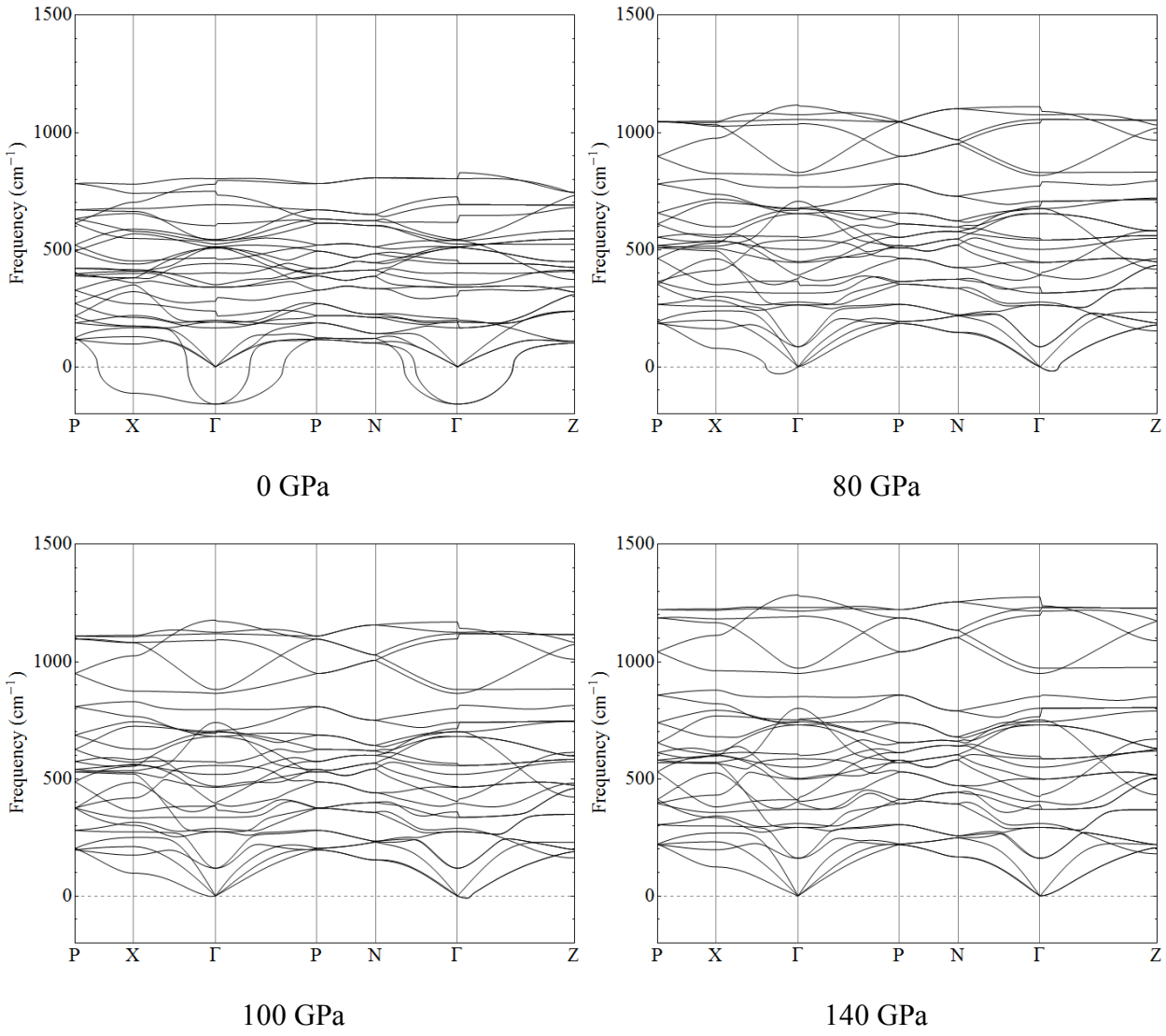

Figure 4.15 Phonon dispersion of *I*4/*mcm* structure.

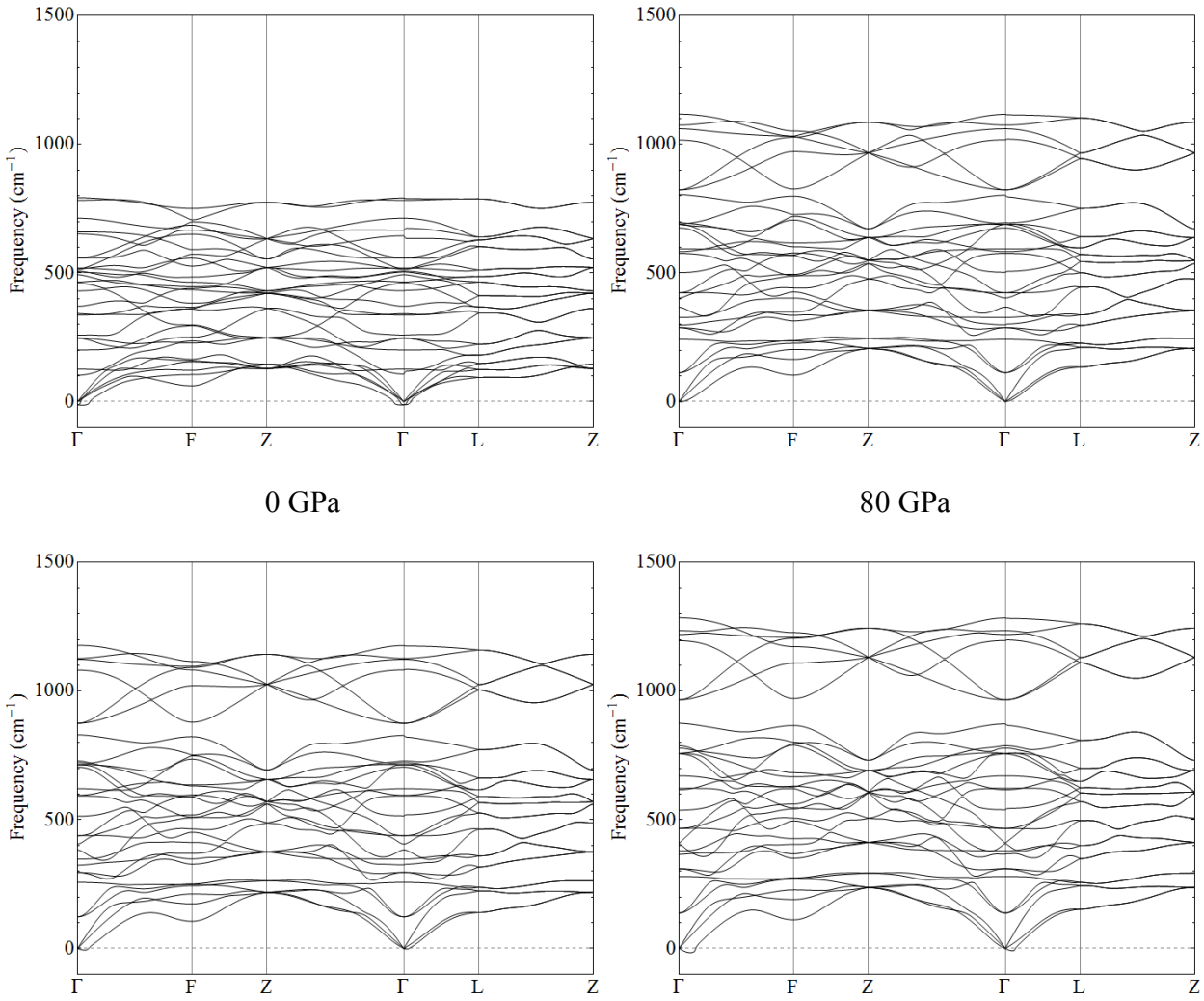

Figure 4.16 Phonon dispersion of $R\bar{3}c$ structure.

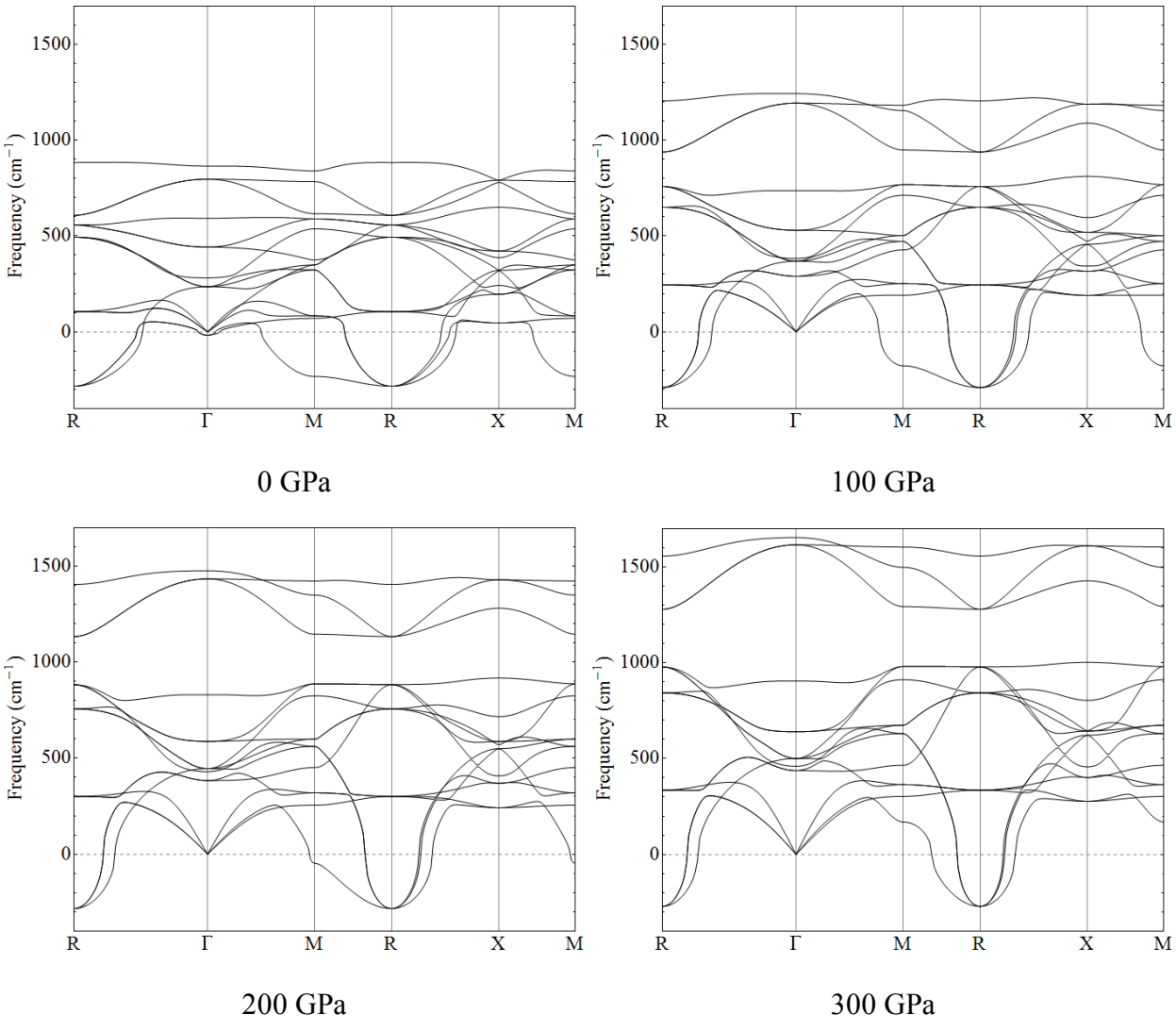

Figure 4.17 Phonon dispersion of $Pm\bar{3}m$ structure.

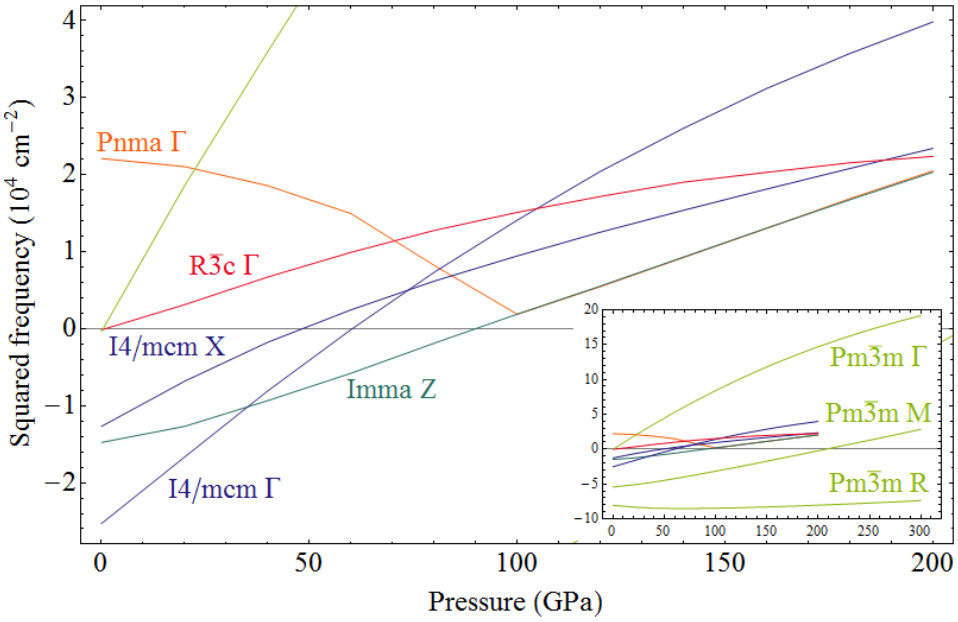

Figure 4.18 Squared frequencies of the soft phonon modes in perovskite structures of $YAlO_3$. The inset has full squared frequency range.

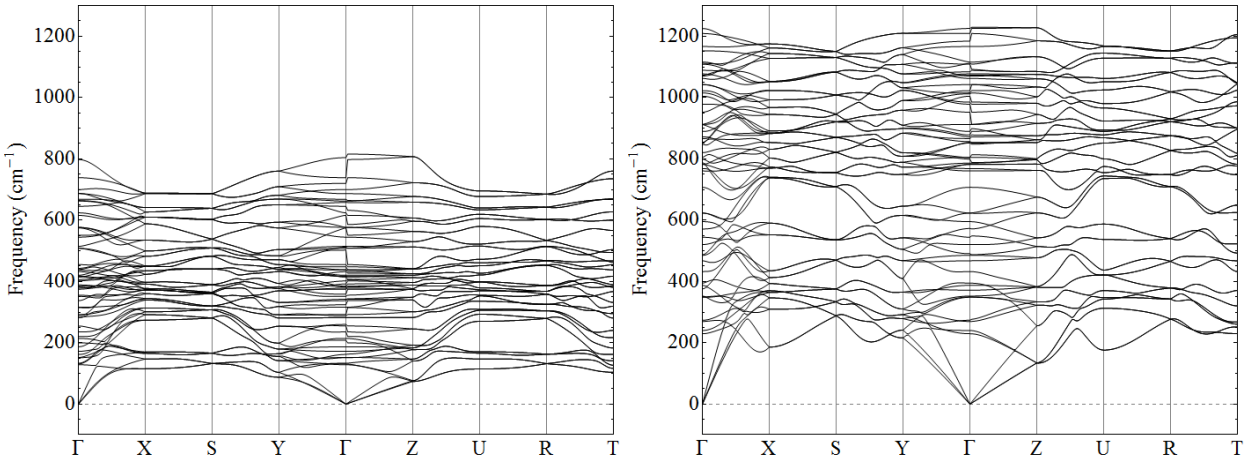

Figure 4.19 Phonon dispersion of NH_4CdCl_3-type structure.

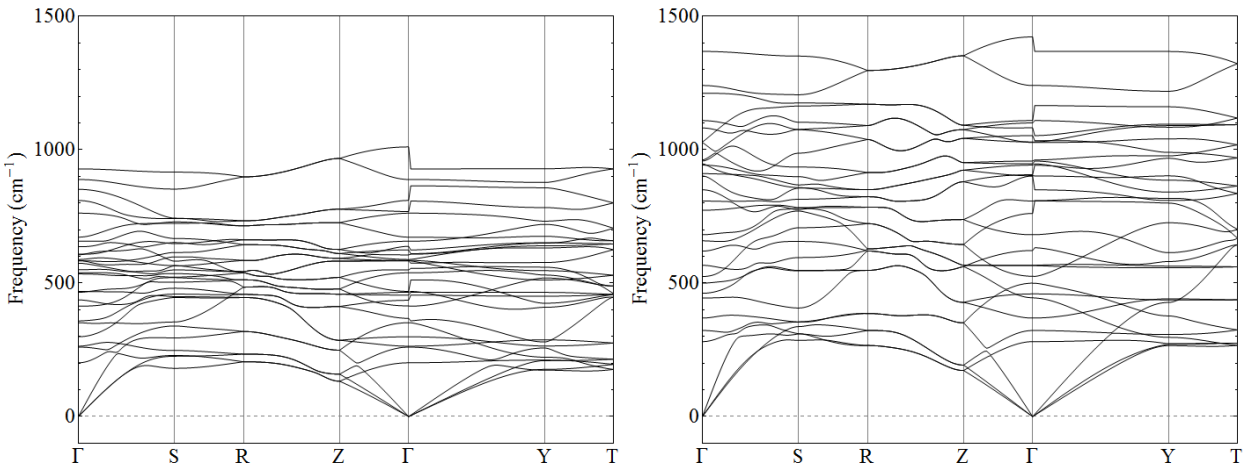

Figure 4.20 Phonon dispersion of PPV structure.

4.4.4 Polyhedral volume ratio V_A/V_B

In the *Pnma* perovskite structure of $YAlO_3$, the AlO_6 octahedra are less tilted with increasing pressure (Figure 4.3), so the volume ratio of the YO_{12} polyhedra and AlO_6 octahedra V_A/V_B increases with pressure (Figure 4.21). A similar trend is also shown in the *I*4/*mcm* structure of $YAlO_3$ (Figure 4.5, Figure 4.21). This indicates that the Al site octahedra are more compressible than the Y sites (Angel *et al.*, 2005), and hence V_A/V_B would increase with pressure all the way through structural evolutions of $YAlO_3$ at high pressures. The V_A/V_B of the $Pm\bar{3}m$ structure is 5 and the *I*4/*mcm* to $Pm\bar{3}m$ transition occurs when the V_A/V_B of the *I*4/*mcm* structure increases to 5. In the NH_4CdCl_3-type and PPV structures of $YAlO_3$, the V_A/V_B are much smaller than those in the perovskite structures (Figure 4.21), thus these two structures could not be the high pressure phases of $YAlO_3$. Similarity was found between the $\Delta V_A/V_B$ and ΔH plots (Figure 4.1, Figure 4.22). Just like the two structures have the same free energy at the phase transition, they also have approximately the same volume ratio of *A* and *B* sites at the transition. For the perovskite structures, the $\Delta V_A/V_B$ qualitatively reproduce the ΔH, which needs to be further tested in perovskites other than $YAlO_3$.

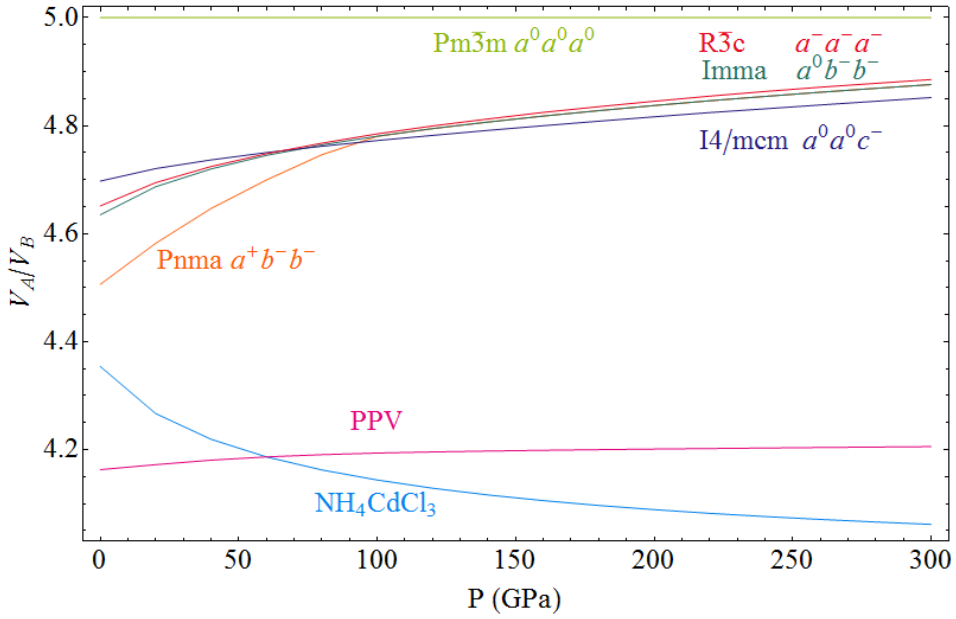

Figure 4.21 Volume ratio of YO_{12} polyhedra and AlO_6 octahedra V_A/V_B of $YAlO_3$ polymorphs as a function of pressure.

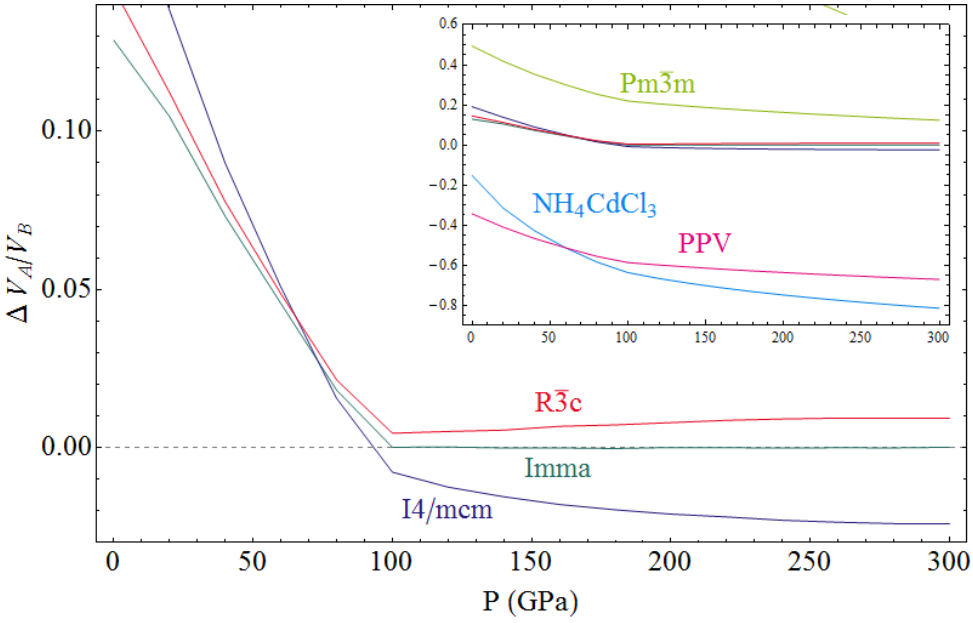

Figure 4.22 $\Delta V_A/V_B$ relative to *Pnma* of $YAlO_3$ polymorphs as a function of pressure.

4.5 Conclusions

The *Pnma – Imma – I*4/*mcm* phase transitions of $YAlO_3$ perovskite at high pressures were determined by relative enthalpies, elasticities and phonons of 9 phases. While the relative enthalpies do not show clearly a stability field for the *Imma* structure, the pressure variations of the soft *Z*-point mode of the *Imma* structure and the phonon dispersions of the *Imma* and *I*4/*mcm* structures provide a clearer *Imma* stability field between 89 and 100 GPa. For the perovskite structures, the pressure ranges of mechanical stability determined by elastic moduli enclose those of dynamical stability determined by phonon dispersions. Although the $NH4CdCl_3$-type and PPV structures are not energetically favorable compared with the perovskite structures, the smaller AlO_6 sites make them dynamically stable and the Gd_2S_3- and U_2S_3-types collapsing to them. The similarity between the $\Delta V_A/V_B$ and ΔH plots shows some insight to the energetic mechanism for the phase transitions, which needs further investigation.

4.6 References

Angel R J, Zhao J and Ross N L 2005 General Rules for Predicting Phase Transitions in Perovskites due to Octahedral Tilting *Phys. Rev. Lett.* **95** 025503

Baroni S, de Gironcoli S, Dal Corso A and Giannozzi P 2001 Phonons and related crystal properties from density-functional perturbation theory *Rev. Mod. Phys.* **73** 515-62

Born M and Huang K 1954 *Dynamical Theory of Crystal Lattices* (Oxford: Clarendon Press)

Ceperley D M and Alder B J 1980 Ground State of the Electron Gas by a Stochastic Method *Phys. Rev. Lett.* **45** 566-9

Ching W Y and Xu Y-N 1999 Nonscalability and nontransferability in the electronic properties of the Y-Al-O system *Phys. Rev. B* **59** 12815-21

Diehl R and Brandt G 1975 Crystal structure refinement of $YAlO_3$, a promising laser material *Mater. Res. Bull.* **10** 85-90

Giannozzi P, Baroni S, Bonini N, Calandra M, Car R, Cavazzoni C, Ceresoli D, Chiarotti G L, Cococcioni M, Dabo I, Corso A D, Gironcoli S d, Fabris S, Fratesi G, Gebauer R, Gerstmann U, Gougoussis C, Kokalj A, Lazzeri M, Martin-Samos L, Marzari N, Mauri F, Mazzarello R, Paolini S, Pasquarello A, Paulatto L, Sbraccia C, Scandolo S, Sclauzero G, Seitsonen A P, Smogunov A, Umari P and Wentzcovitch R M 2009 QUANTUM ESPRESSO: a modular and open-source software project for quantum simulations of materials *J. Phys.: Condens. Matter* **21** 395502

Glazer A M 1972 The classification of tilted octahedra in perovskites *Acta Cryst.* **B28** 3384-92

Hill R 1952 The Elastic Behaviour of a Crystalline Aggregate *Proc. Phys. Soc. A* **65** 349

Hohenberg P and Kohn W 1964 Inhomogeneous Electron Gas *Phys. Rev.* **136** B864-B71

Howard C J, Knight K S, Kennedy B J and Kisi E H 2000 The structural phase transitions in strontium zirconate revisited *J. Phys.: Condens. Matter* **12** L677

Howard C J and Stokes H T 1998 Group-Theoretical Analysis of Octahedral Tilting in Perovskites *Acta Cryst.* **B54** 782-9

Huang Z, Feng J and Pan W 2011 First-principles calculations of mechanical and thermodynamic properties of $YAlO_3$ *Comp. Mater. Sci.* **50** 3056-62

Kennedy B J, Hunter B A and Hester J R 2002 Synchrotron x-ray diffraction reexamination of the sequence of high-temperature phases in $SrRuO_3$ *Phys. Rev. B* **65** 224103
Kennedy B J, Yamaura K and Takayama-Muromachi E 2004 High temperature structural studies of $SrRhO_3$ *J. Phys. Chem. Solids* **65** 1065-9
Kleinman L and Bylander D M 1982 Efficacious Form for Model Pseudopotentials *Phys. Rev. Lett.* **48** 1425-8
Monkhorst H J and Pack J D 1976 Special points for Brillouin-zone integrations *Phys. Rev. B* **13** 5188-92
Mountstevens E H, Redfern S A T and Attfield J P 2005 Order-disorder octahedral tilting transitions in $SrSnO_3$ perovskite *Phys. Rev. B* **71** 220102
Muñoz-García A B, Anglada E and Seijo L 2009 First-principles study of the structure and the electronic structure of yttrium aluminum garnet $Y_3Al_5O_{12}$ *Inter. J. Quant. Chem.* **109** 1991-8
Oganov A R and Brodholt J P 2000 High-pressure phases in the Al_2SiO_5 system and the problem of aluminous phase in the Earth's lower mantle: ab initio calculations *Phys. Chem. Miner.* **27** 430-9
Pari G, Mookerjeee A and Bhattacharya A K 2004 Study of α-Al_2O_3 and the role of Y in $YAlO_3$ and $Y_3Al_5O_{12}$ by first principles electronic structure calculations *Phys. B: Condens. Matter* **353** 192-200
Parker R L 1994 *Geophysical Inverse Theory* (Princeton: Princeton University Press)
Perdew J P and Zunger A 1981 Self-interaction correction to density-functional approximations for many-electron systems *Phys. Rev. B* **23** 5048-79
Ross N L, Zhao J and Angel R J 2004 High-pressure single-crystal X-ray diffraction study of $YAlO_3$ perovskite *J. Solid State Chem.* **177** 1276-84
Thorogood G J, Avdeev M, Carter M L, Kennedy B J, Ting J and Wallwork K S 2011 Structural phase transitions and magnetic order in $SrTcO_3$ *Dalton Trans.* **40** 7228-33
Troullier N and Martins J L 1991 Efficient pseudopotentials for plane-wave calculations *Phys. Rev. B* **43** 1993-2006
Tsuchiya T, Yusa H and Tsuchiya J 2007 Post-Rh_2O_3(II) transition and the high pressure-temperature phase diagram of gallia: A first-principles and x-ray diffraction study *Phys. Rev. B* **76** 174108
Umemoto K and Wentzcovitch R M 2008 Prediction of an U_2S_3-type polymorph of Al_2O_3 at 3.7 Mbar *Proc. Natl. Acad. Sci.* **105** 6526-30
Wentzcovitch R M 1991 Invariant molecular-dynamics approach to structural phase transitions *Phys. Rev. B* **44** 2358-61
Wentzcovitch R M, Martins J L and Price G D 1993 Ab initio molecular dynamics with variable cell shape: Application to $MgSiO_3$ *Phys. Rev. Lett.* **70** 3947-50
Wu X, Qin S and Wu Z 2006 Generalized gradient approximation calculations of the pressure-induced phase transition of $YAlO_3$ perovskite *J. Phys.: Condens. Matter* **18** 3907
Yusa H, Tsuchiya T, Tsuchiya J, Sata N and Ohishi Y 2008 α-Gd_2S_3-type structure in In_2O_3: Experiments and theoretical confirmation of a high-pressure polymorph in sesquioxide *Phys. Rev. B* **78** 092107
Zhao J, Ross N L and Angel R J 2004a New view of the high-pressure behaviour of $GdFeO_3$-type perovskites *Acta Cryst.* **B60** 263-71
Zhao J, Ross N L and Angel R J 2004b Polyhedral control of the rhombohedral to cubic phase transition in $LaAlO_3$ perovskite *J. Phys.: Condens. Matter* **16** 8763-73
Zhao J, Ross N L, Angel R J, Carpenter M A, Howard C J, Pawlak D A and Lukasiewicz T 2009 High-pressure crystallography of rhombohedral $PrAlO_3$ perovskite *J. Phys.: Condens. Matter* **21** 235403

Chapter 5: Conclusions and comments

The octahedral tilt angles derived from the amplitudes of the M_3^+ and R_4^+ symmetry-adapted modes provide a quantitative description of the tiltings of the BO_6 octahedra around each of the three pseudo-cubic axes. Previously, the tilt angles were only unambiguously defined in simple tilt systems such as $a^0a^0c^-$ and $a^-a^-a^-$. This method expands the tilt angle definition to more complicated tilt systems such as $a^+b^-b^-$. Calculated by this method, the in-phase tilt angle in the $YAlO_3$ perovskite clearly shows the continuous change from the $a^+b^-b^-$ to $a^0b^-b^-$ tilt system with increasing pressure (Figure 4.3). The advantage of using the online software *ISODISTORT* is that it gives the same results of the mode amplitudes no matter what setting is used for a structure. So to calculated tilt angles, one does not need to convert, say the cif file generated by refinement software to a standard form.

The calculation of the elastic moduli of $LaAlO_3$ perovskite was found to be difficult. If each of the elastic moduli is only calculated from one stress-strain equation (4.1), the results will have large errors. The errors are easier to see if the elastic moduli calculated at a range of pressures are plotted against pressure. The curves are likely to go up and down randomly with pressure which rarely happens for most materials. And combinations of elastic moduli which should have values related by symmetry constraints usually do not quite obey the exact relations. Thus, a scheme of averaging a large number of stress-strain equations was adopted. A large number of different strains were applied and six times number of equations were obtained. The resulting equation system has far more equations than the number of unknowns and most of them are linearly dependent. The singular value decomposition method was used to solve this type of equation system. More equations with weight factors were added to enforce the dependencies between the elastic moduli.

This large number of strain schemes was found to be necessary only for rhombohedral perovskite. Fewer strains are enough for cubic, tetragonal and orthorhombic perovskites. Note that the symmetry of rhombohedral perovskite is reduced a lot when most strains are applied, while for cubic, tetragonal and orthorhombic perovskites, they are still highly symmetric when

most strains are applied. So, the less symmetry restrictions to the atomic relaxation in rhombohedral perovskite might be the reason for the inaccurate relaxation and stress results.

Landau parameters were calibrated using data from first-principles calculations for the first time. First-principles calculations can provide data which are not available in experiments such as bare cell parameters, elastic moduli and excess free energy (Figure 3.3, Figure 3.14, Figure 3.7). These data either avoid approximations in experimental studies or provide additional equations to fit Landau parameters (Figure 3.17). Octahedral tilt angles were used as the order parameter components, giving them more apparent structural meaning (Figure 3.4). The Landau expected discontinuities of the elastic moduli across the phase transition are less possible to observe in first-principles calculations, because if the structural change is continuous, the elastic moduli calculated based on the gradually changing structures also tend to be continuous (Figure 3.20).

In second-order phase transitions of perovskite such as the $R\bar{3}c - Pm\bar{3}m$ transition in $LaAlO_3$ perovskite, phonon softenings were found in both structures towards the transition pressure (Figure 3.8 – Figure 3.11). Because the relative enthalpy gradually approaches zero in second-order phase transition, it is hard to determine the transition pressure by this, especially when the errors of the first-principles calculations are of comparable order (Figure 3.7). So, the pressure variations of the frequencies of the soft phonon modes provide a better way to determine the transition pressure (Figure 3.12). The *Pnma – Imma* continuous transition in $YAlO_3$ perovskite were analyzed using a similar approach.

Appendix A: Displacive mode decomposition and V_A/V_B as a function of mode amplitudes for 15 perovskite structures

a_p denotes the cell dimension of the cubic aristotype. The mode amplitude is a fraction of a_p. The prime symbol in d' is omitted for tidiness. The three subscripts of d are, in sequence: the relevant atom type, the irrep and the group of digits indicating the linear combination of the corresponding basis modes of the irrep. The V_A/V_B expressions are the same as in Table 3 of the text, with that following the equal sign is in terms of the amplitudes of all the symmetry-adapted modes of X anions condensed in each perovskite structure, and that following the approximately equal sign is in terms of only the tilt mode amplitudes.

---

a $a^0a^0a^0$ No. 221 $Pm\bar{3}m$

$a = b = c = a_p$

A: (1*b*) $\frac{1}{2}, \frac{1}{2}, \frac{1}{2}$

B: (1*a*) 0, 0, 0

X: (3*d*) $\frac{1}{2}$, 0, 0

$\frac{V_A}{V_B} = 5$

---

b $a^-a^-a^-$ No. 167 $R\bar{3}c$

$a = b \approx \sqrt{2}a_p$, $c \approx 2\sqrt{3}a_p$, hexagonal cell

A: (6*a*) 0, 0, $\frac{1}{4}$

B: (6*b*) 0, 0, 0

X: (18*e*) x ($\approx \frac{1}{2}$), 0, $\frac{1}{4}$

$$d_{\mathrm{X},R_4^+,123} + \frac{1}{2} = x_{\mathrm{X}}$$

$$\frac{V_{\mathrm{A}}}{V_{\mathrm{B}}} = \frac{6}{1 + 4 \cdot 3 d^2_{\mathrm{X},R_4^+,123}} - 1$$

---

c $a^0a^0c^+$ No. 127 *P*4/*mbm*

$a = b \approx \sqrt{2}a_p$, $c \approx a_p$

A: (2*c*) 0, $\frac{1}{2}$, $\frac{1}{2}$

B: (2*a*) 0, 0, 0

X1: (2*b*) 0, 0, $\frac{1}{2}$

X2: (4*g*) x ($\approx \frac{1}{4}$), $x + \frac{1}{2}$, 0

$$\frac{1}{2} d_{\mathrm{X},M_3^+,1} + \frac{1}{4} = x_{\mathrm{X2}}$$

$$\frac{V_{\mathrm{A}}}{V_{\mathrm{B}}} = \frac{6}{1 + 4 d^2_{\mathrm{X},M_3^+,1}} - 1$$

---

d $a^0a^0c^-$ No. 140 *I*4/*mcm*

$a = b \approx \sqrt{2}a_p$, $c \approx 2a_p$

A: (4*b*) 0, $\frac{1}{2}$, $\frac{1}{4}$

B: (4*c*) 0, 0, 0

X1: (4*a*) 0, 0, $\frac{1}{4}$

X2: (8*h*) x ($\approx \frac{1}{4}$), $x + \frac{1}{2}$, 0

$$\frac{1}{2}d_{\mathrm{X},R_4^+,1}+\frac{1}{4}=x_{\mathrm{X2}}$$

$$\frac{V_\mathrm{A}}{V_\mathrm{B}}=\frac{6}{1+4d^2_{\mathrm{X},R_4^+,1}}-1$$

---

e $a^0b^-b^-$ No. 74 *Imma*

$a \approx \sqrt{2}a_p$, $b \approx 2a_p$, $c \approx \sqrt{2}a_p$

A: (4*e*) 0, $\frac{1}{4}$, z ($\approx \frac{1}{2}$)

B: (4*a*) 0, 0, 0

X1: (4*e*) 0, $\frac{1}{4}$, z (≈ 0)

X2: (8*g*) $\frac{1}{4}$, y (≈ 0), $\frac{3}{4}$

$$\begin{pmatrix} -1 & 0 & 0 \\ 0 & 1 & -1 \\ 0 & \frac{1}{2} & \frac{1}{2} \end{pmatrix}\begin{pmatrix} d_{\mathrm{A},R_5^+,12} \\ d_{\mathrm{X},R_4^+,12} \\ d_{\mathrm{X},R_5^+,12} \end{pmatrix}+\begin{pmatrix} \frac{1}{2} \\ 0 \\ 0 \end{pmatrix}=\begin{pmatrix} z_\mathrm{A} \\ z_\mathrm{X1} \\ y_\mathrm{X2} \end{pmatrix}$$

$$\frac{V_\mathrm{A}}{V_\mathrm{B}}=\frac{6}{1+8d^2_{\mathrm{X},R_4^+,12}-8d^2_{\mathrm{X},R_5^+,12}}-1$$
$$\approx \frac{6}{1+4\cdot 2d^2_{\mathrm{X},R_4^+,12}}-1$$

---

f $a^0b^-c^-$ No. 12 *I*2/*m* (non-standard setting of *C*2/*m*)

$a \approx \sqrt{2}a_p$, $b \approx 2a_p$, $c \approx \sqrt{2}a_p$, $\beta \approx 90°$

A: (4*i*) x ($\approx \frac{1}{4}$), 0, z ($\approx \frac{3}{4}$)

B: (4*e*) $\frac{1}{4}, \frac{1}{4}, \frac{1}{4}$

X1: (4*i*) x ($\approx \frac{1}{4}$), 0, z ($\approx \frac{1}{4}$)

X2: (4*g*) 0, y ($\approx \frac{1}{4}$), 0

X3: (4*h*) $\frac{1}{2}$, y ($\approx \frac{1}{4}$), 0

$$\begin{pmatrix} \frac{1}{2} & -\frac{1}{2} & 0 & 0 & 0 & 0 \\ -\frac{1}{2} & -\frac{1}{2} & 0 & 0 & 0 & 0 \\ 0 & 0 & \frac{1}{2} & \frac{1}{2} & -\frac{1}{2} & \frac{1}{2} \\ 0 & 0 & \frac{1}{2} & -\frac{1}{2} & -\frac{1}{2} & -\frac{1}{2} \\ 0 & 0 & -\frac{1}{2} & 0 & -\frac{1}{2} & 0 \\ 0 & 0 & 0 & \frac{1}{2} & 0 & -\frac{1}{2} \end{pmatrix} \begin{pmatrix} d_{\mathrm{A},R_5^+,1} \\ d_{\mathrm{A},R_5^+,2} \\ d_{\mathrm{X},R_4^+,1} \\ d_{\mathrm{X},R_4^+,2} \\ d_{\mathrm{X},R_5^+,1} \\ d_{\mathrm{X},R_5^+,2} \end{pmatrix} + \begin{pmatrix} \frac{1}{4} \\ \frac{3}{4} \\ \frac{1}{4} \\ \frac{1}{4} \\ \frac{1}{4} \\ \frac{1}{4} \end{pmatrix} = \begin{pmatrix} x_{\mathrm{A}} \\ z_{\mathrm{A}} \\ x_{\mathrm{X1}} \\ z_{\mathrm{X1}} \\ y_{\mathrm{X2}} \\ y_{\mathrm{X3}} \end{pmatrix}$$

$$\frac{V_{\mathrm{A}}}{V_{\mathrm{B}}} = \frac{6}{1 + 4d^2_{\mathrm{X},R_4^+,1} + 4d^2_{\mathrm{X},R_4^+,2} - 4d^2_{\mathrm{X},R_5^+,1} - 4d^2_{\mathrm{X},R_5^+,2}} - 1$$

$$\approx \frac{6}{1 + 4\left(d^2_{\mathrm{X},R_4^+,1} + d^2_{\mathrm{X},R_4^+,2}\right)} - 1$$

---

g $a^-b^-b^-$ No. 15 *I*2/*a* (non-standard setting of *C*2/*c*)

$a \approx 2a_p$, $b \approx \sqrt{2}a_p$, $c \approx \sqrt{2}a_p$, $\alpha \approx 90°$

A: (4*e*) $\frac{1}{4}$, y (≈ 0), 0

B: (4*b*) 0, $\frac{1}{2}$, 0

X1: (4*e*) $\frac{1}{4}$, y ($\approx \frac{1}{2}$), 0

X2: (8*f*) x (≈ 0), y ($\approx \frac{1}{4}$), z ($\approx \frac{1}{4}$)

$$\begin{pmatrix} 1 & 0 & 0 & 0 & 0 \\ 0 & 0 & 1 & 0 & 1 \\ 0 & 0 & \frac{1}{2} & 0 & -\frac{1}{2} \\ 0 & -\frac{1}{2} & 0 & -\frac{1}{2} & 0 \\ 0 & \frac{1}{2} & 0 & -\frac{1}{2} & 0 \end{pmatrix} \begin{pmatrix} d_{\mathrm{A},R_5^+,13} \\ d_{\mathrm{X},R_3^+,12} \\ d_{\mathrm{X},R_4^+,13} \\ d_{\mathrm{X},R_4^+,2} \\ d_{\mathrm{X},R_5^+,13} \end{pmatrix} + \begin{pmatrix} 0 \\ \frac{1}{2} \\ 0 \\ \frac{1}{4} \\ \frac{1}{4} \end{pmatrix} = \begin{pmatrix} y_{\mathrm{A}} \\ y_{\mathrm{X1}} \\ x_{\mathrm{X2}} \\ y_{\mathrm{X2}} \\ z_{\mathrm{X2}} \end{pmatrix}$$

$$\frac{V_{\mathrm{A}}}{V_{\mathrm{B}}} = \frac{6}{1 - 4d^2_{\mathrm{X},R_3^+,12} + 8d^2_{\mathrm{X},R_4^+,13} + 4d^2_{\mathrm{X},R_4^+,2} - 8d^2_{\mathrm{X},R_5^+,13}} - 1$$

$$\approx \frac{6}{1 + 4\left(2d^2_{\mathrm{X},R_4^+,13} + d^2_{\mathrm{X},R_4^+,2}\right)} - 1$$

---

h $a^+b^-b^-$ No. 62 *Pnma*

$a \approx \sqrt{2}a_p$, $b \approx 2a_p$, $c \approx \sqrt{2}a_p$

A: (4*c*) x ($\approx \frac{1}{2}$), $\frac{1}{4}$, z (≈ 0)

B: (4*a*) 0, 0, 0

X1: (4*c*) x (≈ 0), $\frac{1}{4}$, z (≈ 0)

X2: (8*d*) x ($\approx \frac{3}{4}$), y (≈ 0), z ($\approx \frac{1}{4}$)

$$\begin{pmatrix} 0 & 1 & 0 & 0 & 0 & 0 & 0 \\ -1 & 0 & 0 & 0 & 0 & 0 & 0 \\ 0 & 0 & 0 & 0 & 0 & 0 & -1 \\ 0 & 0 & 0 & 0 & -1 & 1 & 0 \\ 0 & 0 & -\frac{1}{2} & \frac{1}{2} & 0 & 0 & 0 \\ 0 & 0 & 0 & 0 & \frac{1}{2} & \frac{1}{2} & 0 \\ 0 & 0 & \frac{1}{2} & \frac{1}{2} & 0 & 0 & 0 \end{pmatrix} \begin{pmatrix} d_{\mathrm{A},R_5^+,12} \\ d_{\mathrm{A},X_5^+,1} \\ d_{\mathrm{X},M_2^+,3} \\ d_{\mathrm{X},M_3^+,3} \\ d_{\mathrm{X},R_4^+,12} \\ d_{\mathrm{X},R_5^+,12} \\ d_{\mathrm{X},X_5^+,1} \end{pmatrix} + \begin{pmatrix} \frac{1}{2} \\ 0 \\ 0 \\ 0 \\ \frac{3}{4} \\ 0 \\ \frac{1}{4} \end{pmatrix} = \begin{pmatrix} x_{\mathrm{A}} \\ z_{\mathrm{A}} \\ x_{\mathrm{X1}} \\ z_{\mathrm{X1}} \\ x_{\mathrm{X2}} \\ y_{\mathrm{X2}} \\ z_{\mathrm{X2}} \end{pmatrix}$$

$$\frac{V_{\mathrm{A}}}{V_{\mathrm{B}}} = \frac{6}{1 - 4d^2_{\mathrm{X},M_2^+,3} + 4d^2_{\mathrm{X},M_3^+,3} + 8d^2_{\mathrm{X},R_4^+,12} - 8d^2_{\mathrm{X},R_5^+,12} + 16\left(d_{\mathrm{X},M_2^+,3} + d_{\mathrm{X},M_3^+,3}\right)\left(d_{\mathrm{X},R_4^+,12} + d_{\mathrm{X},R_5^+,12}\right)d_{\mathrm{X},X_5^+,1}} - 1$$

$$\approx \frac{6}{1 + 4\left(d^2_{\mathrm{X},M_3^+,3} + 2d^2_{\mathrm{X},R_4^+,12}\right)} - 1$$

---

i $a^+a^+c^-$ No. 137 $P4_2/nmc$

$a = b \approx 2a_p$, $c \approx 2a_p$

A1: (2*a*) $\frac{3}{4}, \frac{1}{4}, \frac{3}{4}$

A2: (2*b*) $\frac{3}{4}, \frac{1}{4}, \frac{1}{4}$

A3: (4*d*) $\frac{1}{4}, \frac{1}{4}, z\ (\approx \frac{1}{4})$

B: (8*e*) 0, 0, 0

X1: (8*g*) $\frac{1}{4}$, $y\ (\approx 0)$, $z\ (\approx 0)$

X2: (8*g*) $\frac{1}{4}$, $y\ (\approx \frac{1}{2})$, $z\ (\approx \frac{1}{2})$

X3: (8*f*) $x\ (\approx \frac{1}{2})$, $-x$, $\frac{1}{4}$

$$\begin{pmatrix} -\frac{1}{2} & 0 & 0 & 0 & 0 & 0 \\ 0 & 0 & -\frac{1}{2} & 0 & \frac{1}{2} & 0 \\ 0 & \frac{1}{2} & 0 & \frac{1}{2} & 0 & \frac{1}{2} \\ 0 & 0 & \frac{1}{2} & 0 & \frac{1}{2} & 0 \\ 0 & -\frac{1}{2} & 0 & -\frac{1}{2} & 0 & \frac{1}{2} \\ 0 & \frac{1}{2} & 0 & -\frac{1}{2} & 0 & 0 \end{pmatrix} \begin{pmatrix} d_{\mathrm{A},X_5^+,1256} \\ d_{\mathrm{X},M_3^+,23} \\ d_{\mathrm{X},M_4^+,1} \\ d_{\mathrm{X},M_4^+,23} \\ d_{\mathrm{X},R_4^+,1} \\ d_{\mathrm{X},X_5^+,1256} \end{pmatrix} + \begin{pmatrix} \frac{1}{4} \\ 0 \\ 0 \\ \frac{1}{2} \\ \frac{1}{2} \\ \frac{1}{2} \end{pmatrix} = \begin{pmatrix} z_{\mathrm{A3}} \\ y_{\mathrm{X1}} \\ z_{\mathrm{X1}} \\ y_{\mathrm{X2}} \\ z_{\mathrm{X2}} \\ x_{\mathrm{X3}} \end{pmatrix}$$

$$\begin{aligned} \frac{V_{\mathrm{A}}}{V_{\mathrm{B}}} &= \frac{6}{1+8d^2_{\mathrm{X},M_3^+,23}-4d^2_{\mathrm{X},M_4^+,1}-8d^2_{\mathrm{X},M_4^+,23}+4d^2_{\mathrm{X},R_4^+,1}-16d_{\mathrm{X},M_4^+,1}\left(d^2_{\mathrm{X},M_3^+,23}-d^2_{\mathrm{X},M_4^+,23}\right)} - 1 \\ &\quad -16\left(d_{\mathrm{X},M_3^+,23}-d_{\mathrm{X},M_4^+,23}\right)d_{\mathrm{X},R_4^+,1}d_{\mathrm{X},X_5^+,1256} \\ &\approx \frac{6}{1+4\left(2d^2_{\mathrm{X},M_3^+,23}+d^2_{\mathrm{X},R_4^+,1}\right)} - 1 \end{aligned}$$

---

j $a^0b^+c^-$ No. 63 *Cmcm*

$a \approx 2a_p$, $b \approx 2a_p$, $c \approx 2a_p$

A1: (4*c*) 0, y (≈ 0), $\frac{1}{4}$

A2: (4*c*) 0, y ($\approx \frac{1}{2}$), $\frac{1}{4}$

B: (8*d*) $\frac{1}{4}$, $\frac{1}{4}$, 0

X1: (8*e*) x ($\approx \frac{1}{4}$), 0, 0

X2: (8*f*) 0, y ($\approx \frac{1}{4}$), z (≈ 0)

X3: (8*g*) x ($\approx \frac{1}{4}$), y ($\approx \frac{1}{4}$), $\frac{1}{4}$

$$\begin{pmatrix} \frac{1}{2} & \frac{1}{2} & 0 & 0 & 0 & 0 & 0 \\ -\frac{1}{2} & \frac{1}{2} & 0 & 0 & 0 & 0 & 0 \\ 0 & 0 & \frac{1}{2} & -\frac{1}{2} & 0 & 0 & 0 \\ 0 & 0 & -\frac{1}{2} & -\frac{1}{2} & 0 & 0 & 0 \\ 0 & 0 & 0 & 0 & \frac{1}{2} & -\frac{1}{2} & 0 \\ 0 & 0 & 0 & 0 & \frac{1}{2} & \frac{1}{2} & 0 \\ 0 & 0 & 0 & 0 & 0 & 0 & -\frac{1}{2} \end{pmatrix} \begin{pmatrix} d_{\mathrm{A},R_5^+,3} \\ d_{\mathrm{A},X_5^+,34} \\ d_{\mathrm{X},M_3^+,1} \\ d_{\mathrm{X},M_4^+,1} \\ d_{\mathrm{X},R_4^+,3} \\ d_{\mathrm{X},R_5^+,3} \\ d_{\mathrm{X},X_5^+,34} \end{pmatrix} + \begin{pmatrix} 0 \\ \frac{1}{2} \\ \frac{1}{4} \\ \frac{1}{4} \\ 0 \\ \frac{1}{4} \\ \frac{1}{4} \end{pmatrix} = \begin{pmatrix} y_{\mathrm{A1}} \\ y_{\mathrm{A2}} \\ x_{\mathrm{X1}} \\ y_{\mathrm{X2}} \\ z_{\mathrm{X2}} \\ x_{\mathrm{X3}} \\ y_{\mathrm{X3}} \end{pmatrix}$$

$$\frac{V_{\mathrm{A}}}{V_{\mathrm{B}}} = \frac{6}{1+4d^2_{\mathrm{X},M_3^+,1}-4d^2_{\mathrm{X},M_4^+,1}+4d^2_{\mathrm{X},R_4^+,3}-4d^2_{\mathrm{X},R_5^+,3}-8\left(d_{\mathrm{X},M_3^+,1}-d_{\mathrm{X},M_4^+,1}\right)\left(d_{\mathrm{X},R_4^+,3}-d_{\mathrm{X},R_5^+,3}\right)d_{\mathrm{X},X_5^+,34}} - 1$$

$$\approx \frac{6}{1+4\left(d^2_{\mathrm{X},M_3^+,1}+d^2_{\mathrm{X},R_4^+,3}\right)} - 1$$

---

k $a^+b^-c^-$ No. 11 $P2_1/m$

$a \approx \sqrt{2}a_p$, $b \approx 2a_p$, $c \approx \sqrt{2}a_p$, $\beta \approx 90°$

A1: (2*e*) x (≈ 0), $\frac{1}{4}$, z (≈ 0)

A2: (2*e*) x ($\approx \frac{1}{2}$), $\frac{1}{4}$, z ($\approx \frac{1}{2}$)

B1: (2*b*) $\frac{1}{2}$, 0, 0

B2: (2*c*) 0, 0, $\frac{1}{2}$

X1: (2*e*) x (≈ 0), $\frac{1}{4}$, z ($\approx \frac{1}{2}$)

X2: (2*e*) x ($\approx \frac{1}{2}$), $\frac{1}{4}$, z (≈ 0)

X3: (4*f*) x ($\approx\frac{1}{4}$), y (≈ 0), z ($\approx\frac{1}{4}$)

X4: (4*f*) x ($\approx\frac{1}{4}$), y (≈ 0), z ($\approx\frac{3}{4}$)

$$\begin{pmatrix}
\frac{1}{2} & \frac{1}{2} & 0 & -1 & 0 & 0 & 0 & 0 & 0 & 0 & 0 & 0 & 0 & 0 \\
\frac{1}{2} & -\frac{1}{2} & -1 & 0 & 0 & 0 & 0 & 0 & 0 & 0 & 0 & 0 & 0 & 0 \\
-\frac{1}{2} & -\frac{1}{2} & 0 & -1 & 0 & 0 & 0 & 0 & 0 & 0 & 0 & 0 & 0 & 0 \\
-\frac{1}{2} & \frac{1}{2} & -1 & 0 & 0 & 0 & 0 & 0 & 0 & 0 & 0 & 0 & 0 & 0 \\
0 & 0 & 0 & 0 & 0 & 0 & 0 & 0 & \frac{1}{2} & -\frac{1}{2} & -\frac{1}{2} & -\frac{1}{2} & 0 & 1 \\
0 & 0 & 0 & 0 & 0 & 0 & 0 & 0 & -\frac{1}{2} & -\frac{1}{2} & \frac{1}{2} & -\frac{1}{2} & 1 & 0 \\
0 & 0 & 0 & 0 & 0 & 0 & 0 & 0 & -\frac{1}{2} & \frac{1}{2} & \frac{1}{2} & \frac{1}{2} & 0 & 1 \\
0 & 0 & 0 & 0 & 0 & 0 & 0 & 0 & \frac{1}{2} & \frac{1}{2} & -\frac{1}{2} & \frac{1}{2} & 1 & 0 \\
0 & 0 & 0 & 0 & -\frac{1}{2} & \frac{1}{2} & \frac{1}{2} & -\frac{1}{2} & 0 & 0 & 0 & 0 & 0 & 0 \\
0 & 0 & 0 & 0 & 0 & 0 & 0 & 0 & -\frac{1}{2} & 0 & -\frac{1}{2} & 0 & 0 & 0 \\
0 & 0 & 0 & 0 & \frac{1}{2} & -\frac{1}{2} & \frac{1}{2} & -\frac{1}{2} & 0 & 0 & 0 & 0 & 0 & 0 \\
0 & 0 & 0 & 0 & -\frac{1}{2} & -\frac{1}{2} & -\frac{1}{2} & -\frac{1}{2} & 0 & 0 & 0 & 0 & 0 & 0 \\
0 & 0 & 0 & 0 & 0 & 0 & 0 & 0 & 0 & \frac{1}{2} & 0 & -\frac{1}{2} & 0 & 0 \\
0 & 0 & 0 & 0 & -\frac{1}{2} & -\frac{1}{2} & \frac{1}{2} & \frac{1}{2} & 0 & 0 & 0 & 0 & 0 & 0
\end{pmatrix}
\begin{pmatrix}
d_{\mathrm{A},R_5^+,1} \\ d_{\mathrm{A},R_5^+,2} \\ d_{\mathrm{A},X_5^+,1} \\ d_{\mathrm{A},X_5^+,2} \\ d_{\mathrm{X},M_1^+,3} \\ d_{\mathrm{X},M_2^+,3} \\ d_{\mathrm{X},M_3^+,3} \\ d_{\mathrm{X},M_4^+,3} \\ d_{\mathrm{X},R_4^+,1} \\ d_{\mathrm{X},R_4^+,2} \\ d_{\mathrm{X},R_5^+,1} \\ d_{\mathrm{X},R_5^+,2} \\ d_{\mathrm{X},X_5^+,1} \\ d_{\mathrm{X},X_5^+,2}
\end{pmatrix}
+
\begin{pmatrix}
0 \\ 0 \\ \frac{1}{2} \\ \frac{1}{2} \\ 0 \\ \frac{1}{2} \\ \frac{1}{2} \\ 0 \\ \frac{1}{4} \\ 0 \\ \frac{1}{4} \\ \frac{1}{4} \\ 0 \\ \frac{3}{4}
\end{pmatrix}
=
\begin{pmatrix}
x_{\mathrm{A1}} \\ z_{\mathrm{A1}} \\ x_{\mathrm{A2}} \\ z_{\mathrm{A2}} \\ x_{\mathrm{X1}} \\ z_{\mathrm{X1}} \\ x_{\mathrm{X2}} \\ z_{\mathrm{X2}} \\ x_{\mathrm{X3}} \\ y_{\mathrm{X3}} \\ z_{\mathrm{X3}} \\ x_{\mathrm{X4}} \\ y_{\mathrm{X4}} \\ z_{\mathrm{X4}}
\end{pmatrix}$$

$$\frac{V_\mathrm{A}}{V_\mathrm{B}} = \frac{6}{1+4d^2_{\mathrm{X},M_1^+,3}-4d^2_{\mathrm{X},M_2^+,3}+4d^2_{\mathrm{X},M_3^+,3}-4d^2_{\mathrm{X},M_4^+,3}+4d^2_{\mathrm{X},R_4^+,1}+4d^2_{\mathrm{X},R_4^+,2}-4d^2_{\mathrm{X},R_5^+,1}-4d^2_{\mathrm{X},R_5^+,2}} - 1$$
$$+8\begin{pmatrix}\left(d_{\mathrm{X},M_1^+,3}+d_{\mathrm{X},M_2^+,3}+d_{\mathrm{X},M_3^+,3}+d_{\mathrm{X},M_4^+,3}\right)\left(d_{\mathrm{X},R_4^+,1}+d_{\mathrm{X},R_5^+,1}\right)\\+\left(d_{\mathrm{X},M_1^+,3}-d_{\mathrm{X},M_2^+,3}-d_{\mathrm{X},M_3^+,3}+d_{\mathrm{X},M_4^+,3}\right)\left(d_{\mathrm{X},R_4^+,2}-d_{\mathrm{X},R_5^+,2}\right)\end{pmatrix} d_{\mathrm{X},X_5^+,1}$$
$$-8\begin{pmatrix}\left(d_{\mathrm{X},M_1^+,3}+d_{\mathrm{X},M_2^+,3}-d_{\mathrm{X},M_3^+,3}-d_{\mathrm{X},M_4^+,3}\right)\left(d_{\mathrm{X},R_4^+,1}+d_{\mathrm{X},R_5^+,1}\right)\\-\left(d_{\mathrm{X},M_1^+,3}-d_{\mathrm{X},M_2^+,3}+d_{\mathrm{X},M_3^+,3}-d_{\mathrm{X},M_4^+,3}\right)\left(d_{\mathrm{X},R_4^+,2}-d_{\mathrm{X},R_5^+,2}\right)\end{pmatrix} d_{\mathrm{X},X_5^+,2}$$
$$\approx \frac{6}{1+4\left(d^2_{\mathrm{X},M_3^+,3}+d^2_{\mathrm{X},R_4^+,1}+d^2_{\mathrm{X},R_4^+,2}\right)} - 1$$

---

1 $a^+a^+a^+$ No. 204 $Im\overline{3}$

$a = b = c \approx 2a_p$

A1: (2*a*) 0, 0, 0

A2: (6*b*) 0, $\frac{1}{2}$, $\frac{1}{2}$

B: (8*c*) $\frac{1}{4}$, $\frac{1}{4}$, $\frac{1}{4}$

X: (24*g*) 0, *y* ($\approx\frac{1}{4}$), *z* ($\approx\frac{1}{4}$)

$$\begin{pmatrix}-\frac{1}{2} & -\frac{1}{2}\\ \frac{1}{2} & -\frac{1}{2}\end{pmatrix}\begin{pmatrix}d_{\mathrm{X},M_3^+,123}\\ d_{\mathrm{X},M_4^+,123}\end{pmatrix}+\begin{pmatrix}\frac{1}{4}\\ \frac{1}{4}\end{pmatrix}=\begin{pmatrix}y_\mathrm{X}\\ z_\mathrm{X}\end{pmatrix}$$

$$\frac{V_\mathrm{A}}{V_\mathrm{B}} = \frac{6}{1+12d^2_{\mathrm{X},M_3^+,123}-12d^2_{\mathrm{X},M_4^+,123}+16\left(3d^2_{\mathrm{X},M_3^+,123}+d^2_{\mathrm{X},M_4^+,123}\right)d_{\mathrm{X},M_4^+,123}} - 1$$
$$\approx \frac{6}{1+4\cdot 3d^2_{\mathrm{X},M_3^+,123}} - 1$$

---

m $a^0b^+b^+$ No. 139 *I*4/*mmm*

$a = b \approx 2a_p$, $c \approx 2a_p$

A1: (2*a*) 0, 0, 0

A2: (2*b*) 0, 0, $\frac{1}{2}$

A3: (4*c*) $\frac{1}{2}$, 0, 0

B: (8*f*) $\frac{1}{4}$, $\frac{1}{4}$, $\frac{1}{4}$

X1: (8*h*) x ($\approx \frac{1}{4}$), x, 0

X2: (16*n*) 0, y ($\approx \frac{1}{4}$), z ($\approx \frac{1}{4}$)

$$\begin{pmatrix} \frac{1}{2} & 0 & -\frac{1}{2} \\ 0 & -\frac{1}{2} & 0 \\ -\frac{1}{2} & 0 & -\frac{1}{2} \end{pmatrix} \begin{pmatrix} d_{\mathrm{X},M_3^+,23} \\ d_{\mathrm{X},M_4^+,1} \\ d_{\mathrm{X},M_4^+,23} \end{pmatrix} + \begin{pmatrix} \frac{1}{4} \\ \frac{1}{4} \\ \frac{1}{4} \end{pmatrix} = \begin{pmatrix} x_{\mathrm{X1}} \\ y_{\mathrm{X2}} \\ z_{\mathrm{X2}} \end{pmatrix}$$

$$\frac{V_\mathrm{A}}{V_\mathrm{B}} = \frac{6}{1+8d^2_{\mathrm{X},M_3^+,23} - 4d^2_{\mathrm{X},M_4^+,1} - 8d^2_{\mathrm{X},M_4^+,23} - 16d_{\mathrm{X},M_4^+,1}\left(d^2_{\mathrm{X},M_3^+,23} - d^2_{\mathrm{X},M_4^+,23}\right)} - 1$$

$$\approx \frac{6}{1+4\cdot 2d^2_{\mathrm{X},M_3^+,23}} - 1$$

---

n $a^+b^+c^+$ No. 71 *Immm*

$a \approx 2a_p$, $b \approx 2a_p$, $c \approx 2a_p$

A1: (2*a*) 0, 0, 0

A2: (2*b*) 0, $\frac{1}{2}$, $\frac{1}{2}$

A3: (2*c*) $\frac{1}{2}$, $\frac{1}{2}$, 0

A4: (2*d*) $\frac{1}{2}$, 0, $\frac{1}{2}$

B: (8*k*) $\frac{1}{4}$, $\frac{1}{4}$, $\frac{1}{4}$

X1: (8*l*) 0, *y* ($\approx\frac{1}{4}$), *z* ($\approx\frac{1}{4}$)

X2: (8*m*) *x* ($\approx\frac{1}{4}$), 0, *z* ($\approx\frac{1}{4}$)

X3: (8*n*) *x* ($\approx\frac{1}{4}$), *y* ($\approx\frac{1}{4}$), 0

$$\begin{pmatrix} -\frac{1}{2} & 0 & 0 & -\frac{1}{2} & 0 & 0 \\ 0 & 0 & \frac{1}{2} & 0 & 0 & -\frac{1}{2} \\ \frac{1}{2} & 0 & 0 & -\frac{1}{2} & 0 & 0 \\ 0 & -\frac{1}{2} & 0 & 0 & -\frac{1}{2} & 0 \\ 0 & 0 & -\frac{1}{2} & 0 & 0 & -\frac{1}{2} \\ 0 & \frac{1}{2} & 0 & 0 & -\frac{1}{2} & 0 \end{pmatrix} \begin{pmatrix} d_{\mathrm{X},M_3^+,1} \\ d_{\mathrm{X},M_3^+,2} \\ d_{\mathrm{X},M_3^+,3} \\ d_{\mathrm{X},M_4^+,1} \\ d_{\mathrm{X},M_4^+,2} \\ d_{\mathrm{X},M_4^+,3} \end{pmatrix} + \begin{pmatrix} \frac{1}{4} \\ \frac{1}{4} \\ \frac{1}{4} \\ \frac{1}{4} \\ \frac{1}{4} \\ \frac{1}{4} \end{pmatrix} = \begin{pmatrix} y_{\mathrm{X1}} \\ z_{\mathrm{X1}} \\ x_{\mathrm{X2}} \\ z_{\mathrm{X2}} \\ x_{\mathrm{X3}} \\ y_{\mathrm{X3}} \end{pmatrix}$$

$$\begin{aligned} \frac{V_\mathrm{A}}{V_\mathrm{B}} &= \frac{6}{1+4d^2_{\mathrm{X},M_3^+,1}+4d^2_{\mathrm{X},M_3^+,2}+4d^2_{\mathrm{X},M_3^+,3}-4d^2_{\mathrm{X},M_4^+,1}-4d^2_{\mathrm{X},M_4^+,2}-4d^2_{\mathrm{X},M_4^+,3}} -1 \\ &\quad +16d_{\mathrm{X},M_3^+,3}\left(d_{\mathrm{X},M_3^+,2}d_{\mathrm{X},M_4^+,1}+d_{\mathrm{X},M_3^+,1}d_{\mathrm{X},M_4^+,2}\right)+16\left(d_{\mathrm{X},M_3^+,1}d_{\mathrm{X},M_3^+,2}+d_{\mathrm{X},M_4^+,1}d_{\mathrm{X},M_4^+,2}\right)d_{\mathrm{X},M_4^+,3} \\ &\approx \frac{6}{1+4\left(d^2_{\mathrm{X},M_3^+,1}+d^2_{\mathrm{X},M_3^+,2}+d^2_{\mathrm{X},M_3^+,3}\right)} -1 \end{aligned}$$

---

o $a^-b^-c^-$ No. 2 $P\bar{1}$

$a \approx \sqrt{2}a_p$, $b \approx \sqrt{2}a_p$, $c \approx \sqrt{2}a_p$, $\alpha \approx 60°$, $\beta \approx 60°$, $\gamma \approx 60°$

A: (2*i*) *x* ($\approx\frac{1}{4}$), *y* ($\approx\frac{1}{4}$), *z* ($\approx\frac{1}{4}$)

B1: $(1a)$ 0, 0, 0

B2: $(1h)\frac{1}{2}, \frac{1}{2}, \frac{1}{2}$

X1: $(2i)$ x ($\approx\frac{1}{4}$), y ($\approx\frac{3}{4}$), z ($\approx\frac{1}{4}$)

X2: $(2i)$ x ($\approx\frac{1}{4}$), y ($\approx\frac{1}{4}$), z ($\approx\frac{3}{4}$)

X3: $(2i)$ x ($\approx\frac{3}{4}$), y ($\approx\frac{1}{4}$), z ($\approx\frac{1}{4}$)

$$\begin{pmatrix} -\frac{1}{2} & \frac{1}{2} & \frac{1}{2} & 0 & 0 & 0 & 0 & 0 & 0 & 0 & 0 & 0 \\ \frac{1}{2} & -\frac{1}{2} & \frac{1}{2} & 0 & 0 & 0 & 0 & 0 & 0 & 0 & 0 & 0 \\ \frac{1}{2} & \frac{1}{2} & -\frac{1}{2} & 0 & 0 & 0 & 0 & 0 & 0 & 0 & 0 & 0 \\ 0 & 0 & 0 & \frac{1}{2} & \frac{1}{4} & \frac{1}{2} & \frac{1}{2} & 0 & \frac{1}{2} & \frac{1}{2} & 0 & -\frac{1}{2} \\ 0 & 0 & 0 & -\frac{1}{2} & -\frac{1}{4} & -\frac{1}{2} & \frac{1}{2} & 0 & -\frac{1}{2} & \frac{1}{2} & 0 & \frac{1}{2} \\ 0 & 0 & 0 & \frac{1}{2} & \frac{1}{4} & \frac{1}{2} & -\frac{1}{2} & 0 & -\frac{1}{2} & -\frac{1}{2} & 0 & \frac{1}{2} \\ 0 & 0 & 0 & \frac{1}{2} & \frac{1}{4} & -\frac{1}{2} & -\frac{1}{2} & -\frac{1}{2} & 0 & \frac{1}{2} & -\frac{1}{2} & 0 \\ 0 & 0 & 0 & \frac{1}{2} & \frac{1}{4} & -\frac{1}{2} & \frac{1}{2} & \frac{1}{2} & 0 & -\frac{1}{2} & \frac{1}{2} & 0 \\ 0 & 0 & 0 & -\frac{1}{2} & -\frac{1}{4} & \frac{1}{2} & -\frac{1}{2} & \frac{1}{2} & 0 & \frac{1}{2} & \frac{1}{2} & 0 \\ 0 & 0 & 0 & -\frac{1}{2} & \frac{1}{2} & 0 & 0 & -\frac{1}{2} & \frac{1}{2} & 0 & \frac{1}{2} & \frac{1}{2} \\ 0 & 0 & 0 & \frac{1}{2} & -\frac{1}{2} & 0 & 0 & -\frac{1}{2} & -\frac{1}{2} & 0 & \frac{1}{2} & -\frac{1}{2} \\ 0 & 0 & 0 & \frac{1}{2} & -\frac{1}{2} & 0 & 0 & \frac{1}{2} & \frac{1}{2} & 0 & -\frac{1}{2} & \frac{1}{2} \end{pmatrix} \begin{pmatrix} d_{\mathrm{A},R_5^+,1} \\ d_{\mathrm{A},R_5^+,2} \\ d_{\mathrm{A},R_5^+,3} \\ d_{\mathrm{X},R_1^+,1} \\ d_{\mathrm{X},R_3^+,1} \\ d_{\mathrm{X},R_3^+,2} \\ d_{\mathrm{X},R_4^+,1} \\ d_{\mathrm{X},R_4^+,2} \\ d_{\mathrm{X},R_4^+,3} \\ d_{\mathrm{X},R_5^+,1} \\ d_{\mathrm{X},R_5^+,2} \\ d_{\mathrm{X},R_5^+,3} \end{pmatrix} + \begin{pmatrix} \frac{1}{4} \\ \frac{1}{4} \\ \frac{1}{4} \\ \frac{1}{4} \\ \frac{3}{4} \\ \frac{1}{4} \\ \frac{1}{4} \\ \frac{1}{4} \\ \frac{3}{4} \\ \frac{3}{4} \\ \frac{1}{4} \\ \frac{1}{4} \end{pmatrix} = \begin{pmatrix} x_{\mathrm{A}} \\ y_{\mathrm{A}} \\ z_{\mathrm{A}} \\ x_{\mathrm{X1}} \\ y_{\mathrm{X1}} \\ z_{\mathrm{X1}} \\ x_{\mathrm{X2}} \\ y_{\mathrm{X2}} \\ z_{\mathrm{X2}} \\ x_{\mathrm{X3}} \\ y_{\mathrm{X3}} \\ z_{\mathrm{X3}} \end{pmatrix}$$

$$\frac{V_{\mathrm{A}}}{V_{\mathrm{B}}} = \frac{6}{1+12d^2_{\mathrm{X},R_1^+,1} - 3d^2_{\mathrm{X},R_3^+,1} - 4d^2_{\mathrm{X},R_3^+,2} + 4d^2_{\mathrm{X},R_4^+,1} + 4d^2_{\mathrm{X},R_4^+,2} + 4d^2_{\mathrm{X},R_4^+,3} - 4d^2_{\mathrm{X},R_5^+,1} - 4d^2_{\mathrm{X},R_5^+,2} - 4d^2_{\mathrm{X},R_5^+,3}} - 1$$

$$\approx \frac{6}{1+4\left(d^2_{\mathrm{X},R_4^+,1} + d^2_{\mathrm{X},R_4^+,2} + d^2_{\mathrm{X},R_4^+,3}\right)} - 1$$